

The Pennsylvania State University

The Graduate School

College of Engineering

**COMPUTATIONAL MODELING OF AN 8-GHz MICROWAVE  
ELECTROTHERMAL THRUSTER**

A Thesis in

Aerospace Engineering

by

Christopher A. DeForce Jr.

©2011 Christopher A. DeForce Jr.

Submitted in Partial Fulfillment  
of the Requirements  
for the Degree of

Master of Science

May 2011

The thesis of Christopher A. DeForce Jr. was reviewed and approved\* by the following:

Michael M. Micci  
Professor of Aerospace Engineering and Director of Graduate Studies  
Thesis Advisor

Sven G. Bilén  
Associate Professor of Engineering Design, Electrical Engineering, and  
Aerospace Engineering

George A. Lesieutre  
Professor of Aerospace Engineering and Head of the Department of Aerospace  
Engineering

\*Signatures are on file in the Graduate School.

## ABSTRACT

The design of an 8-GHz Microwave Electrothermal Thruster was studied and optimized via numerical modeling. The electromagnetics of the thruster was modeled in an effort to develop and optimize a thruster design that would produce a robust electric field and resonate at the  $TM_{011}^z$  mode shape. The fluid dynamics of the MET propellant injection system were modeled in two and three dimensions.

The electromagnetics study investigated multiple designs and configurations in an effort to obtain a robust  $TM_{011}^z$  mode shape with an intense electric field concentration at the nozzle end of the thruster cavity. Models using both coaxial and waveguide ports for microwave energy inputs were investigated and optimized. It was found that though the coaxial input provided a stable  $TM_{011}^z$  mode, a much stronger electric field could be obtained by coupling a waveguide to a coaxial port. Also, using a waveguide short, the result could be fine-tuned. The design was optimized through testing different waveguide sizes and varying the antenna depth in the chamber. It was also found that the electric field intensity varied based upon the amount of dielectric in the cavity. Also, the resonant frequency increased when using a dielectric with a higher dielectric constant, but had little effect on the electric field intensity.

In the fluid dynamic analysis, three-dimensional models were developed for the propellant injection system using incompressible and weakly compressible fluid flow assumptions. A viscous compressible flow model was being developed using the governing equations: mass, momentum, and energy. Both two- and three-dimensional compressible flow models were developed; however, a three-dimensional compressible flow model was not completed. Future recommendations are made for future modeling efforts in completing the three-dimensional compressible flow modeling, as well as moving forward toward developing a numerical model that encapsulates the coalesced plasma characteristics that a physical prototype demonstrates.

# TABLE OF CONTENTS

<b>LIST OF FIGURES .....</b>	<b>vi</b>
<b>LIST OF TABLES .....</b>	<b>ix</b>
<b>NOMENCLATURE.....</b>	<b>x</b>
<b>ACKNOWLEDGMENTS .....</b>	<b>xii</b>
<b>CHAPTER 1Introduction .....</b>	<b>1</b>
<b>1.1 Space Propulsion.....</b>	<b>1</b>
1.1.1 Overview of Rocket Propulsion .....	1
1.1.2 Types of Propulsion Systems .....	3
<b>1.2 Microwave Electrothermal Thruster Overview.....</b>	<b>6</b>
1.2.1 Prior MET Research.....	8
1.2.1.1 Experimental Research .....	8
1.2.1.2 Numerical Research .....	10
<b>CHAPTER 2 Theory.....</b>	<b>12</b>
<b>2.1 Electromagnetic Theory .....</b>	<b>12</b>
2.1.1 Transverse Mode Shapes .....	13
2.1.2 The $TM_{011}^z$ Resonant Mode .....	13
<b>2.2 Fluid Mechanics .....</b>	<b>18</b>
2.2.1 The Continuity Equation.....	18
2.2.2 The Momentum Equation .....	19
2.2.3 The Energy Equation .....	20
<b>CHAPTER 3 Computational Analysis Setup.....</b>	<b>21</b>
<b>3.1 Electromagnetics Modeling.....</b>	<b>21</b>
3.1.1 Boundary Conditions .....	22
3.1.2 Mesh Setup.....	24
<b>3.2 Fluid Mechanics Modeling.....</b>	<b>25</b>
3.2.1 Boundary Conditions .....	25
3.2.1.1 3D Incompressible Flow .....	26
3.2.1.2 3D Weakly Compressible Flow .....	27
3.2.1.3 2D Compressible Flow.....	27
3.2.1.4 3D Compressible Flow.....	29
3.2.2 Mesh Setup.....	30

3.2.2.1 3D Incompressible Flow and 3D CFD Mesh.....	30
3.2.2.2 2D Compressible Flow Mesh.....	31
3.2.2.3 3D Compressible Flow Mesh.....	32
<b>CHAPTER 4 Results and Discussion .....</b>	<b>34</b>
<b>4.1 Electromagnetics Modeling.....</b>	<b>34</b>
4.1.1 Coaxial Modeling.....	34
4.1.1.1 Unloaded Cavity with Variable Antenna Depth .....	34
4.1.1.2 Dielectric Material .....	36
4.1.1.3 Optimized Coaxial Configuration .....	38
4.1.2.1 Waveguide Selection.....	39
4.1.2.2 Optimized Single Direct Waveguide Input Configuration.....	44
4.1.3 Double Direct Waveguide Input .....	46
4.1.4 Single Direct Waveguide Input with Short .....	48
4.1.4.1 WR90 Full-Height with Variable Short Length.....	48
4.1.4.2 WR90 Half-Height with Variable Short Length .....	55
4.1.4.3 WR90 Full-Height with Variable Quartz Short Length .....	61
4.1.4.4 Optimized Single Direct Waveguide Input with Short Configuration .....	65
4.1.5 Waveguide to Coaxial Coupling .....	67
4.1.5.1 WR90 vs. WR112 .....	68
4.1.5.2 Variable Antenna Depth.....	69
4.1.5.3 Electric Field Interaction with Plasma .....	70
4.1.5.4 Final MET Design.....	72
<b>4.2 Fluid Mechanics Modeling .....</b>	<b>74</b>
4.2.1 Viscous Incompressible Fluid Flow.....	74
4.2.2 Viscous Weakly Compressible Flow .....	77
4.2.2.1 Incompressible vs. Weakly Compressible Flow .....	79
4.2.3 2D Viscous Compressible Flow .....	79
4.2.4 3D Viscous Compressible Flow.....	82
<b>4.3 Summary of Results .....</b>	<b>84</b>
<b>CHAPTER 5 .....</b>	<b>86</b>
<b>Conclusions and Future Recommendations .....</b>	<b>86</b>
<b>REFERENCES.....</b>	<b>88</b>

# LIST OF FIGURES

Figure 1.1	Representation of conservation of momentum on rocket .....	2
Figure 1.2	Diagram of the MET .....	7
Figure 1.3	$TM_{011}^z$ resonant mode field lines within MET .....	7
Figure 2.1	Cylindrical reference frame of cylindrical resonant cavity with height $h$ and radius $a$ .....	14
Figure 3.1	Geometry of the MET .....	23
Figure 3.2	Meshed Geometry of MET .....	25
Figure 3.3	3D propellant injection system of MET .....	27
Figure 3.4	2D cylinder with converging nozzle .....	29
Figure 3.5	3D cylinder with converging nozzle .....	30
Figure 3.6	Meshed geometry of 3D propellant injection system of MET .....	32
Figure 3.7	Meshed geometry of the 2D cylinder with converging nozzle geometry .....	33
Figure 3.8	Meshed geometry of the 3D cylinder with converging nozzle geometry .....	34
Figure 4.1	Unloaded MET cavity with flat tip antenna .....	36
Figure 4.2	Unloaded MET cavity with rounded tip antenna .....	36
Figure 4.3	Geometry of chamber loaded with dielectric.....	38
Figure 4.4	Electric Field vs. Frequency for MET with varying dielectric materials .....	38
Figure 4.5	Contour plot of the E-Field for a coaxial configuration .....	39
Figure 4.6	Graph of E-Field vs. Frequency for the coaxial model .....	40
Figure 4.7	Contour plot of the E-Field for the full-height WR112 single waveguide configuration .....	41
Figure 4.8	Contour plot of the E-Field for the full-height WR90 single waveguide configuration .....	42
Figure 4.9	Contour plot of the E-Field for the half-height WR112 single waveguide configuration .....	43
Figure 4.10	Contour plot of the E-Field for the half-height WR90 single waveguide configuration .....	44
Figure 4.11	Plot of E-Field vs. Frequency for the single waveguide configurations.....	45
Figure 4.12	Contour plot of the E-Field for a single waveguide configuration.....	46
Figure 4.13	Graph of E-Field vs. Frequency for the single waveguide model .....	47
Figure 4.14	Contour plot of the E-Field for a double waveguide configuration .....	48
Figure 4.15	Graph of E-Field vs. Frequency for the double waveguide model.....	49

Figure 4.16	WR90 full-height with 40% length short configuration .....	50
Figure 4.17	WR90 full-height with 45% length short configuration .....	51
Figure 4.18	WR90 full-height with 50% length short configuration .....	52
Figure 4.19	WR90 full-height with 52.5% length short configuration .....	53
Figure 4.20	WR90 full-height with 55% length short configuration .....	54
Figure 4.21	WR90 full-height with 60% length short configuration .....	55
Figure 4.22	E-Field vs. Frequency for WR90 full-height waveguide configuration with short.....	56
Figure 4.23	WR90 half-height with 40% length short configuration .....	57
Figure 4.24	WR90 half-height with 45% length short configuration .....	58
Figure 4.25	WR90 half-height with 50% length short configuration .....	59
Figure 4.27	WR90 half-height with 55% length short configuration .....	60
Figure 4.28	WR90 half-height with 60% length short configuration .....	61
Figure 4.29	E-Field vs. Frequency for WR90 half-height waveguide configuration with short.....	61
Figure 4.30	WR90 full-height with 25% length quartz short configuration .....	62
Figure 4.31	WR90 full-height with 50% length quartz short configuration .....	63
Figure 4.32	WR90 full-height with 52.5% length quartz short configuration .....	64
Figure 4.33	WR90 full-height with 55% length quartz short configuration .....	65
Figure 4.34	E-Field vs. Frequency for WR90 full-height waveguide configuration with quartz short .....	66
Figure 4.35	Contour plot of the E-Field for a single waveguide with short configuration.....	67
Figure 4.36	Graph of E-Field vs. Frequency for the single waveguide with short model .....	68
Figure 4.37	Graph of E-Field vs. Frequency for the single waveguide with short model .....	69
Figure 4.38	Antenna depth study of E-Field vs. Frequency for WR90 full-height waveguide .....	70
Figure 4.39	Antenna depth study of E-Field vs. Frequency for WR112 full-height waveguide .....	71
Figure 4.40	Geometric setup of conducting sphere in MET cavity .....	72
Figure 4.41	E-field results in the presence of a conducting sphere for a WR112 configuration .....	72
Figure 4.42	Contour plot of the E-Field for a single waveguide with short with coaxial coupling.....	74
Figure 4.43	Graph of E-Field vs. Frequency for the single waveguide with coaxing coupling .....	75
Figure 4.44	3-D viscous incompressible flow COMSOL result of the propellant Injection.....	76

<b>Figure 4.45</b>	<b>Graph of pressure vs. distance for the viscous incompressible flow solution .....</b>	<b>77</b>
<b>Figure 4.46</b>	<b>Graph of velocity vs. distance for the viscous incompressible flow solution .....</b>	<b>77</b>
<b>Figure 4.47</b>	<b>3-D CFD velocity streamline result.....</b>	<b>78</b>
<b>Figure 4.48</b>	<b>Graph of pressure vs. distance for the COMSOL CFD solution .....</b>	<b>79</b>
<b>Figure 4.49</b>	<b>Graph of velocity vs. distance for the COMSOL CFD solution .....</b>	<b>79</b>
<b>Figure 4.50</b>	<b>Velocity comparison between incompressible and weakly compressible modules .....</b>	<b>80</b>
<b>Figure 4.51</b>	<b>2-D viscous compressible flow model .....</b>	<b>81</b>
<b>Figure 4.52</b>	<b>Graph of pressure vs. distance for the 2-D viscous compressible flow solution.....</b>	<b>82</b>
<b>Figure 4.53</b>	<b>Graph of velocity vs. distance for the 2-D viscous compressible flow solution .....</b>	<b>82</b>
<b>Figure 4.54</b>	<b>3-D viscous compressible flow model without RANS smoothing .....</b>	<b>83</b>
<b>Figure 4.55</b>	<b>3-D viscous compressible flow model with RANS smoothing.....</b>	<b>84</b>
<b>Figure 4.56</b>	<b>Comparison of pressure vs. distance for 3-D viscous compressible flow solutions before and after RANS smoothing.....</b>	<b>84</b>
<b>Figure 4.57</b>	<b>Comparison of velocity vs. distance for 3-D viscous compressible flow solutions before and after RANS smoothing.....</b>	<b>85</b>



## LIST OF TABLES

<b>Table 4.1</b>	<b>Comparison of antenna depths for unloaded MET cavity ..... 37</b>
------------------	--

## NOMENCLATURE

$A^*$	Nozzle throat area, m <sup>2</sup>
$A_e$	Nozzle exit area, m <sup>2</sup>
$A_z$	Magnetic vector potential, HA/m
$B_{mn}$	Vector potential constant, HA/m
$\beta$	Phase constant
$E$	Electric field, V/m
$e$	Internal energy, J/kg
$\vec{f}$	Force vector, N
$F_x$	Horizontal force, N
$f_{\text{res}}$	Resonant frequency, Hz
$g$	Gravitational acceleration at Earth's surface, m/s <sup>2</sup>
$H$	Magnetic field, A/m
$h$	Enthalpy, J/kg
$I_{\text{sp}}$	Specific impulse, s
$k$	Heat transfer coefficient, W/m <sup>2</sup> K
$\lambda$	Dynamic bulk viscosity, kg/m s
$\mu$	Viscosity, kg/m s
$M$	Mach number
$m$	Mass, kg
$\dot{m}$	Mass flow rate, kg/s
$\hat{n}$	Unit vector
$p$	Momentum, kg-m/s
$P_a$	Ambient pressure, Pa
$P_d$	Dissipated power, W
$P_e$	Exit pressure, Pa
$P_{\text{input}}$	Input power, W
$Q$	Quality factor

$\dot{q}$	Heat flux, J/kg s
$R_s$	Surface resistance, $\Omega$
$\tau$	Thrust, N
$u_e$	Exhaust velocity, m/s
$u_{eq}$	Equivalent velocity, m/s
$v$	Velocity, m/s
$W$	Total stored energy, J
$\eta_\tau$	Thrust efficiency
$\nabla$	Del operator

## **ACKNOWLEDGMENTS**

There are many people I would like to thank for their advice, assistance, encouragement, and confidence throughout my graduate school experience. I would like to thank Dr. Micci firstly for giving me the opportunity to do research with him; secondly for his advice, guidance, and confidence. I have learned a lot in my time doing research with him. I would like to thank Dr. Bilén for his advice and guidance. I would like to thank Dr. Silvio Chianese for his assistance and direction; and Northrop Grumman Aerospace Systems for the opportunity to work on this project and for funding my graduate education. I would like to thank Jeff Hopkins, Peter Hammond, and Enyu Gao for helping me to become acclimated with my research through giving advice and assistance. I would like to thank the faculty and staff in the Aerospace Department for their assistance throughout my time in both my undergraduate and graduate studies at Penn State.

More personally, I would like to thank my parents for their invaluable support, encouragement, and confidence throughout not only college, but throughout life as well. I would like to thank my grandmother, friends, and the rest of my family for their support, encouragement, and confidence in me throughout my entire life. I would lastly like to thank God for keeping me grounded throughout the duration of this thesis, research, and graduate school; and with every other facet of my life.

# **CHAPTER 1**

## **Introduction**

The Microwave Electrothermal Thruster (MET) propulsion system has been under development at The Pennsylvania State University for about 25 years. The MET is categorized as an electrothermal thruster that works on the principle of heating propellant via microwave energy. The goal of the MET research is to establish its viability by demonstrating the capabilities and advantages of such a system with the ultimate ambition of developing a system that will be used for space applications. The MET is ideal for satisfying the low thrust and high specific impulse needs in many of today's space missions.

In order to help simplify the design process of developing the thruster, numerical modeling is required. Numerical modeling accelerates the rate at which designs can be constructed and tested while decreasing the cost of design by eliminating the need to prototype every thruster configuration. Through numerical modeling, multiple designs can be evaluated, as well as fine-tuned and tweaked while eliminating the cost and time-related burdens of iterative physical prototyping. The focus of this thesis is on numerical modeling of an 8-GHz MET, specifically with respect to the electromagnetic fields and the fluid dynamic behavior in the thruster.

### **1.1 Space Propulsion**

Today's space propulsion systems operate on the premise of accelerating and expelling mass outward to induce an opposing force via the rate of change in momentum. This is known as the mass reaction principle and operates in adherence to Newton's third law. This opposing force is known as thrust. There are multiple methods of accomplishing this and, in order to design an effective propulsion system, it is fundamental that one has a general understanding of rocket propulsion.

#### **1.1.1 Overview of Rocket Propulsion**

As stated previously, rocket propulsion is based on Newton's third law, which states that, for every action, there is an equal and opposite reaction. The mass expelled from the rocket causes a rate of change in momentum, which thereby produces thrust. The equation for momentum can be expressed as

$$p = mv \quad (1.1)$$

An illustration of the forces acting upon a rocket within a control volume can give better insight on the mechanisms inducing thrust. These are diagrammed in Figure 1.1.

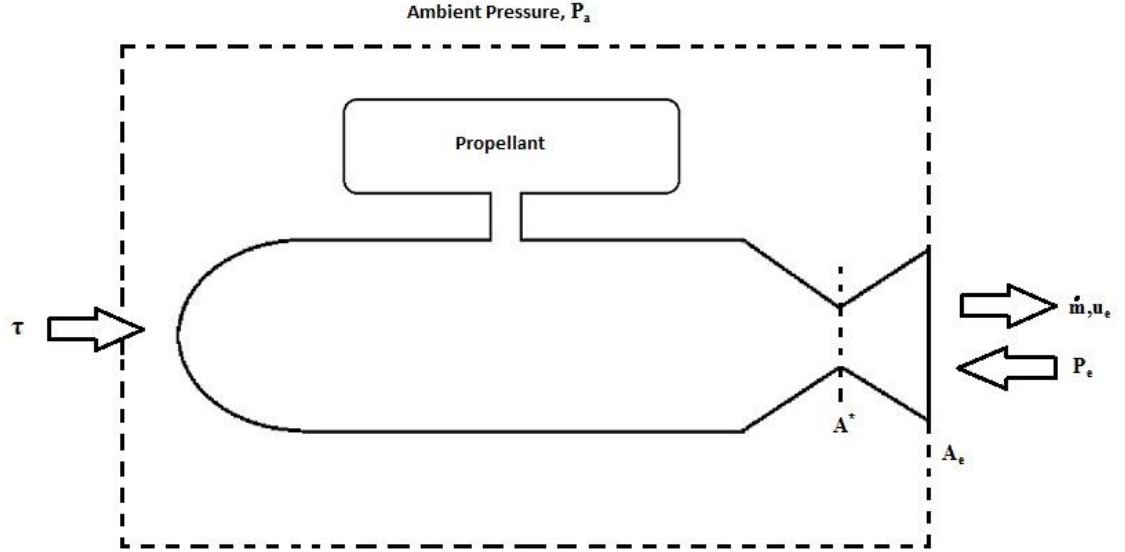


**Figure 1.1** Representation of conservation of momentum on rocket.

When gathering the forces acting upon the rocket in Figure 1.1 and balancing them relative to the sum of the horizontal forces, one can see that

$$\sum F_x = \tau - (P_e)A_e + (P_a)A_e \quad (1.2)$$

Taking into account that the change in momentum is equal to force, Equations (1.1) and (1.2) can be combined to form the equation for thrust,  $\tau$ , which is

$$\tau = \dot{m}u_e + (P_e + P_a)A_e \quad (1.3)$$

Generally, this is simplified by consolidating the velocity and pressures into a term known as the equivalent velocity,  $u_{eq}$ , given by

$$u_{eq} = u_e + \frac{(P_e - P_a)A_e}{\dot{m}} \quad (1.4)$$

Using this term, the thrust can now be represented as

$$\tau = \dot{m}u_{eq} \quad (1.5)$$

Although the thrust is a very important aspect of rocket performance, another factor greatly influences the overall performance. The specific impulse,  $I_{sp}$ , of a rocket has great influence on its overall efficiency and value for any specific space mission. Due to the limitations of mass that can be transported at a feasible cost, the efficiency of the rocket is critical. The specific impulse is a measure of a rocket's efficiency in its thrust per unit mass of propellant. This is usually represented in seconds of time.<sup>1</sup>The specific impulse,  $I_{sp}$ , is expressed as

$$I_{sp} = \frac{\tau}{\dot{m}g} = \frac{u_{eq}}{g} \quad (1.6)$$

### 1.1.2 Types of Propulsion Systems

There are a multitude of methods for generating thrust that are currently being used. The bulk of these methods tend to fall into one of two categories: chemical and electric propulsion. When looking at Equation (1.5), one can see that the two main factors that influence the thrust of a rocket are the exit velocity and the mass flow rate. Being mindful of the constraints of mass, the key to increasing rocket performance is to increase the amount of kinetic energy in the system per unit of mass, which in turn increases the momentum of the expelled mass. The propulsive methods mentioned above introduce energy in the system through different means and it is by understanding this concept that one can better understand the underlying constraints within each method.

A chemical rocket introduces energy into the system via stored chemical bonds in the propellant. This kinetic energy is released when these bonds are broken through exothermic chemical reactions. This energy is added the system and the propellant mass is subsequently ejected through a gas dynamic nozzle. Some rockets use monopropellants such as hydrazine ( $N_2H_4$ ), whereas others use bipropellants, in which the fuel is mixed with an oxidizer, such as in oxygen–hydrogen rockets.<sup>1</sup> Despite the method used, the same underlying constraints apply. Within a chemical system, the energy that can be introduced in the system is limited based upon

the stored energy within the propellant. It is important to note that losses occur within these reactions due to recombination and dissociation of the propellant. The thrust is constrained based upon the limitations of the attainable exit velocity and mass flow rate. The exit velocity is constrained by the rate of thermal expansion of the propellant within the chamber and an efficiently high mass flow rate is constrained by the size of the rocket itself. Although a chemical rocket can produce massive amounts of thrust, on the order of 5 MN, the specific impulses are limited to about 450 seconds.<sup>2</sup> The limitations of the specific impulse for chemical rockets make them practical for missions where a high thrust is needed to overcome obstacles such as the Earth's gravity during lift-off, but much less so for attitude control and basic satellite maneuvering.

Electric rockets are able to attain much higher specific impulses on the order of 1000s of seconds. However, they are currently constrained to low levels of thrust. Electric propulsion systems are typically used in satellites for attitude adjustment.<sup>1</sup>

With electric rockets, kinetic energy is directly added to the system via a power source. This power source ranges from solar cells and fuel cells to radioisotopes and nuclear reactors. Electric rockets can be divided into three subcategories: electrostatic, electromagnetic, and electrothermal.<sup>1</sup> These three subcategories add energy into the system using different means. In an electrostatic thruster, particles are charged by electron bombardment and accelerated by electrostatic forces. Some examples of electrostatic thrusters are: Hall thrusters and gridded electrostatic ion thrusters. Electromagnetic thrusters operate using electromagnetic and pressure forces to accelerate an ionized fluid. Some examples of an electromagnetic thruster are: magnetoplasmadynamic (MPD) thrusters and pulsed inductive thrusters (PID). Electrothermal thrusters operate on the principle of electrically heating a fluid and this can be achieved by means of an electrical arc discharge, electrical heating through a wall, or by creating plasma within the chamber using microwaves. Examples of these are arcjets, resistojets, and the MET, respectively.

Electric rockets are not constrained by chemical bonds as with chemical rockets, but by the power source used, thus making the attainable thrust theoretically infinite if such a power source were to exist. As opposed to chemical rockets, which have a set amount of energy per unit mass, the energy imparted on the particles in an electrical rocket can be much greater and can greatly reduce the amount of propellant consumed per unit impulse.<sup>1</sup> Due to the current limitations of



power systems, the thrust generated by electric rockets is not yet comparable to that of chemical rockets. As with chemical rockets, losses can also occur in electric rockets, but through power transmission and consumption. It is critical to gauge this and maximize the efficiency within the system and this efficiency,  $\eta_\tau$ , can be calculated using<sup>2</sup>

$$\eta_\tau = \frac{\dot{m} u_{eq}^2}{2P_{input}} \quad (1.7)$$

If one were to combine Equations (1.6) and (1.7), the required power can be calculated as<sup>2</sup>

$$P_{input} = \frac{\tau^2}{2\dot{m}\eta_\tau} = \frac{I_{sp}^2 g}{2\eta_\tau} \quad (1.8)$$

and is calculated based upon using a certain specific impulse, efficiency, and thrust. Using Equation (1.7) one can calculate the efficiency of a particular configuration of mass flow, velocity, and power.

It can be shown that the efficiency is directly related to the achieved mass flow and equivalent velocity relative to the power input, which is to be expected. Equation (1.8) can be used to calculate an input power corresponding to a desired thrust and specific impulse and specified efficiency. It is intuitive that the power input is greatly affected by the efficiency in that, as the efficiency deviates from unity, the power input required increases to compensate for losses in the system. The most important thing that can be deduced from Equation (1.8) is that the thrust and specific impulse are constrained by the maximum power that can be generated by the power source. Given a maximum power limit and assuming perfect efficiency, the true trade off within an electric thruster is the desired thrust relative to the specific impulse. Looking further in depth and observing Equations (1.5) and (1.6) for thrust and specific impulse, one can see that varying the mass flow of the propellant directly affects these two variables. Increasing the mass flow will result in an increase in thrust and a decrease in specific impulse and the converse when the mass flow is decreased.

## 1.2 Microwave Electrothermal Thruster Overview

The reasons for investing in the development of electric propulsion devices are driven by the need for having a thruster that can operate effectively over a long duration mission. Chemical propulsion is disadvantaged in this respect due to the fact that the specific impulse is much lower for these thrusters.

The Microwave Electrothermal Thruster (MET) is categorized under the electrothermal class of electric propulsion. The MET operates under a similar principle as an arcjet thruster. Both thrusters create a plasma to heat a propellant, though the manner in which this is accomplished differs. An arcjet thruster works by generating a high electric field between an anode and cathode to create plasma by breaking down propellant. The MET works under the principle of introducing microwave energy into a resonant cavity to create a coalesced plasma that is concentrated near the entrance of the thruster's nozzle. Figure 1.2 shows gives an idea of what the MET looks like. With the MET, the plasma is created by introducing microwaves at a specified frequency that is selected relative to the dimensions of the thruster. A frequency of 8.21 GHz was selected so that a  $TM_{011}^z$  mode shape could be formed for the desired cavity dimensions and the electric field would be at its maximum near the entrance to the nozzle. From here, free-floating plasma can be created in this region and propellant is injected into the MET in a vortex motion along the walls of the thruster where it is heated by the plasma and subsequently expelled out the nozzle. Figure 1.3 shows an example of  $TM_{011}^z$  resonant mode electric field lines within the MET.

The colors in Figure 1.3 show the intensity of the electric field. Dark blue indicates no electric field and red is an indication of a high electric field. It is important to note that the scale of intensity is of the order of  $10^6$ . Thus, these subtle changes in the hue of blue represent a large variation in the electric field. This model was generated using COMSOL Multiphysics, a finite element solver that is discussed later.

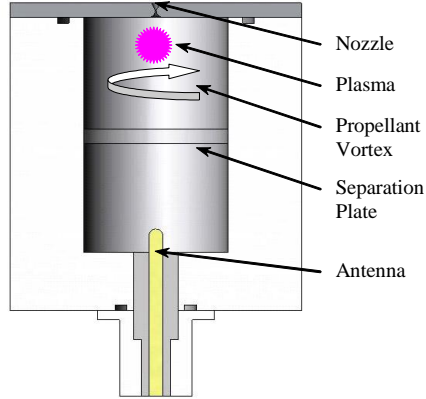


**Figure 1.2** Diagram of the MET

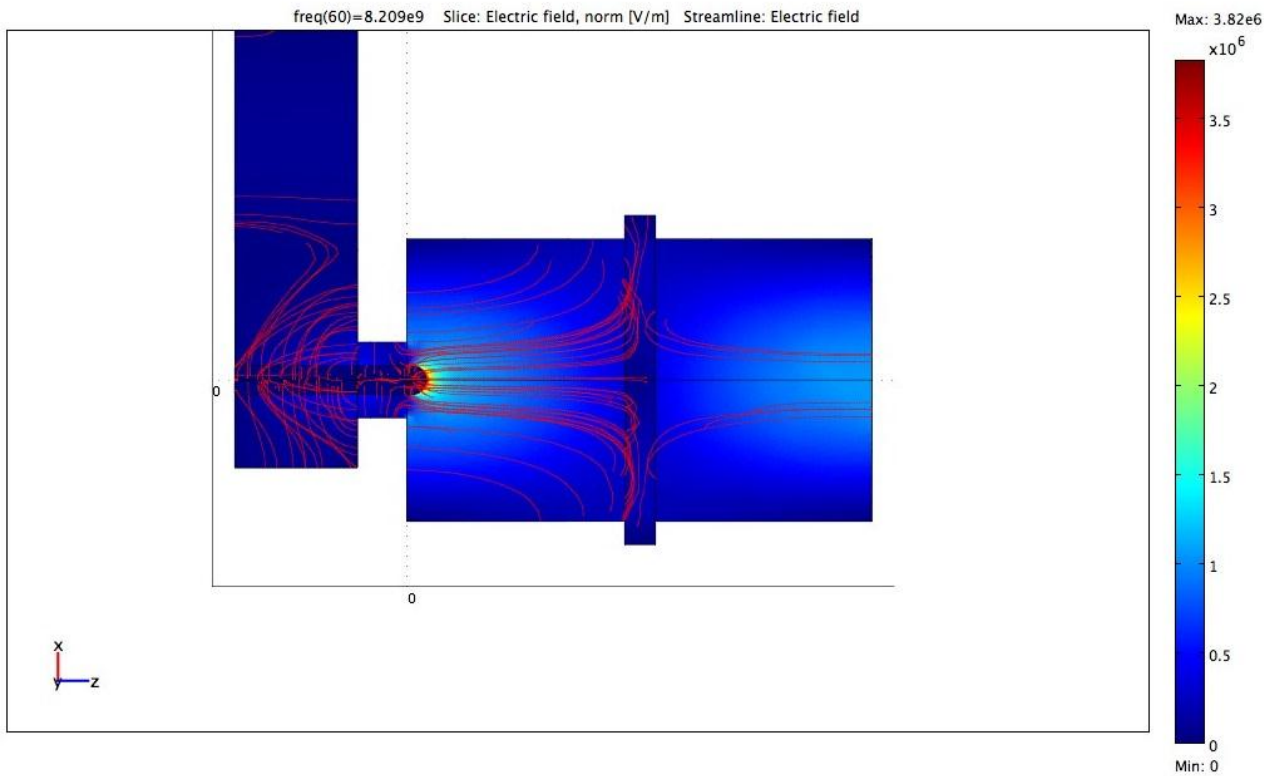


**Figure 1.3**  $TM_{011}^z$  resonant mode field lines within MET.

As stated previously, the fine-tuned microwave frequency was selected based upon the dimensions of the cavity, but diameter and length of the MET's cylindrical chamber were chosen with the intentions of concentrating the electric field near the end of the cavity. The microwaves are first introduced into a waveguide where the energy is transferred into the coaxial antenna and introduced into the chamber. An electric field is created within the chamber with a  $TM_{011}^z$  mode. The propellant is injected tangentially to the nozzle via injection ports at the wall located in the

section beyond the boron nitride separation plate. The propellant is introduced in this manner to swirl along the chamber wall with the intention of cooling it from the heat of the chamber, which can reach temperatures on the order of 2000 K.<sup>8</sup> The plasma is free-floating as mentioned previously and created at the end of the chamber where the electric field concentration is high. The advantage of having free-floating plasma is that potential issues such as surface erosion can be averted. An arcjet thruster will encounter progressive electrode erosion over time, making pulsed operation impractical.<sup>3</sup> Avoiding degradations like this can help increase the lifetime of the thruster and help preserve its functionality. The propellant is heated by the plasma and ejected through the converging–diverging nozzle of the thruster.

### **1.2.1 Prior MET Research**

The Microwave Electrothermal Thruster has been under development at The Pennsylvania State University for roughly 25 years. In the course of this development, multiple designs and configurations have been implemented via building and testing, while less emphasis has been placed on numerical modeling. Experimental efforts have ranged from a 2.45-GHz high power configuration to the current 8.21-GHz lower power configuration. Numerical modeling efforts have ranged from the numerical modeling of bluff body microwave plasmas to the current modeling of electromagnetics and fluid dynamics that will be discussed in this thesis.

#### **1.2.1.1 Experimental Research**

Mueller and Micci<sup>4,5</sup> investigated using a 2.45-GHz MET configuration that operated between 250 and 2000 watts. Research was performed with microwave-heated plasmas using a rectangular waveguide to sustain a  $TE_{10}$  electromagnetic field pattern, for which a coupling efficiency of 90% was achieved. The plasma was stabilized using bluff body stabilization in which a dielectric material such as boron nitride was inserted into the propellant flow. Stabilization was achieved upon the contingency of the mass flow rates and gas pressure being coupled with given power ranges. However, problems arose using this resonant mode due to the  $TE_{10}$  electromagnetic field pattern touching the waveguide walls ultimately resulting in thruster erosion and efficiency loss. Later, a circular  $TM_{10}$  mode applicator was investigated and resulted in alleviating the previous issue of wall touching when a coupling efficiency of up to 96% was achieved. Using a converging nozzle, thrust and specific impulse values of 0.4 N and 350 seconds were obtained using an input power of 1 kW, respectively.

Balaam and Micci<sup>6</sup> investigated the effects of stabilizing the plasma by swirling the propellant as compared to bluff body stabilization using a 2.45-GHz MET configuration that operated at 250–2000 watts. When investigating bluff body stabilization, it was found that the plasma was successfully kept away from all solid surfaces, which resulted in the plasma being able to absorb more power. In this approach, the plasma was sustained in pressures up to 500 kPa and coupling efficiencies between 95 and 100% were reached over a variety of operating conditions. With swirling flow stabilization, the plasma was highly sensitive to pressure and incident power. Problems regarding swirl flow stabilization were attributed simply to the geometry of the quartz vessel used rather than the technique itself.

Sullivan and Micci<sup>7</sup> worked on a coaxial configuration that operated at 2.45 GHz. This utilized the  $TM_{011}^z$  mode shape in an effort to generate the plasma near the entrance to the nozzle. The propellant was injected tangentially to the surface of the cavity walls to utilize swirl flow stabilization to increase the plasma discharge's axial stability. This helped to keep the plasma centered at the nozzle inlet. The propellants tested were hydrogen, helium, nitrogen, and ammonia. It was noted that although the microwave arcjet concept eliminated much of the core problems of the standard arcjet via generating free-floating plasma, erosion could still occur at the nozzle during high power operation.

Nordling *et al.*<sup>9</sup> was the first to work on a scaled-down version of the MET that operated at a higher frequency and used much less power than previously. This new configuration operated at 7.5 GHz with a power input of 100 watts. This configuration operated on the same premise as the thrusters following thereafter by utilizing the  $TM_{011}^z$  mode shape and injecting the propellant tangentially to the chamber walls in a vortical manner to help cool the chamber walls and stabilize the plasma via swirl stabilization. The justification for a smaller chamber was theorized based on the idea that a higher thrust-to-weight ratio could be obtained from the facts that the thruster was lighter and its smaller size would reduce convective thermal losses as a result of the decrease in the chamber-wall heat transfer rate while simultaneously stabilizing the plasma by reducing the plasma's tendency to expel more energy than it absorbs from the EM field.

Souliez *et al.*<sup>10</sup> continued working on the 7.5-GHz MET configuration by conducting emission spectroscopy of the plasma in an effort to measure the electron temperature for plasmas at relative power levels, measuring exhaust velocity via Doppler shift analysis, and by examining the assumption of local thermodynamic equilibrium (LTE). It was found that the electron

temperature for helium converged to about 4000 K with input powers of less than 100 watts. The LTE assumption was validated for pressures approaching 344 kPa. Using the Doppler shift experiment, specific impulse values were between 730 and 1330 seconds for powers between 15 and 30 MJ/kg for helium propellant. Nordling's thrust stand was also modified to allow vertical thrust measurements due to the fact that buoyancy had caused plasma instabilities, which resulted in thrust measurement losses. Following this modification, thrust measurements for helium were measured at 21.44 mN and 19.4 mN for nitrogen with specific impulses of 178 seconds and 89 seconds, respectively.<sup>11</sup>

Clemens<sup>12</sup> continued research on the 7.5-GHz and 2.45-GHz MET thrusters. Ammonia and simulated hydrazine were tested in the 2.45-GHz MET and specific impulses of 400 and 425 seconds were obtained, respectively. Tests with simulated hydrazine on the 7.5-GHz configuration resulted in a specific impulse of 220 seconds. Parametric studies of the effects of nozzle throat diameter, antenna probe depth, propellant injector diameter, and the inclusion of an impedance matching unit were performed for the 2.45-GHz MET. It was found that, by slightly decreasing the throat diameter of the nozzle, one could improve the overall performance. However, this was limited to the constraints of low Reynolds number losses.<sup>13</sup> That is, as the throat diameter is decreased, low Reynolds number losses become more significant and will eventually result in reducing overall performance.

Blum<sup>14</sup> investigated an 8-GHz MET configuration using nitrogen as the propellant. The input power ranged from 100 to 350 watts. The thruster was also optimized via parametrically testing a variety of different thruster components, including: antenna depth, propellant injector cross-sectional diameter, nozzle material and throat diameter, and propellant gas type. It was found that a one piece thruster design could not operate over a long duration without destroying the antenna, which was shown when the MET was tested with nitrogen. The MET was optimized using ammonia as the propellant, which resulted in a specific impulse that was 33% higher than that achieved by the 2.45-GHz configuration.

### **1.2.1.2 Numerical Research**

Venkateswaran and Merkle<sup>15</sup> investigated numerical bluff body stabilized plasmas and compared these results with experimental measurements. Using the code they developed, parameters such as the size, shape, location, overall thermal efficiency, coupling efficiency, and peak temperature of the plasma were able to be accurately predicted. This was predicted using

the Navier–Stokes and Maxwell equations. It should be noted that the cavity used by Balaam and Micci<sup>6</sup> was modeled in these simulations. It was found that the coupling efficiency reaches up to 99% when using low powers, but decreases as power is increased. The reason for this is that the geometry of the chamber limits the growth of the plasma. The plasma peak temperature was estimated to be about 12,000 K and this was confirmed by experimental results. Finally, it is noted that peak performance occurs when the plasma is located near the entrance to the nozzle.

Initial efforts to generate models of electromagnetic effects were conducted by Bilén *et al.*<sup>16</sup> using COMSOL Multiphysics, a finite element solver. The configuration studied was the 70-W 7.5-GHz MET. The  $TM_{011}^z$  mode was the electromagnetic field was chosen. In this study, three different cases were considered. However, all cases used a coaxial antenna to inject the microwave energy. The three configurations were: an empty cavity, a cavity with a dielectric covering the antenna, and a cavity with a dielectric separation plate. The disadvantage of using an empty cavity is that, in an empty cavity, a low pressure plasma forms in the cavity and can damage the antenna. The separation plate is intended to inhibit this by maintaining a high enough pressure near the antenna to prevent breakdown.

Valentino<sup>17</sup> continued modeling electromagnetic effects on a 7.5-GHz MET configuration using COMSOL and also performed some fluid dynamics modeling of propellant injection using FLUENT. With the electromagnetics modeling, studies were performed on the size and shape of the antenna, the conical half angle of the nozzle end, and different dielectric filler configurations. It was found in these studies that the size and the shape of the antenna have an effect on the resonant frequency and a minor effect on field strength. The resonant frequency was found to decrease when more dielectric was used and the electric field strength changed based on the amount and type of dielectric used. A 2-dimensional study of the fluid dynamics of the thruster indicated that the mass flow was 16.4 mg/s and resulted in a thrust of 7.279 mN which only deviated by 6% from that predicted by isentropic flow theory.

## CHAPTER 2

### Theory

The mechanisms of the MET are governed by multiple physical processes. These processes include: electromagnetics, fluid mechanics, thermodynamics, and plasma physics. It would be extremely complex to move straightway in creating a model that captured all of the various physics and characteristics of the MET due to their coupled nature. It is much more practical to treat the total product as a system and break these relative fields down into subsystems, thereby averting the overlying coupling difficulties and complexities and focusing more on the subatomic issues of the individual models themselves. This way, once the individual theoretical models are accurately represented, work can be done on merging these models into a more wholesome complete model. This is one of the many reasons that COMSOL Multiphysics was used for modeling the physics in the MET. COMSOL Multiphysics a software package that allows one to create multiple theoretical models and integrate them into a coupled system.

This thesis focuses on the electromagnetics and fluid mechanics of the thruster; the underlying theory represented in these models is discussed in this chapter.

#### 2.1 Electromagnetic Theory

As mentioned previously, the MET is an electric thruster that works on the premise of introducing microwave energy into a resonant cavity to generate an electric field with the  $TM_{011}^z$  mode shape. Using this mode shape, the highest concentration of energy is near the entrance of the nozzle and the opposite end of the cavity. When the propellant is introduced, the high electric field breaks down the propellant into a coalesced free-floating plasma that is then used to heat the flowing propellant that is expanded and subsequently ejected from the nozzle to generate thrust. In order to successfully obtain the  $TM_{011}^z$  mode shape to accomplish this, one must have an understanding of electromagnetic theory. More specifically, an understanding of the various types of mode shapes, the  $TM_{011}^z$  resonant mode, possible perturbations, and how to determine its quality factor.



### 2.1.1 Transverse Mode Shapes

Transverse modes can be grouped into four categories, which are: transverse electric (TE), transverse magnetic (TM), transverse electromagnetic (TEM), and hybrid. In the transverse electric mode, there is no electric field in the direction of propagation. Conversely, there is no magnetic field in the direction of propagation in the transverse magnetic mode. With transverse electromagnetic waves, neither electric nor magnetic fields are in the direction of propagation. Finally, in hybrid modes, there exists a nonzero electric and magnetic field in the direction of propagation. The primary focus, however, will be on the transverse magnetic mode, specifically the  $TM_{011}^z$  due to the advantages it has with respect to the MET.

### 2.1.2 The $TM_{011}^z$ Resonant Mode

The electromagnetic theoretical focus will be on the MET cavity, which can be treated as a circular waveguide. A resonator can be created by closing sections of a waveguide. In doing this, electric and magnetic energy can be stored in the cavity because the ends of the closed cavity are generally short-circuited at both ends, forming a closed box. Losses can occur via power dissipation into the walls as well as any dielectric, if present.

The resonance depends greatly upon the geometry of the cavity. Both the shape (whether rectangular or cylindrical) and dimensions can have great influence on the mode shape obtained and, by being selective with these criteria, one can obtain a preferred resonant mode shape. The theory behind finding the resonant mode for the MET is explored. This derivation makes the following assumptions: 1) the cavity is a perfect electric conductor and 2) the medium within the cavity is lossless, homogenous, and source-free.<sup>18</sup>

Since the closed-cylindrical waveguide is being assumed, the use of a cylindrical coordinate system will be used in this derivation. The cylindrical reference frame is defined in Figure 2.1.

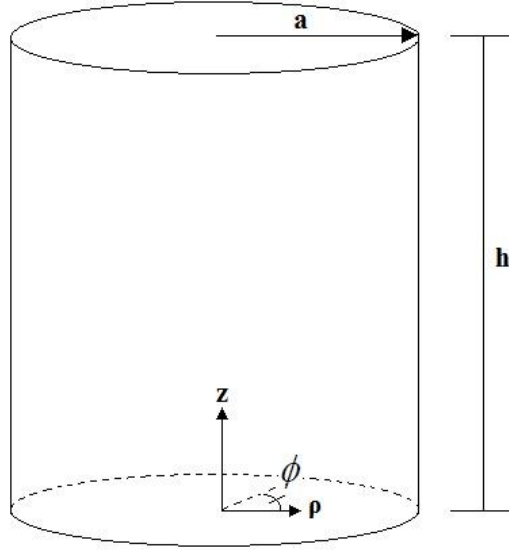


**Figure 2.1** Cylindrical reference frame of cylindrical resonant cavity with height  $h$  and radius  $a$ .

A transverse magnetic (TM) mode propagating in the  $z$  direction is desired for the MET and this is denoted by  $\text{TM}^z$ . The first step in solving for the electric field equations is to derive the value of the vector potential  $A_z$  by first reducing the vector form of the wave equation

$$\nabla^2 A + \beta^2 A = -\mu J \quad (2.1)$$

into its scalar form with  $J=0$  to arrive to the scalar wave equation<sup>19</sup>

$$\nabla^2 A_z(\rho, \phi, z) + \beta^2 A_z(\rho, \phi, z) = 0 \quad (2.2)$$

Equation (2.2) can then be applied to the case of a cylindrical coordinate system to derive the vector potential

$$A_z(\rho, \phi, z) = B_{mn} J_m(\beta_\rho \rho) [C_2 \cos(m\phi) + D_2 \sin(m\phi)] [C_3 \cos(\beta_z z) + D_3 \sin(\beta_z z)] \quad (2.3)$$

where

$$\beta_\rho = \frac{\chi_{mn}}{a} \quad (2.4)$$

In order to derive  $\beta_z$ , one must first obtain the cylindrical  $\text{TM}^z$  mode equations for the electric and magnetic fields. This can be accomplished using the second-order differential equation form of Maxwell's equation and the vector potential for time-harmonic fields, which result in the following<sup>19</sup>

$$E_\rho = -j \frac{1}{\omega_r \mu \epsilon} \frac{\partial^2 A_z}{\partial \rho \partial z} \quad (2.5)$$

$$E_\phi = -j \frac{1}{\omega_r \mu \varepsilon} \frac{1}{\rho} \frac{\partial^2 A_z}{\partial \phi \partial z} \quad (2.6)$$

$$E_z = -j \frac{1}{\omega_r \mu \varepsilon} \left( \frac{\partial^2}{\partial z^2} + \beta_r \right) A_z \quad (2.7)$$

$$H_\rho = \frac{1}{\mu} \frac{1}{\rho} \frac{\partial A_z}{\partial \phi} \quad (2.8)$$

$$H_\phi = -\frac{1}{\mu} \frac{\partial A_z}{\partial \rho} \quad (2.9)$$

$$H_z = 0 \quad (2.10)$$

Upon obtaining these equations, one must be mindful of the boundary conditions that must be imposed. It is important to note that the tangential components of the electric field do not exist on a conducting material and, using this, one can derive a set of boundary conditions. The boundary conditions are<sup>19</sup>

$$E_\rho(\rho, \phi, z = 0, h) = 0 \quad (2.11)$$

$$E_\phi(\rho, \phi, z = 0, h) = 0 \quad (2.12)$$

$$E_z(\rho, \phi, z) = 0 \quad (2.13)$$

Next, by inserting Equation (2.3) into Equation (2.6), one obtains

$$E_\phi(\rho, \phi, z) = -j \frac{1}{\omega_r \mu \varepsilon} \frac{1}{\rho} \frac{\partial^2 A_z}{\partial \phi \partial z} = -j B_{mnp} \frac{m \beta_z}{\omega \mu \varepsilon} \frac{1}{\rho} J_m(\beta_\rho \rho) [-C_2 \sin(m\phi) + D_2 \cos(m\phi)] \times [-C_3 \sin(\beta_z z) + D_3 \cos(\beta_z z)] \quad (2.14)$$

and by applying the boundary conditions from Equation (2.12) and setting Equation (2.14) equal to zero, the following is obtained

$$\beta_z = \frac{p\pi}{h} \quad (2.15)$$

A relationship exists between  $\beta_\rho$  and  $\beta_z$

$$\beta_\rho^2 + \beta_z^2 = \left( \frac{\chi_{mn}}{a} \right)^2 + \left( \frac{p\pi}{h} \right)^2 = \beta_r^2 = \omega_r^2 \mu \varepsilon \quad (2.16)$$

and by using this relationship, one can obtain the equation for the resonant frequency

$$(f_{\text{res}})_{mnp}^{\text{TM}^z} = \frac{1}{2\pi\sqrt{\mu\epsilon}} \sqrt{\left(\frac{\chi_{mn}}{a}\right)^2 + \left(\frac{p\pi}{h}\right)^2} \quad (2.17)$$

The previously derived expressions were of the general form. The  $\text{TM}_{011}^z$  mode is the specific  $\text{TM}^z$  mode desired and thus the electric field and magnetic field equations given in Equations (2.5)–(2.10) are now<sup>12</sup>

$$E_\rho = j \frac{B_{011}}{\omega\mu\epsilon} \frac{\chi_{01}}{a} \frac{\pi}{h} J_0' \left( \frac{\chi_{01}}{a} \rho \right) \sin \left( \frac{\pi}{h} z \right) \quad (2.18)$$

$$E_\phi = 0 \quad (2.19)$$

$$E_z = -j \frac{B_{011}}{\omega\mu\epsilon} \left( \frac{\chi_{01}}{a} \right)^2 J_0 \left( \frac{\chi_{01}}{a} \rho \right) \cos \left( \frac{\pi}{h} z \right) \quad (2.20)$$

$$H_\rho = 0 \quad (2.21)$$

$$H_\phi = -\frac{B_{011}}{\mu} \frac{\chi_{01}}{a} J_0' \left( \frac{\chi_{01}}{a} \rho \right) \cos \left( \frac{\pi}{h} z \right) \quad (2.22)$$

$$H_z = 0 \quad (2.23)$$

and the equation for the resonant frequency for a  $\text{TM}_{011}^z$  mode cavity is

$$(f_{\text{res}})_{011}^{\text{TM}^z} = \frac{1}{2\pi\sqrt{\mu\epsilon}} \sqrt{\left(\frac{\chi_{01}}{a}\right)^2 + \left(\frac{\pi}{h}\right)^2} \quad (2.24)$$

It is important to note that Equation (2.24) for the resonant frequency assumes the ideal conditions stated previously. When designing a cavity, one must take into account the perturbations to this ideal approach that can cause a discrepancy between the calculated resonant frequency and the true ideal frequency. Some perturbations include: 1) the medium within the cavity, 2) the dielectric used, 3) the temperature variation, 4) potential geometric irregularities, and 5) the plasma. All of these can have effect on the frequency and, for this reason it was critical to take all of these into account when choosing the geometry for the MET thruster.

Aside from the perturbations that can cause deviations from the ideal resonant frequency calculation, another factor must be taken into account when designing a resonant microwave

cavity. This is the energy dissipation into the walls of the cavity. This can be gauged by estimating the quality factor,  $Q$ . The quality factor is defined as the ratio of the energy stored in the cavity to the energy dissipated in the cavity per cycle, typically in the conducting walls. The quality factor can be calculated using

$$Q = \omega \frac{W}{P_d} \quad (2.25)$$

It should be noted that, as the quality factor increases, the oscillations are more slowly damped.  $W$  is the total energy stored in the cavity can be given by<sup>19</sup>

$$W = \frac{\epsilon}{2} \iiint_V |E|^2 dV \quad (2.26)$$

and after inserting the electric field equations for the  $\text{TM}_{011}^z$  mode, Equations (2.18) through (2.20) into Equation (2.26), and taking the integral, one can obtain the total energy stored in the cavity

$$W = \frac{\pi \epsilon h a^2}{4} \left( \frac{B_{011}}{\omega \mu \epsilon} \right)^2 \left( \frac{\chi_{01}}{a} \right)^2 J_1^2(\chi_{01}) \left[ \left( \frac{\pi}{h} \right)^2 + \left( \frac{\chi_{01}}{a} \right)^2 \right] \quad (2.27)$$

The power dissipated by the cavity,  $P_d$ , is calculated using

$$P_d = \frac{R_s}{2} \iint_A |H|^2 d\bar{S} \quad (2.28)$$

where  $R_s$  is the surface resistance

$$R_s = \sqrt{\frac{\omega \mu}{2\sigma}} \quad (2.29)$$

Taking magnetic field equations for the  $\text{TM}_{011}^z$  mode, Equations (2.21) through (2.23), and solving for the integral, the power dissipated by the cavity can be found using

$$P_d = \frac{\pi}{2} \sqrt{\frac{\omega \mu}{2\sigma}} \left( \frac{B_{011}}{\mu} \right)^2 \left( \frac{\chi_{01}}{a} \right)^2 J_1^2(\chi_{01}) [h^2 + 2a^2] \quad (2.30)$$

The quality factor for the  $\text{TM}_{011}^z$  mode can be calculated by inserting Equations (2.24), (2.27), and (2.30) into Equation (2.25), yielding

$$Q = \frac{ha^2}{ha + 2a^2} \left( \frac{\sigma}{2} \right)^{1/2} \left( \frac{\mu}{\varepsilon} \right)^{1/4} \left[ \left( \frac{\pi}{h} \right)^2 + \left( \frac{\chi_{01}}{a} \right)^2 \right]^{1/4} \quad (2.31)$$

It should be noted that, for the MET, the power is not only dissipated into the walls of the cavity, but also into the plasma and propellant, which would also cause some additional deviation from the analytical solution.

## 2.2 Fluid Mechanics

The MET injects propellant in a vortical motion along the walls of the thruster to cool the chamber from the heat of the plasma. In order to design a propellant injection system as in the MET, an understanding of fluid mechanics is necessary. In this thesis, the propellant injection system was modeled numerically using COMSOL Multiphysics. This was accomplished using the governing equations: continuity, momentum, and energy.

### 2.2.1 The Continuity Equation

The conservation of mass is based upon the premise that matter can neither be created nor destroyed.<sup>1</sup> The basic idea is that the rate of change of the mass in a given control volume is zero. The continuity equation can be defined as:

$$\frac{\partial \rho}{\partial t} + \nabla \cdot (\rho \vec{u}) = 0 \quad (2.32)$$

and represents unsteady-compressible flow. The assumption made in the numerical model was that the fluid flow was steady and, thus,

$$\frac{\partial \rho}{\partial t} = 0 \quad (2.33)$$

When creating the numerical model, the initial model assumed an incompressible flow to simplify the model. This boundary condition assumed the density,  $\rho$ , to be constant and changes Equation (2.32) to

$$\rho \cdot \nabla(\vec{u}) = 0 \quad (2.34)$$

which can be expanded to

$$\rho \left( \frac{\partial u}{\partial x} + \frac{\partial v}{\partial y} + \frac{\partial w}{\partial z} \right) = 0 \quad (2.35)$$

and Equation (2.32) can be rewritten as

$$\frac{\partial \rho}{\partial x} u + \frac{\partial \rho}{\partial y} v + \frac{\partial \rho}{\partial z} w + \rho \left( \frac{\partial u}{\partial x} + \frac{\partial v}{\partial y} + \frac{\partial w}{\partial z} \right) = 0 \quad (2.36)$$

This is the expanded continuity equation for 3-D compressible flow.

### 2.2.2 The Momentum Equation

The conservation of momentum operates based upon Newton's second law which states that the time rate of change of momentum in a body equals the force exerted upon it.<sup>1</sup> The conservation of momentum can be expressed as

$$\iiint_V \frac{\partial}{\partial t} (\rho \bar{u}) dV + \iint_S \rho \bar{u} (\bar{u} \cdot \bar{n}) dS = - \iint_S \rho \bar{n} dS + \iiint_V \rho \bar{f} dV \quad (2.37)$$

and this can be modified to a simpler form by applying the divergence theorem to yield the differential form

$$\frac{\partial \rho \bar{u}}{\partial t} + \nabla \cdot (\rho \bar{u} \bar{u}^T) = -\nabla p + \rho \bar{f} \quad (2.38)$$

which is an equation for an inviscid compressible flow. Equation (2.38) can be broken up into three separate equations for the respective velocity components:  $u$ ,  $v$ , and  $w$ . Doing this results in the following three equations

$$\rho \frac{Du}{Dt} = -\frac{\partial p}{\partial x} + \sum F_x \quad (2.39)$$

$$\rho \frac{Dv}{Dt} = -\frac{\partial p}{\partial y} + \sum F_y \quad (2.40)$$

$$\rho \frac{Dw}{Dt} = -\frac{\partial p}{\partial z} + \sum F_z \quad (2.41)$$

In order to account for the viscosity of the fluid, the term  $\phi$  can be added to the right-hand side of Equation (2.38) and is defined as<sup>21</sup>

$$\begin{aligned} \phi = \mu & \left[ 2 \left( \frac{\partial u}{\partial x} \right)^2 + 2 \left( \frac{\partial v}{\partial y} \right)^2 + 2 \left( \frac{\partial w}{\partial z} \right)^2 + \left( \frac{\partial v}{\partial x} + \frac{\partial u}{\partial y} \right)^2 + \left( \frac{\partial w}{\partial y} + \frac{\partial v}{\partial z} \right)^2 + \left( \frac{\partial u}{\partial z} + \frac{\partial w}{\partial x} \right)^2 \right] \\ & + \lambda \left( \frac{\partial u}{\partial x} + \frac{\partial v}{\partial y} + \frac{\partial w}{\partial z} \right)^2 \end{aligned} \quad (2.42)$$

Where, according to Stokes' hypothesis,

$$\lambda = -\frac{2}{3}\mu \quad (2.43)$$

Equation (2.42) can be broken up into its respective components and implemented into Equations (2.39)–(2.41) to yield the full three-dimensional viscous compressible flow equations.

### 2.2.3 The Energy Equation

The conservation of energy equation adheres to the first law of thermodynamics, which states that energy can be neither created nor destroyed. The energy equation can be expressed as<sup>20</sup>

$$\int_{CV} \dot{q} \rho V - \int_{CS} p \bar{u} \cdot d\bar{S} + \int_{CV} \rho(\bar{f} \cdot \bar{u}) dV = \int_{CV} \frac{d}{dt} \left[ \rho \left( e + \frac{u^2}{2} \right) \right] dV + \int_{CS} \rho \left( e + \frac{u^2}{2} \right) \bar{u} \cdot d\bar{S} \quad (2.44)$$

Through some manipulation, the energy equation can be rewritten as<sup>21</sup>

$$\rho \frac{D}{Dt} \left( e + \frac{p}{\rho} \right) = \frac{Dp}{Dt} + \nabla(k \nabla T) + \phi \quad (2.45)$$

where  $\phi$  is the viscous terms from Equation (2.42). This can be simplified knowing that

$$h = e + \frac{p}{\rho} \quad (2.46)$$

and thus Equation (2.46) becomes

$$\rho \frac{Dh}{Dt} = \frac{Dp}{Dt} + \nabla(k \nabla T) + \phi \quad (2.47)$$



## **CHAPTER 3**

### **Computational Analysis Setup**

Computational technology has made great leaps and bounds in the past 40 years, making the computer more viable for attacking complex problems. This has allowed engineers and scientists to rely also on solving problems numerically than only by physical experiments. Specifically with respect to innovation, this transition has effectively saved a great amount of money and time. The incorporation of computer modeling into research and development has allowed engineers to generate numerous theoretical prototypes to test a concept or design in lieu of reiterative physical prototyping, which can be much more costly and time consuming.

In this research, computer modeling of the MET was done numerically to simulate the electromagnetics and fluid mechanics of the thruster. Through modeling numerous designs to find a configuration that presented the best method of generating the most stable  $TM_{011}^z$  mode, the current thruster design was selected. This was accomplished using the commercially available software package COMSOL Multiphysics. Using this package, the various types of physics of a design or concept can be modeled and through these simulations, critical data can be obtained with respect to the effectiveness of a prototype for multiple individual aspects.

#### **3.1 Electromagnetics Modeling**

COMSOL Multiphysics is a software package used for coupling and solving physics and engineering problems. COMSOL Multiphysics can also solve finite element analysis problems. Through the use of the COMSOL Multiphysics software package, many computer models can be generated and multiple aspects of physics can be coupled. In addition to this, designs can be optimized and new designs can be generated quickly. This makes the flow of design work more efficient with respect to time. A perfect example with the MET was the ability to model several configurations, optimize the dimensions, and adjust variables such as power input and microwave frequency.

COMSOL Multiphysics is broken up into multiple modules that can be used to solve several types of physics such as RF, MEMS, structural mechanics, and CFD; and then these modules can be coupled to couple the physics with the intent of working toward a comprehensive numerical model. The specific module used for the electromagnetics modeling was the RF module.

COMSOL Multiphysics works by generating a mesh over a specified geometry and then solving a specified partial differential equation (PDE) at each nodal point along the mesh. It uses a finite-difference approximation to solve the PDE, which is then placed into a matrix of the form  $\underline{A}\bar{x} = \underline{B}$ . Upon generating the  $\underline{A}$  matrix, a specified solver method is used to solve the sparse matrix. COMSOL Multiphysics gives multiple solver options for which to solve the matrices and each have their relative benefits for any given simulation or configuration. The primary solver used in the electromagnetics modeling was the Direct SPOOLES solver. SPOOLES stands for Sparse Object Oriented Linear Equations Solver and is used to solve real and complex linear systems of equations. SPOOLES uses a multifrontal method in conjunction with a direct LU factorization of the matrix.<sup>23</sup> This matrix is then solved in conjunction with the boundary conditions which are presented in the next section.

### 3.1.1 Boundary Conditions

The initial step in generating the model was to create the geometry of the thruster. There are two methods in which the geometry can be created. The geometry can be created using a program such as SolidWorks and then imported into COMSOL Multiphysics. This method may be better if one prefers a specific drawing interface or needs to create a very complex geometry. Alternatively, the geometry can be drawn in COMSOL Multiphysics using its geometry generation tools. The latter method was used in generating the models in this research. Figure 3.1 is the geometry for the current MET configuration.

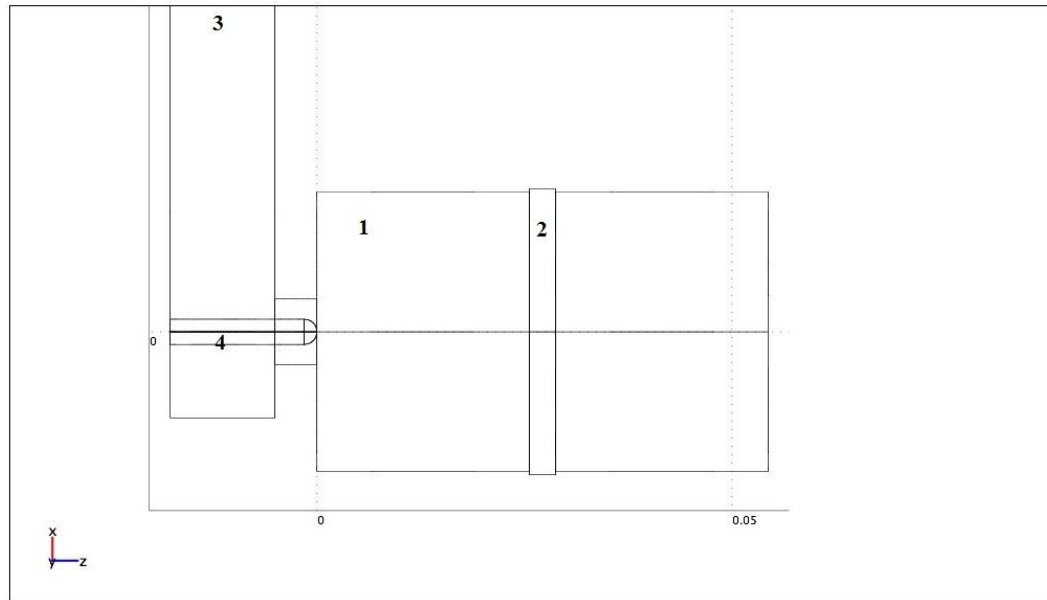


**Figure 3.1** Geometry of the MET.

After creating the geometry, the next step is to specify the subdomain and boundary conditions. The subdomain allows one to specify things such as the materials used and their particular properties and the boundary conditions allow one to give initial conditions and impose constraints for the simulation. The subdomain details for this simulation correspond to the labeling in Figure 3.1 and were specified as followed:

- 1) The chamber is specified as a vacuum.
- 2) The dielectric is made of boron nitride with a dielectric constant of 3.7.
- 3) The waveguide is specified as a vacuum.
- 4) The antenna is made of copper.

COMSOL Multiphysics includes a materials database that has vast amounts of information regarding the properties of multiple materials and those that are not listed in this database can be entered manually, as was the case with the boron nitride dielectric.

Next, the boundary conditions were specified. The boundary conditions detail how the geometry of the model behaves and interacts with respect to the overall system. The boundary conditions for this simulation correspond to the labeling in Figure 3.1 and were specified as followed:

- 1) The walls of the conductor are specified as a perfect electrical conductor.
- 2) The dielectric is specified as a matched boundary condition, where<sup>17</sup>

$$E_x = \frac{200x}{x^2 + y^2} \quad (3.1)$$

$$E_y = \frac{200y}{x^2 + y^2} \quad (3.2)$$

$$E_z = 0 \quad (3.3)$$

The constant is the 200 W power input.

- 3) The upper end of the waveguide is specified as a rectangular port with an input power of 200 W.
- 4) The antenna is a perfect electrical conductor.

When specifying the waveguide as a port, this is where the microwave signal is introduced at a frequency that can be specified. The microwave frequency can be set up to sweep over a given range of frequencies. This can be very advantageous when trying to determine a resonant

frequency for a given cavity configuration without having to run dozens of simulations independently.

### 3.1.2 Mesh Set Up

The manner in which the mesh is set up is critical for obtaining an accurate solution. If the mesh is too coarse, the solution will be inaccurate and if the mesh is too fine, one of two things will occur. Either the solution may take a long time to run or the computer will run out of memory while attempting to formulate the matrix, so it is important to generate a sufficient matrix while avoiding generating one that will run for a long duration without giving a sufficient increase in the accuracy of the numerical solution. COMSOL Multiphysics features a mesh generation tool that makes generating a mesh more simplistic than what other software packages may offer. The number of mesh elements varies based upon the geometric configuration. The meshes used were generally comprised of about 20,000 tetrahedral elements with roughly 4100 mesh point and 130,000 degrees of freedom. The degrees of freedom represent unknowns at given nodal points. Below is the mesh for one of the cases.

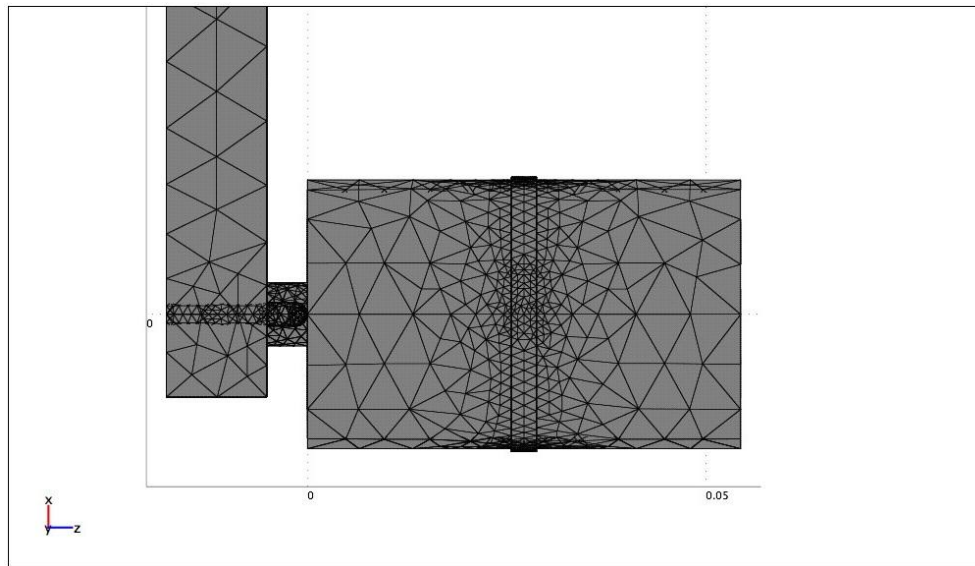


**Figure 3.2** Meshed Geometry of MET.

The average time that the electromagnetic simulations took was about 45 minutes to an hour for a machine with a 2.0 GHz core duo processor and 2 GB of memory, although some configurations can greatly exceed this.

### 3.2 Fluid Mechanics Modeling

COMSOL Multiphysics was also used for the fluid mechanics analysis of the propellant injection system. This, however, was much more tedious than the electromagnetics modeling due to the lack of support in COMSOL Multiphysics (3.5a) for compressible fluid flows. Within the fluid analysis, several models were created using a few different methods and techniques. The geometric and meshing setups were similar, but the methods of imposing the boundary conditions were different. The three models generated were: 1) a 3-dimensional viscous incompressible flow simulation of the propellant injection system, 2) a 3-dimensional viscous weakly compressible ( $M < 0.3$ ) flow simulation of the propellant injection system, 3) a 2-dimensional viscous compressible flow simulation, and 4) a 3-dimensional viscous compressible flow simulation. The SPOOLES solver was used for the 3D incompressible fluid flow and the 3D weakly compressible flow simulations. The UMFPACK solver was used for the 2D compressible flow simulation. UMFPACK is a solver for unsymmetric sparse linear systems using an unsymmetric multifrontal method. PARDISO was used for the 3D compressible flow simulation. PARDISO stands for Parallel Direct Solver and is a solver used for solving large sparse symmetric and unsymmetric systems of equations.

#### 3.2.1 Boundary Conditions

The initial setup was to create the geometry for the simulation. The built-in geometry generation tools were used to generate the portion of the chamber where propellant injection takes place. This geometry was used for the cases mentioned above of the 3-dimensional incompressible flow and weakly compressible simulations. The 2-dimensional compressible flow simulation modeled flow through a cylinder and a converging nozzle. The 3-dimensional compressible flow simulation modeled flow through a 3-dimensional cylinder and converging nozzle. Figure 3.3 represents the geometry for the propellant injection system which comes after the dielectric plate in which the full MET configuration can be seen in Figure 3.1.

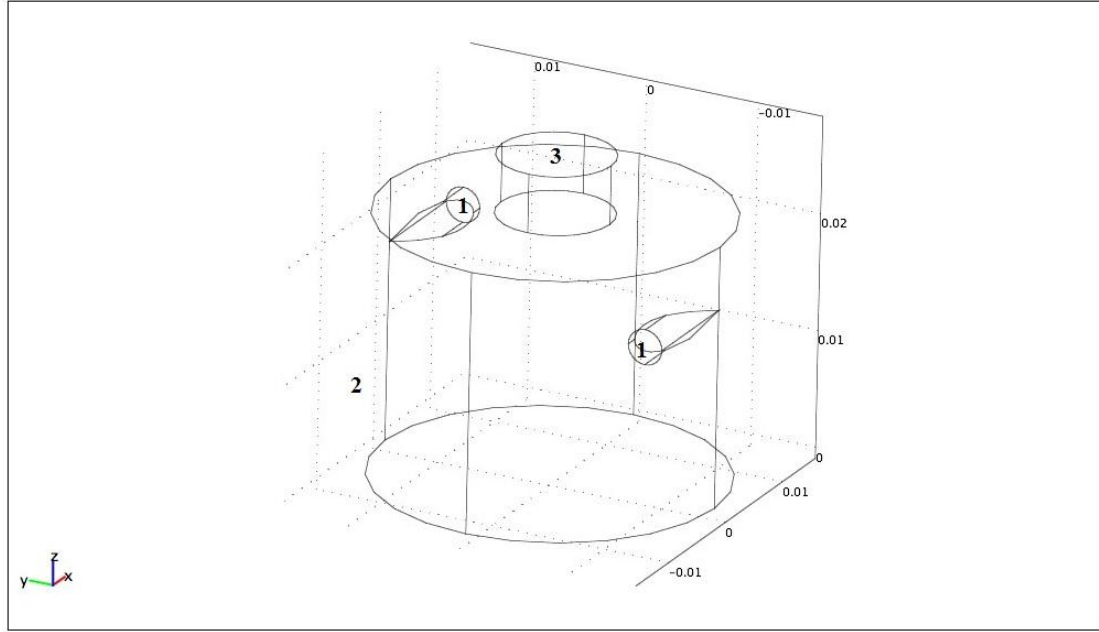


**Figure 3.3** 3D propellant injection system of MET.

### 3.2.1.1 3D Incompressible Flow

COMSOL Multiphysics features an incompressible Navier–Stokes module in which incompressible flows can be modeled. In this simulation, the density of the propellant is held constant. The geometry shown in Figure 3.3 was used in the 3D incompressible flow simulation. After creating the geometry, the subdomain and boundary conditions were specified. The subdomain of this module differs from that of the electromagnetics model in that, instead of describing the characteristics of the materials, the characteristics of the fluid were detailed. The density,  $\rho$ , of air at standard temperature and pressure was used in this simulation and thus the density used was  $1.23 \text{ kg/m}^3$ . The viscosity,  $\mu$ , chosen was very small and modeled to be about  $1.8 \times 10^{-1} \text{ Pa}\cdot\text{s}$ . The initial pressure,  $P$ , in the chamber is roughly 1 atm or  $10^5 \text{ Pa}$ . After this, the boundary conditions were specified. The boundary conditions for this simulation correspond to the labeling in Figure 3.3 and were specified as followed:

- 1) The inlet where the propellant is introduced is set as an inlet with an injection velocity of 0.554 m/s.
- 2) The walls of the chamber were modeled as walls with a no slip condition.
- 3) The nozzle of the chamber was modeled as an outlet with a pressure of 0 Pa and no viscous stresses.

### 3.2.1.2 3D Weakly Compressible Flow

In addition to the Incompressible Flow module, a CFD module is also available and features the ability to solve incompressible flows and weakly compressible flows. The term “weakly compressible” is another way of stating that the program handles flows with Mach numbers,  $M$ , less than 0.3. This is used because densities below this Mach number are hardly variable and remain relatively static. One can also enable a turbulence model type. From this option, RANS smoothing was selected. RANS stands for Reynolds Averaged Navier–Stokes and is used in computer simulations to smooth out a result. The geometry in Figure 3.3 is used in this simulation. The subdomain and the boundary conditions are almost identical to that of the 3D incompressible flow simulation. The boundary conditions for this simulation correspond to the labeling in Figure 3.3 and were specified as followed:

- 1) The inlet where the propellant is introduced is set as a velocity inlet with an injection velocity of 0.554 m/s.
- 2) The walls of the chamber were modeled as walls with a no slip condition.
- 3) The nozzle of the chamber was modeled as an outlet with a pressure of 0 Pa and no viscous stresses.

### 3.2.1.3 2D Compressible Flow

The approach to modeling fully compressible flow in COMSOL Multiphysics was different than using either the CFD turbulent flow module or the incompressible Navier–Stokes module in the respect that the entire simulation was built from its foundation upward. COMSOL Multiphysics features a partial differential equation (PDE) module that one can use to create simulations that are not yet supported by COMSOL Multiphysics by entering equations manually. Using the PDE module, a fully compressible flow module was built.

The initial step was to create the geometry using the same methods as previously. Figure 3.4 shows the geometry for the 2D viscous compressible flow simulation.

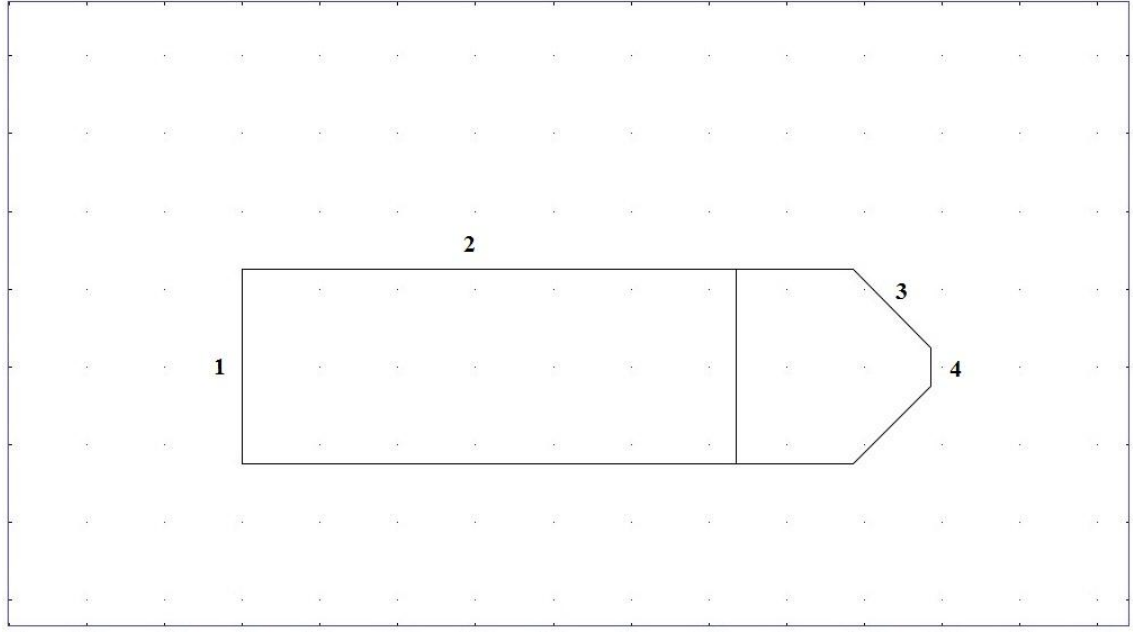


**Figure 3.4** 2D cylinder with converging nozzle.

After generating the geometry, the subdomain and boundary conditions were specified. Rather than simply characterizing the fluid via specifying density, pressure, and velocity as was done previously, more set up needed to be done. First, the governing equations of a fluid in 2 dimensions had to be derived. The assumption of a steady flow with “no slip” on the walls was assumed. From here, the equations of mass, momentum, and energy were derived in 2D. Secondly, when instantiating the module, one had to specify the variables being used for the simulation in order to build the basic framework of the simulation. The variables used were  $\rho$ ,  $u$ ,  $v$ , and  $p$ . The governing equations were entered when specifying the subdomain. The manner in which the equations are entered in COMSOL Multiphysics are of the form  $\nabla \Gamma = F$ , with  $F$  being the source term and  $\nabla \Gamma$  is a flux vector where the equations are entered in a form in which the partial derivative can be taken in the  $x$ ,  $y$ , and  $z$  directions. The initial conditions of the fluid can be entered in the constants list in COMSOL Multiphysics. The initial conditions of the domain can be entered directly into the subdomain conditions. After this, the boundary conditions for this simulation correspond to the labeling in Figure 3.4 and were specified as followed:

- 1) Inlet where  $\rho = 1$ ,  $u = 1$ ,  $v = 0$ , and  $p = 10^5$
- 2) Wall where  $\rho = \text{unspecified}$ ,  $u = 0$ ,  $v = 0$ , and  $p = \text{unspecified}$
- 3) Wall where  $\rho = \text{unspecified}$ ,  $u = n_x \sqrt{u^2 + v^2}$ ,  $v = n_y \sqrt{u^2 + v^2}$ , and  $p = \text{unspecified}$



- 4) Outlet where  $\rho = 0$ ,  $u = \text{unspecified}$ ,  $v = \text{unspecified}$ , and  $p = 0$

The general equation for the boundary conditions is of the form

$$-n \cdot \Gamma = G + \left( \frac{\partial R}{\partial u} \right)^T \mu; \text{ with } R = 0 \quad (3.4)$$

where the boundary conditions were entered in  $R$ .

### 3.2.1.4 3D Compressible Flow

After developing a working 2-dimensional simulation, the model was expanded to 3 dimensions in order to move closer toward integrating the viscous compressible flow module with the MET fuel injection system. The governing equations derived in the 2D model were expanded to 3 dimensions using the same assumptions of a steady flow with “no slip” on the walls. Next, the PDE module was modified to account for the extra velocity term  $w$ , making the variables  $\rho$ ,  $u$ ,  $v$ ,  $w$ , and  $p$ . The geometry was then modified to account for the extra dimension as displayed in Figure 3.5.

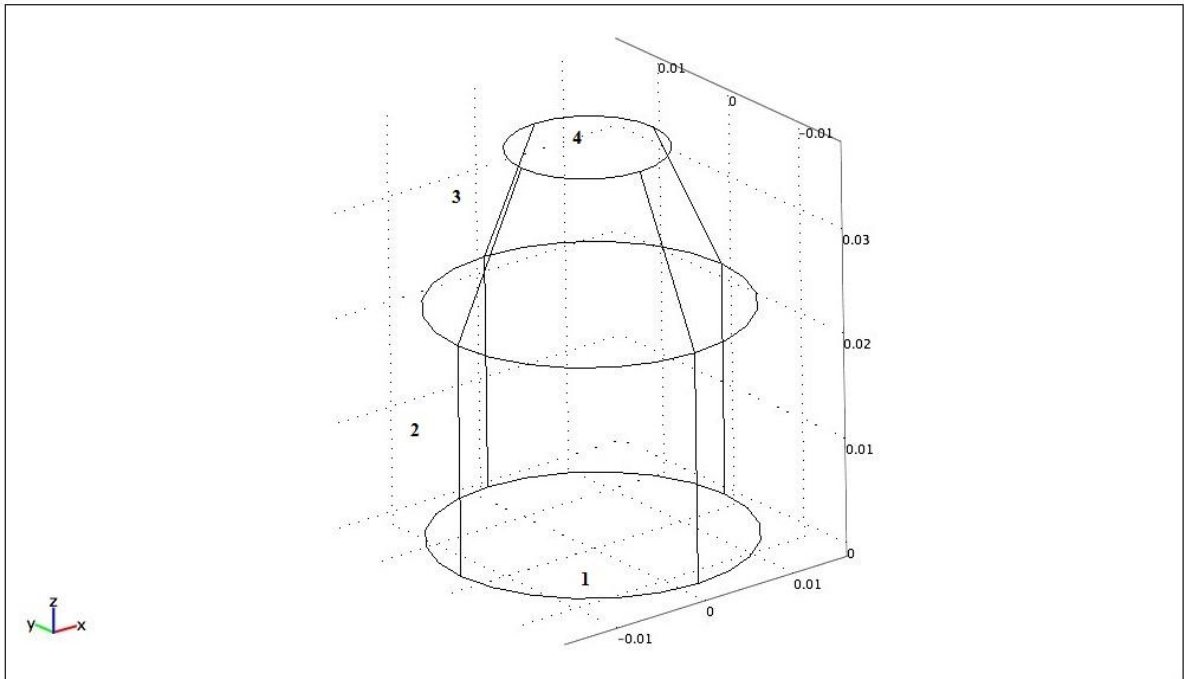


**Figure 3.5** 3D cylinder with converging nozzle.

After generating the geometry, the subdomain and boundary conditions were specified. The equations were entered into COMSOL Multiphysics in the same manner as with the 2D case.

The initial conditions of the fluid were entered into the constants list. The initial conditions of the domain can be entered directly into the subdomain conditions. After this, the boundary conditions for this simulation correspond to the labeling in Figure 3.5 and were specified as followed:

- 1) Inlet where  $\rho = 1$ ,  $u = 0$ ,  $v = 0$ ,  $w = 0.1$ , and  $p = 10^5$
- 2) Wall where  $\rho = \text{unspecified}$ ,  $u = 0$ ,  $v = 0$ ,  $w = 0$ , and  $p = \text{unspecified}$
- 3) Wall where  $\rho = \text{unspecified}$ ,  $u = 0$ ,  $v = 0$ ,  $w = 0$ , and  $p = \text{unspecified}$
- 4) Outlet where  $\rho = 0$ ,  $u = \text{unspecified}$ ,  $v = \text{unspecified}$ ,  $w = \text{unspecified}$ , and  $p = 0$

It can be seen that the boundary condition of the wall where the nozzle converges is specified as zero rather than a directional vector multiplied by the magnitude of the velocity. The method used to govern the direction of fluid flowing along the wall in the 2-dimensional case proved not to be effective in the 3D case and thus a form of smoothing was sought out to better direct the fluid flow and relax the streamlines from their erratic behavior. RANS smoothing was used to resolve this issue and once this method was implemented into COMSOL Multiphysics, the issue of the flow along the walls and erratic fluid streamline behavior was resolved.

### 3.2.2 Mesh Setup

The mesh setup had a great impact on the accuracy of the solution and whether it converged or not. The mesh generation tool in COMSOL Multiphysics was used to generate the mesh for the geometry. The coarseness of the mesh varied for each simulation. The mesh for the incompressible and weakly compressible flow simulations was finer because it was worth the increased solver time to obtain a more accurate result. When building the compressible flow module, it was most effective to use a coarser mesh so that the calculation time was short and multiple modifications could be made to the underlying code and streamline smoothing methodology.

#### 3.2.2.1 3D Incompressible Flow and 3D CFD Mesh

The built in mesh generation tools were used to set up the mesh in a similar manner as with the electromagnetics simulations. The mesh had roughly 13,400 tetrahedral elements with 63,000 degrees of freedom. Figure 3.6 shows the meshed geometry that was used for both the 3D incompressible flow and the 3D CFD simulations.

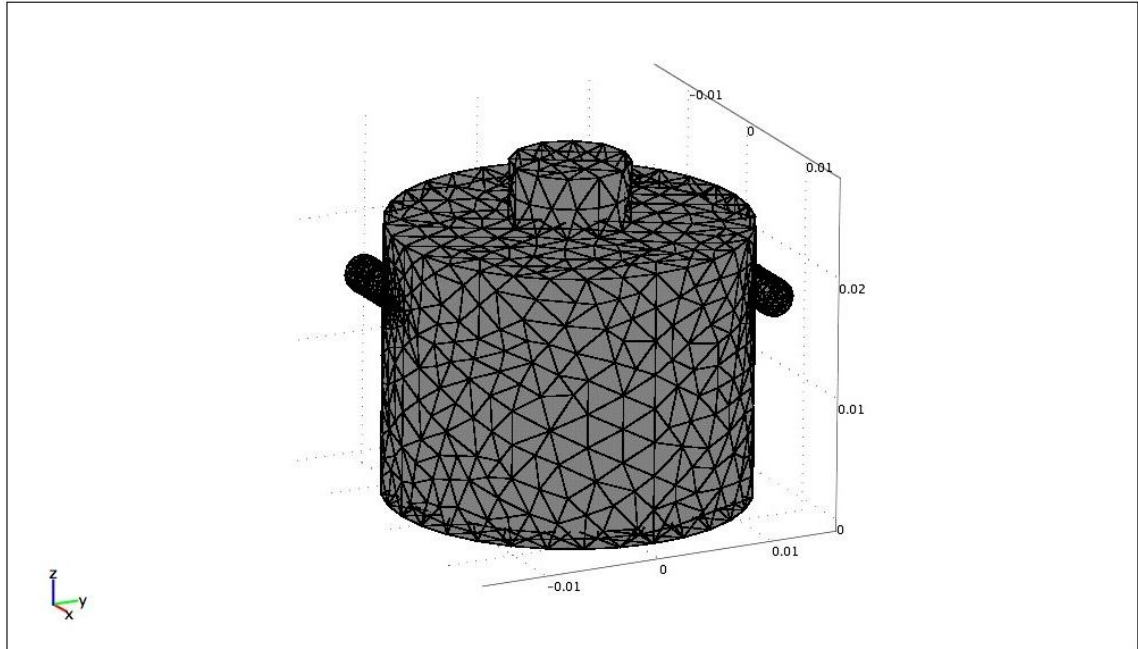


**Figure 3.6** Meshed geometry of 3D propellant injection system of MET.

The simulations for incompressible flow and weakly compressible flow took about 45 minutes to an hour to solve using this mesh set up.

### **3.2.2.2 2D Compressible Flow Mesh**

The mesh of the 2D case was the least complex in that the mesh used many fewer elements and degrees of freedom to accurately solve the simulation than for the 3-dimensional cases. The mesh generated was comprised of 950 triangular mesh elements with roughly 9,300 degrees of freedom. Figure 3.7 is the meshed geometry for the 2D compressible flow simulation.

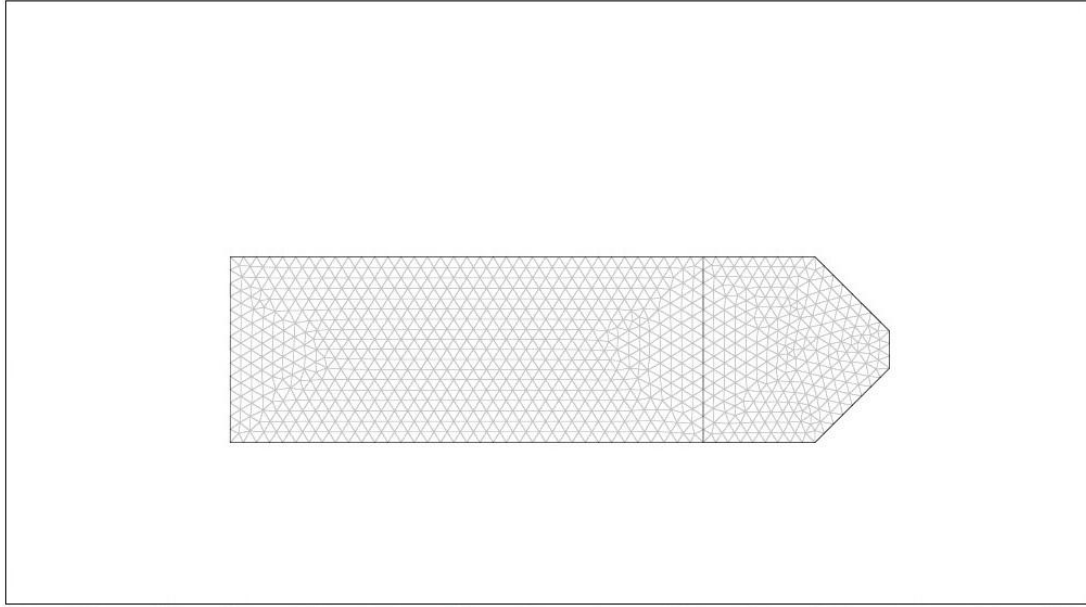


**Figure 3.7** Meshed geometry of the 2D cylinder with converging nozzle geometry.

Given that the 2D simulations used much fewer mesh points, the run time was also much less than the 3D cases and generally took on the order of a minute or so.

### **3.2.2.3 3D Compressible Flow Mesh**

The 3D compressible flow case used a mesh that was comprised of 7,300 tetrahedral mesh elements with 36,000 degrees of freedom. Figure 3.8 is the meshed geometry for the 3D compressible flow simulation.

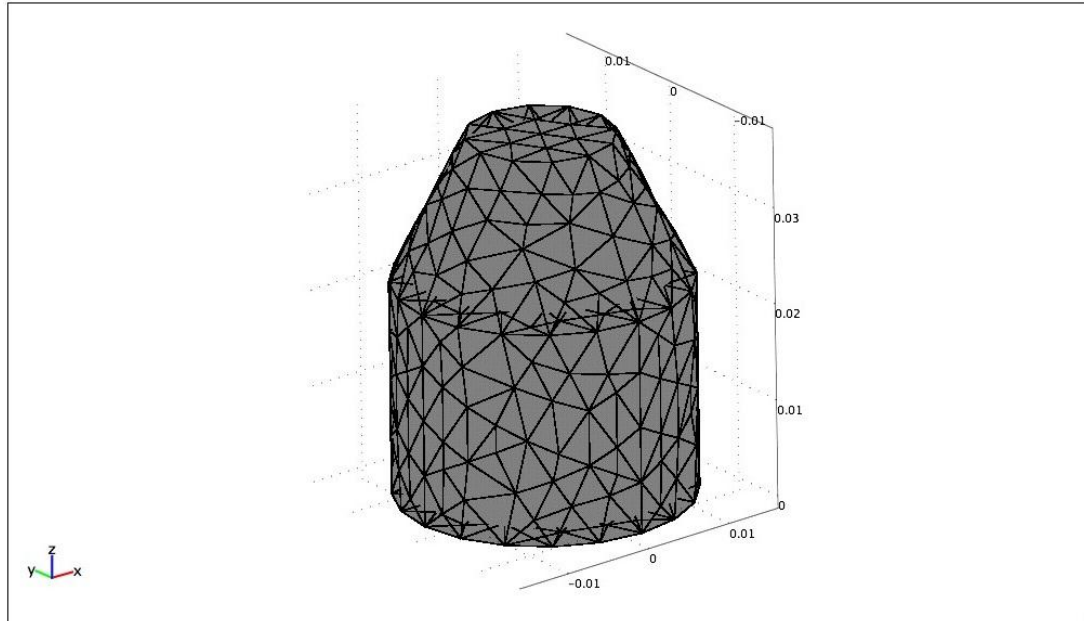


**Figure 3.8** Meshed geometry of the 3D cylinder with converging nozzle geometry.

The 3D compressible flow simulation generally took about 20 minutes to solve under these meshing conditions.

## **CHAPTER 4**

### **Results and Discussion**

#### **4.1 Electromagnetics Modeling**

The results of the electromagnetics modeling are presented in this section. The goal of the electromagnetics modeling was to choose an optimal configuration for the MET. Various tests were done with the electromagnetics modeling. Multiple methods of introducing the microwave energy were investigated. Some of these methods were: a coaxial port, a single waveguide, a double waveguide, a waveguide with a short, and a waveguide with a short and coaxial coupling. Optimizations of all of these methods were performed and include: materials, antenna depth, antenna shape, power input, waveguide length, waveguide type, and using a short and varying its length.

##### **4.1.1 Coaxial Modeling**

The initial objective was to model the electromagnetic effects within the MET. The next objective was to find the optimum frequency for a chamber using a coaxial port configuration. This was accomplished by generating plots of the EM Field vs. Frequency. In order to work toward finding the optimum frequency, an optimum configuration was also investigated. The different cases investigated were: the antenna length, antenna, shape, unloaded and loaded cavities, dielectric material and antenna shape.

##### **4.1.1.1 Unloaded Cavity with Variable Antenna Depth**

The beginning of the MET electromagnetic modeling began with modeling the MET without a dielectric. A study was performed with antenna depth and shape over a parametric sweep of frequencies to observe how the resonant frequency and relative intensity at the nozzle-end of the cavity varied. The two antenna shapes modeled were a rounded tip antenna and a flat tip antenna. Figure 4.1 shows the geometry for the flat tip antenna configuration and Figure 4.2 shows the geometry for the rounded antenna.

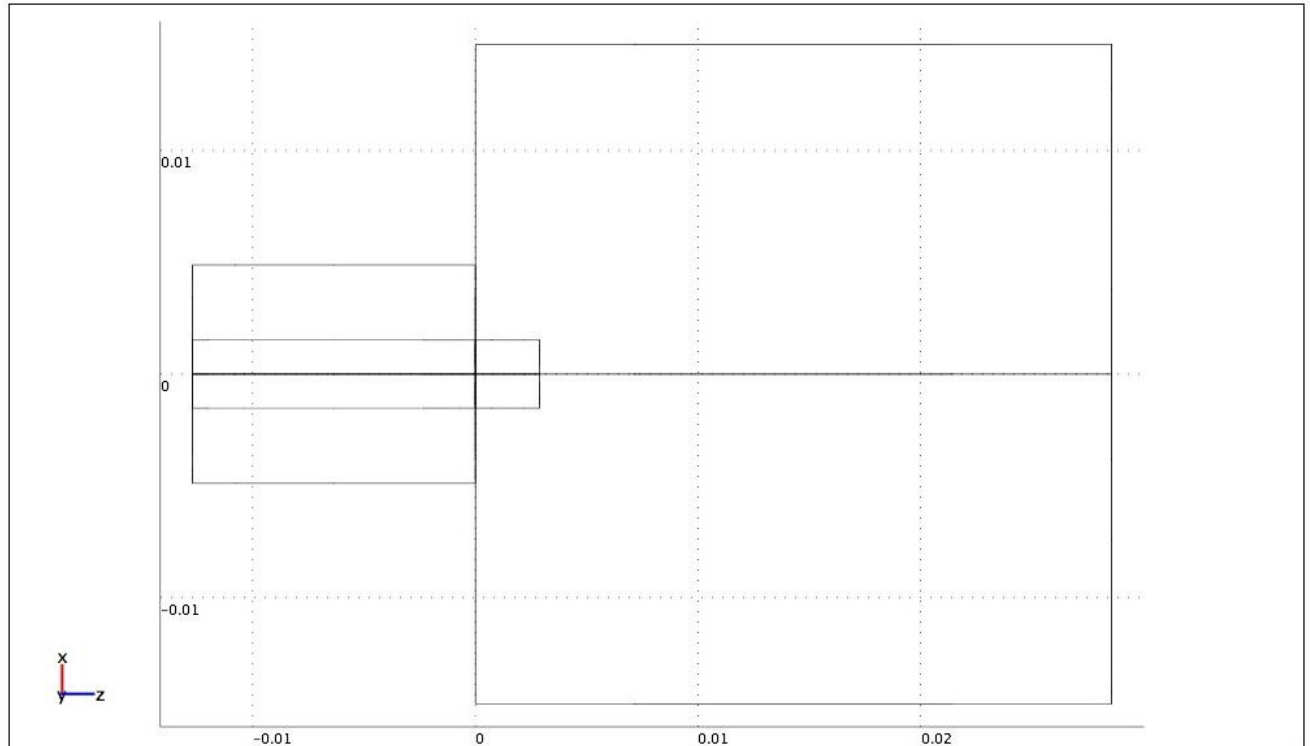


**Figure 4.1** Unloaded MET cavity with flat tip antenna.

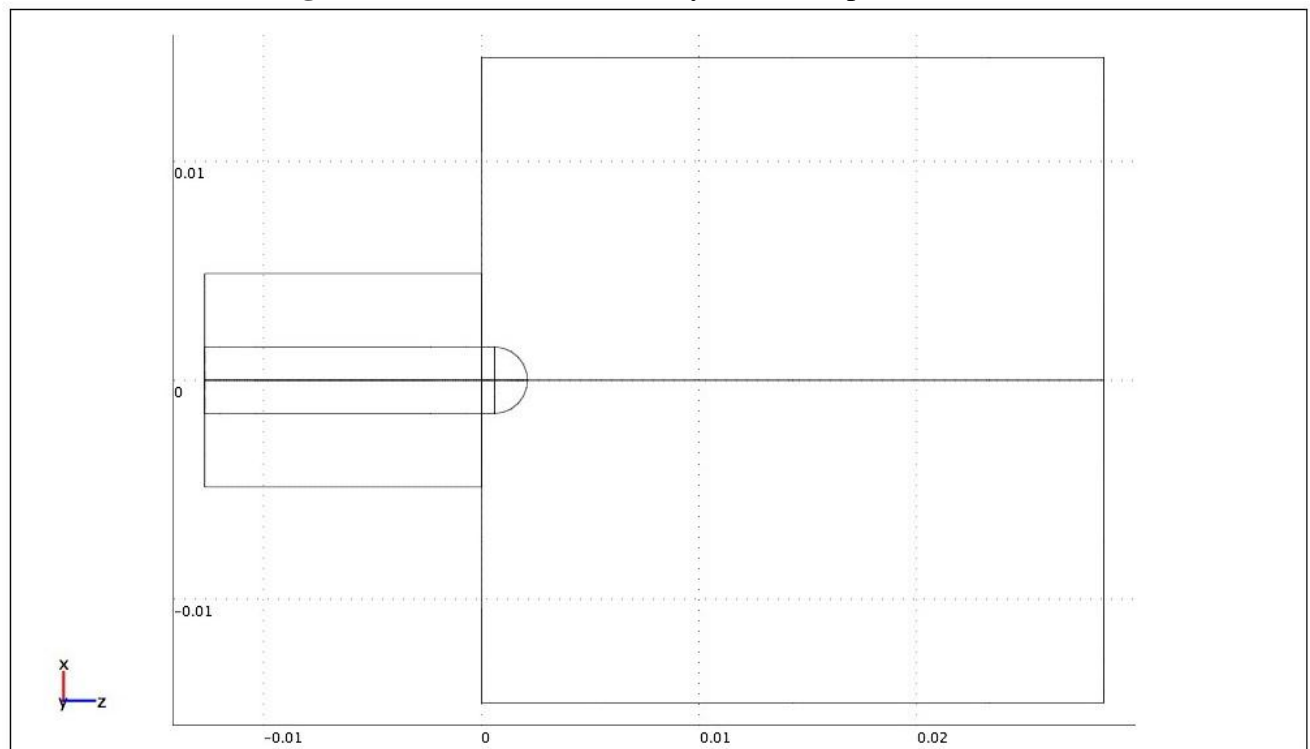


**Figure 4.2** Unloaded MET cavity with rounded tip antenna.

In this study, six antenna lengths were modeled and compared with four antennas having flat tips and the other two having rounded tips. The results of this comparison can be observed in Table 4.1. It is important to note that the depth as a percentage is relative to the baseline value as a percent increase in depth. Rounded and flat refer to the antenna shape as several models were made with both configurations.

**Table 4.1** Comparison of antenna depths for unloaded MET cavity

Antenna Depth	Resonant Frequency (GHz)	E-Field Intensity (kV/m)
Baseline (Flat)	9.40	327
11% (Rounded)	9.37	259
11% (Flat)	9.27	177
18.5% (Flat)	9.24	163
26% (Rounded)	9.17	149
37% (Flat)	8.83	130

From this table, one can see that, as the antenna depth increases, the resonant frequency decreases as does the electric field intensity. Another issue can be derived from the electric field results for an unloaded cavity. In the absence of a dielectric, breakdown can occur at the antenna, which causes degradation over time. The intensity at the nozzle end of the cavity can be increased significantly and the issue of breakdown can be averted through the introduction of a dielectric to the cavity. Having a dielectric in the cavity allows for a pressure differential between the antenna region and the nozzle region. This is advantageous because it can help inhibit breakdown and degradation. This helped conclude that using a dielectric was the best decision with respect to optimization and performance.

#### 4.1.1.2 Dielectric Material

Upon completing the unloaded cavity study of the MET, the next aspect investigated in order to find the optimum frequency was the dielectric material. Figure 4.3 shows the geometry of the chamber when loaded with a dielectric. The two dielectric materials investigated were quartz and boron nitride. The dielectric constant,  $\epsilon_r$ , of the quartz modeled was 4.2 and for boron nitride was 3.75. It was found that although the electric field intensity did not increase, the resonant frequency shifted depending on the dielectric material used. The cavity resonated at a higher frequency for the material with the higher dielectric constant, quartz. This effect can be observed in Figure 4.4.



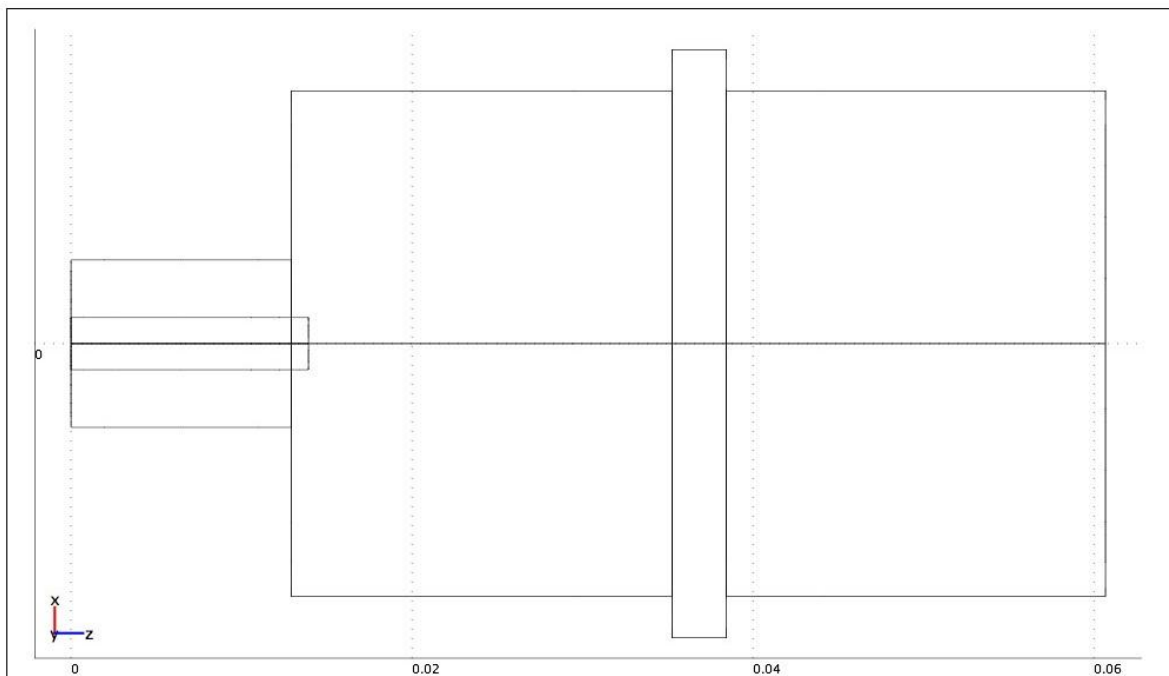


**Figure 4.3** Geometry of chamber loaded with dielectric.

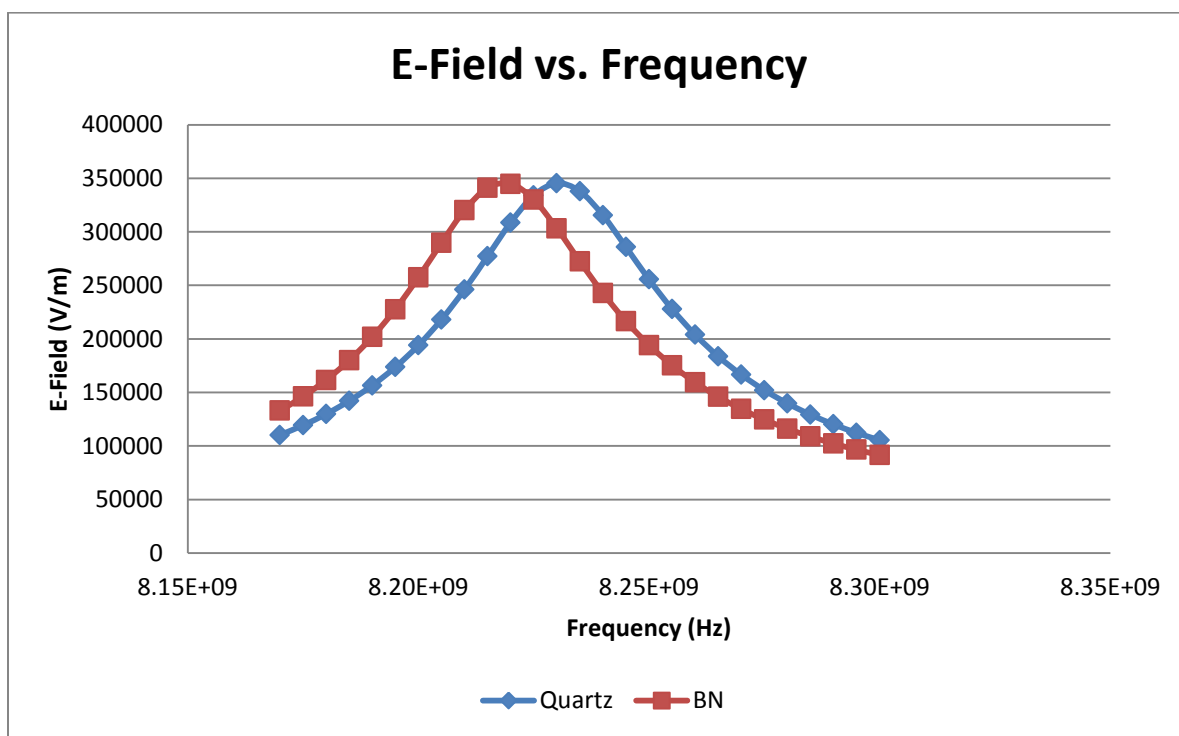


**Figure 4.4** Electric Field vs. Frequency for MET with varying dielectric materials.

#### 4.1.1.3 Optimized Coaxial Configuration

Figure 4.5 shows the contour plot of the E-field magnitude. The regions of a high E-field are concentrated at the antenna and the entrance to the nozzle. The chamber is made of stainless steel and its dimensions remain constant with all the electromagnetic modeling. The separation plate is composed of Boron Nitride (BN). The antenna was modeled with both a rounded tip and a flat tip. This particular model uses a flat tip antenna. Figure 4.6 shows a graph of the E-field vs. frequency. The peak is reached at an E-field intensity of  $3.485 \times 10^5$  V/m using the frequency 8.23 GHz. This peak is where the  $TM_{011}^z$  mode shape is represented the most intensely.

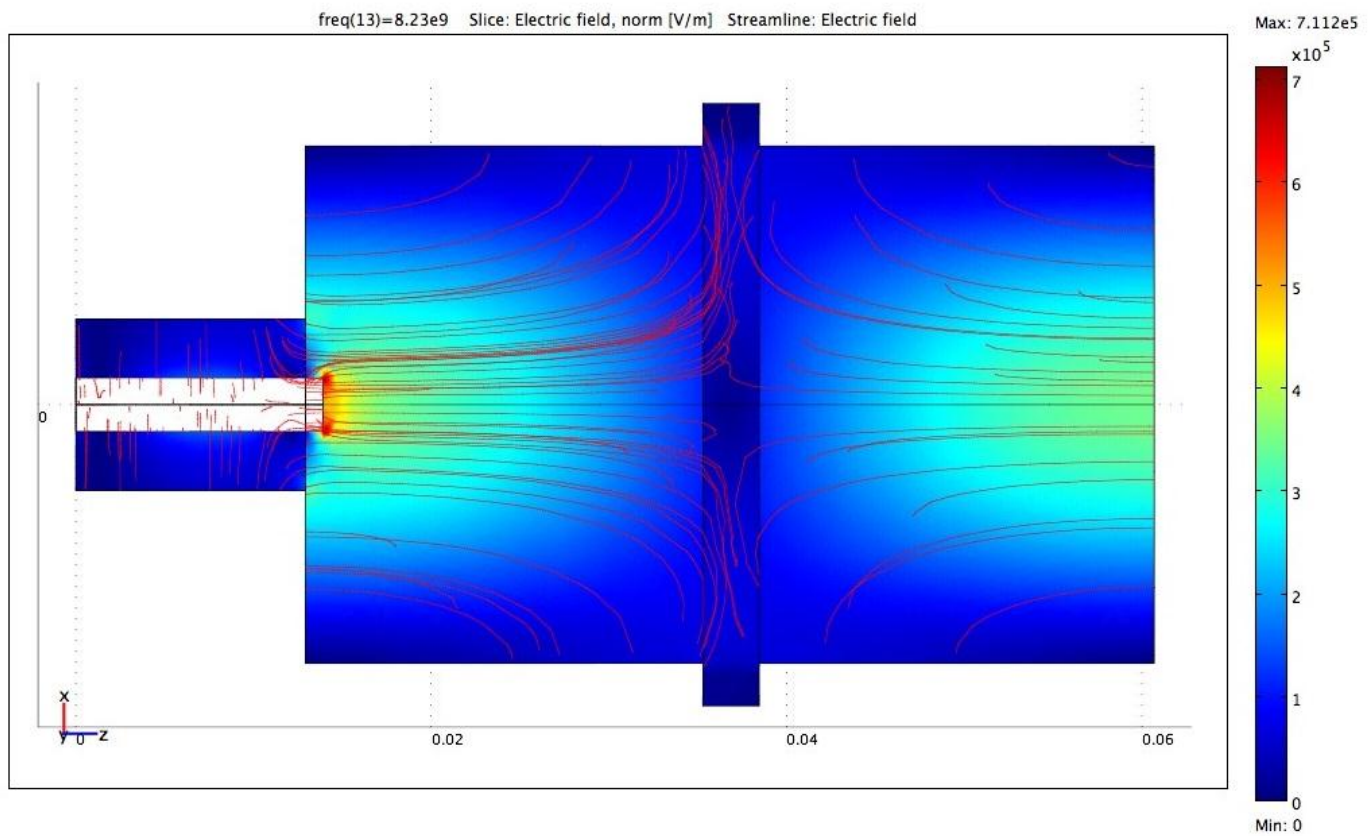


**Figure 4.5** Contour plot of the E-Field for a coaxial configuration.

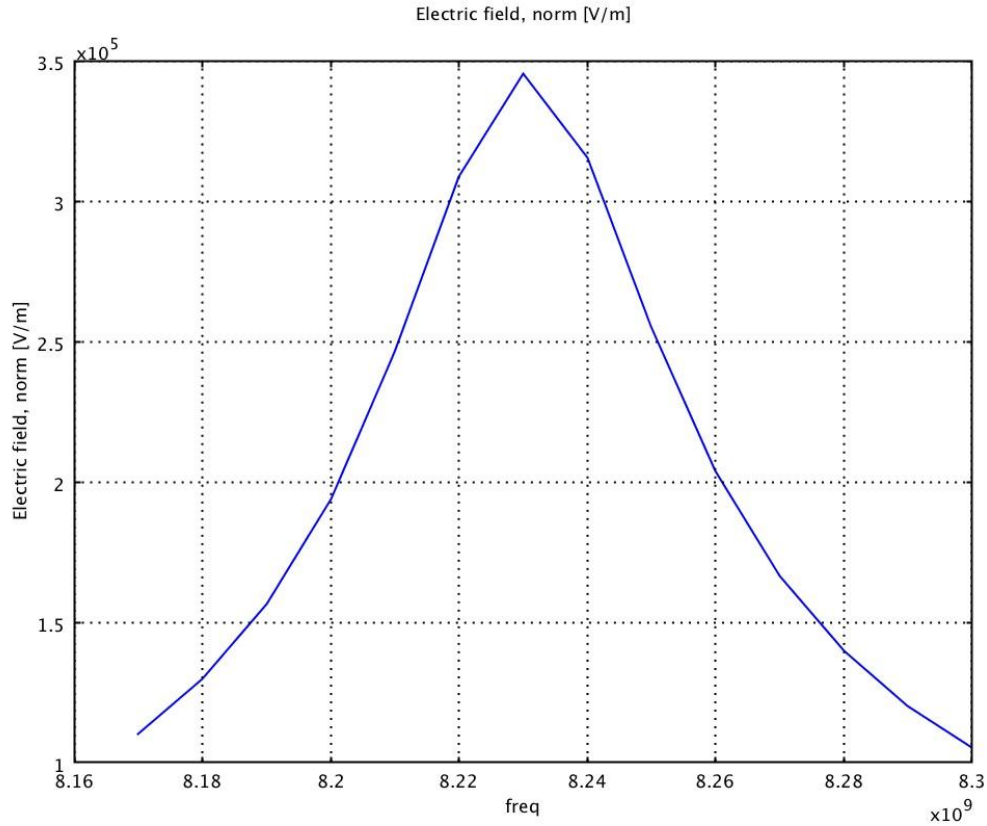


**Figure 4.6** Graph of E-Field vs. Frequency for the coaxial model.

#### 4.1.2 Single Direct Waveguide Input

The next set of electromagnetic modeling dealt with a waveguide configuration where the microwave energy is coupled to the chamber via a waveguide instead of a coaxial line.

##### 4.1.2.1 Waveguide Selection

Several different configurations were modeled using differently sized waveguides until the optimal result was found. These are: WR112 full height, WR112 half height, WR90 full height, and WR90 half height waveguides. Models were first completed with the WR112 and WR90 full height configurations. Figures 4.7 and 4.8 are the electric field result of the two full height waveguide configurations.

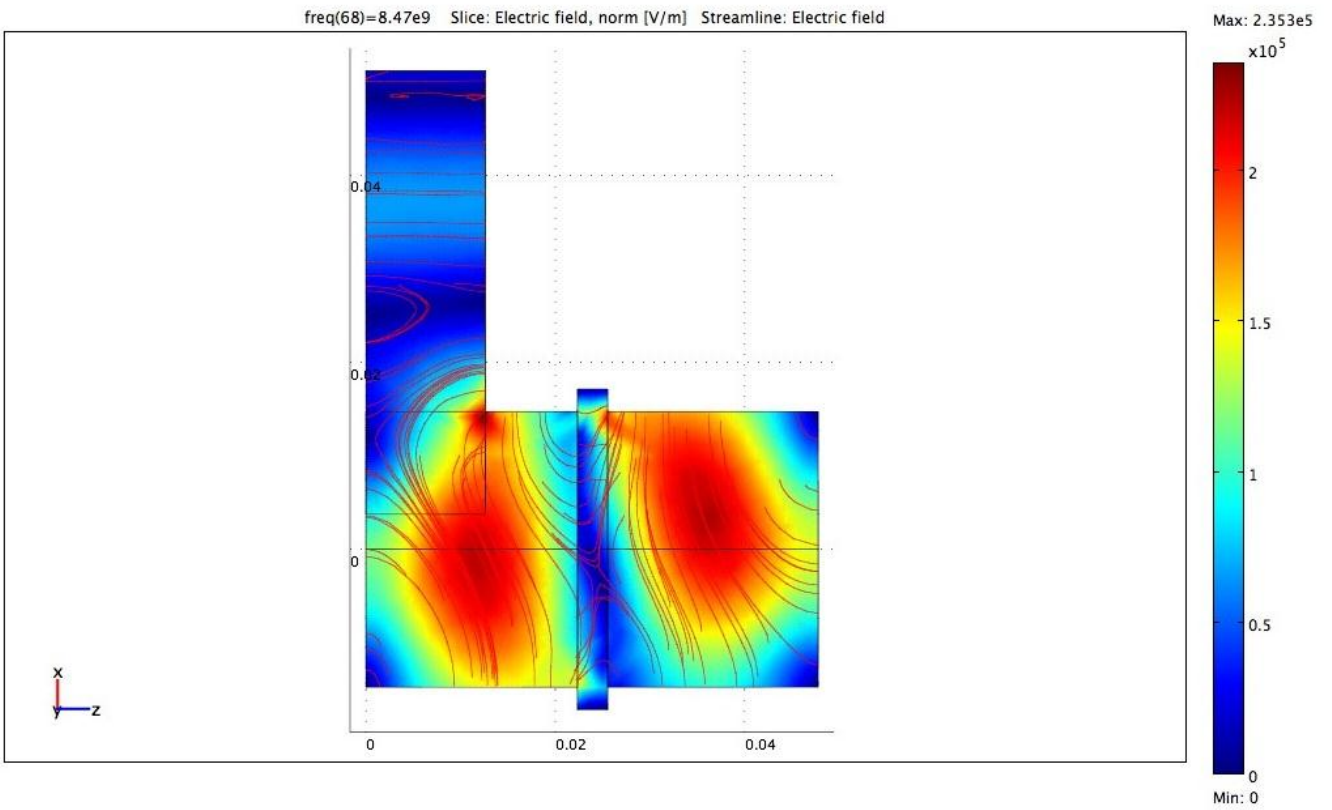


**Figure 4.7** Contour plot of the E-Field for the full-height WR112 single waveguide configuration.

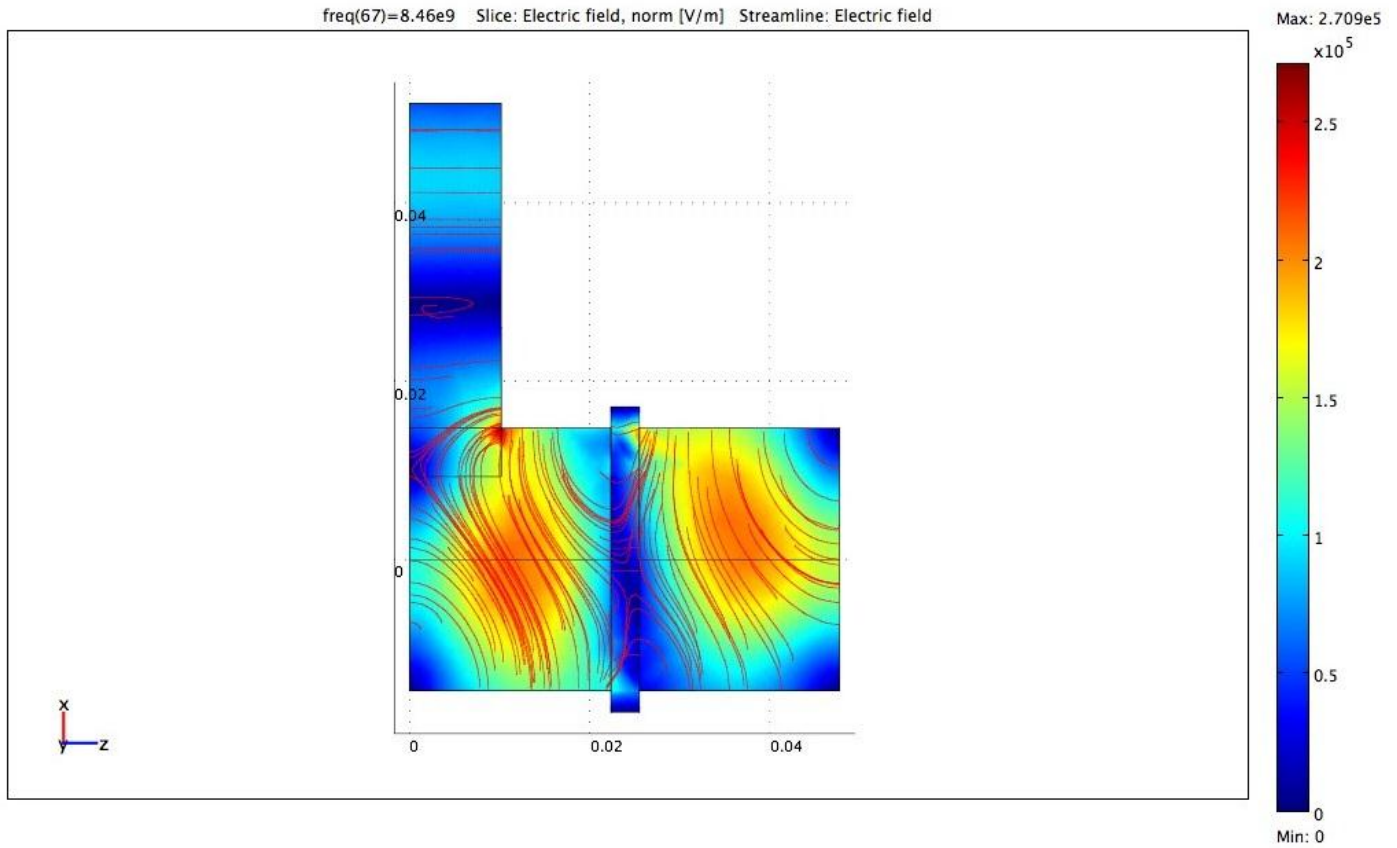


**Figure 4.8** Contour plot of the E-Field for the full-height WR90 single waveguide configuration.

One can see that in full height waveguide configurations, the electric field had a strong propensity to resonate at the  $TM_{012}^z$  mode shape. In order to move toward obtaining the  $TM_{011}^z$  mode, the half-height configurations were investigated and modeled. Figures 4.9 and 4.10 show the WR112 and WR90 half height configurations.

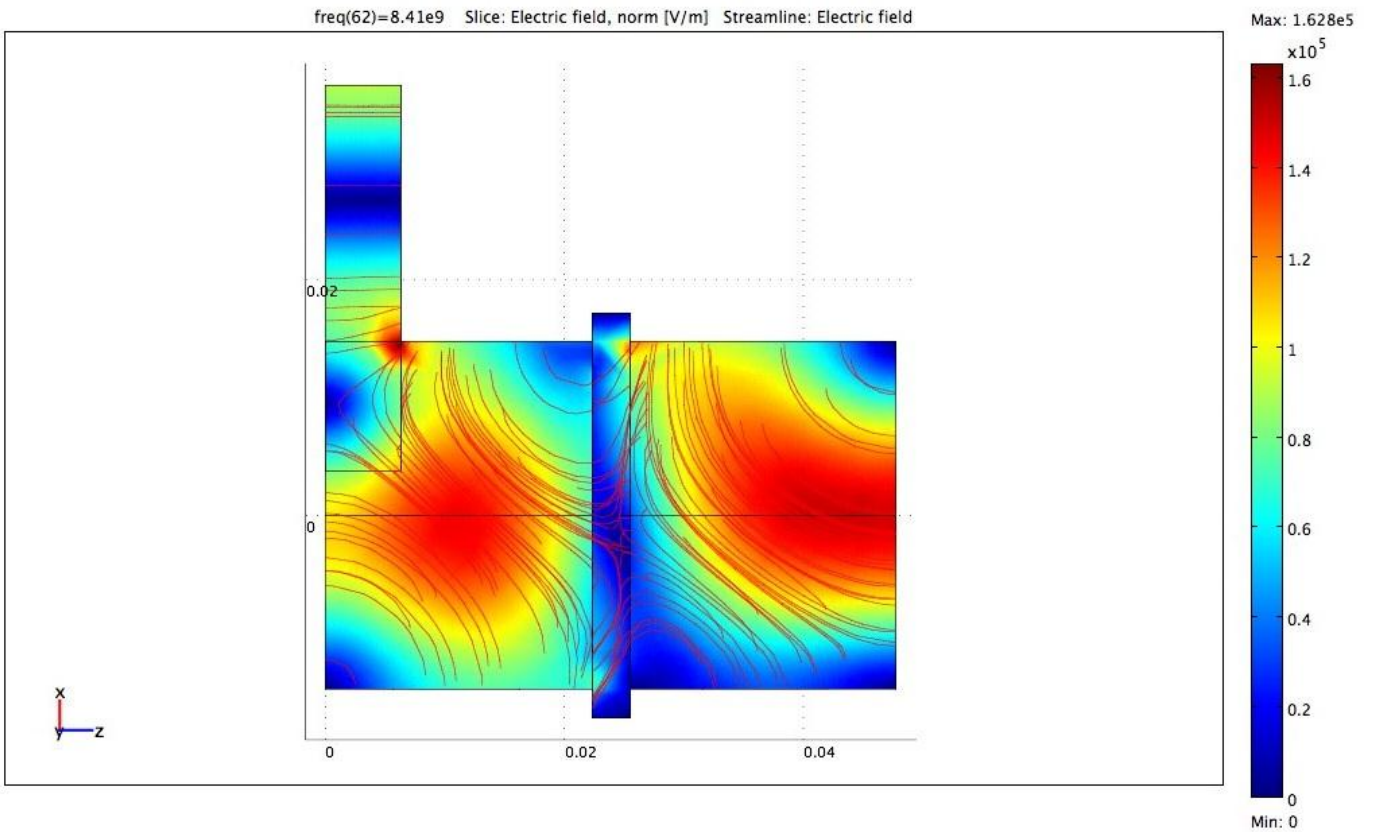


**Figure 4.9** Contour plot of the E-Field for the half-height WR112 single waveguide configuration.

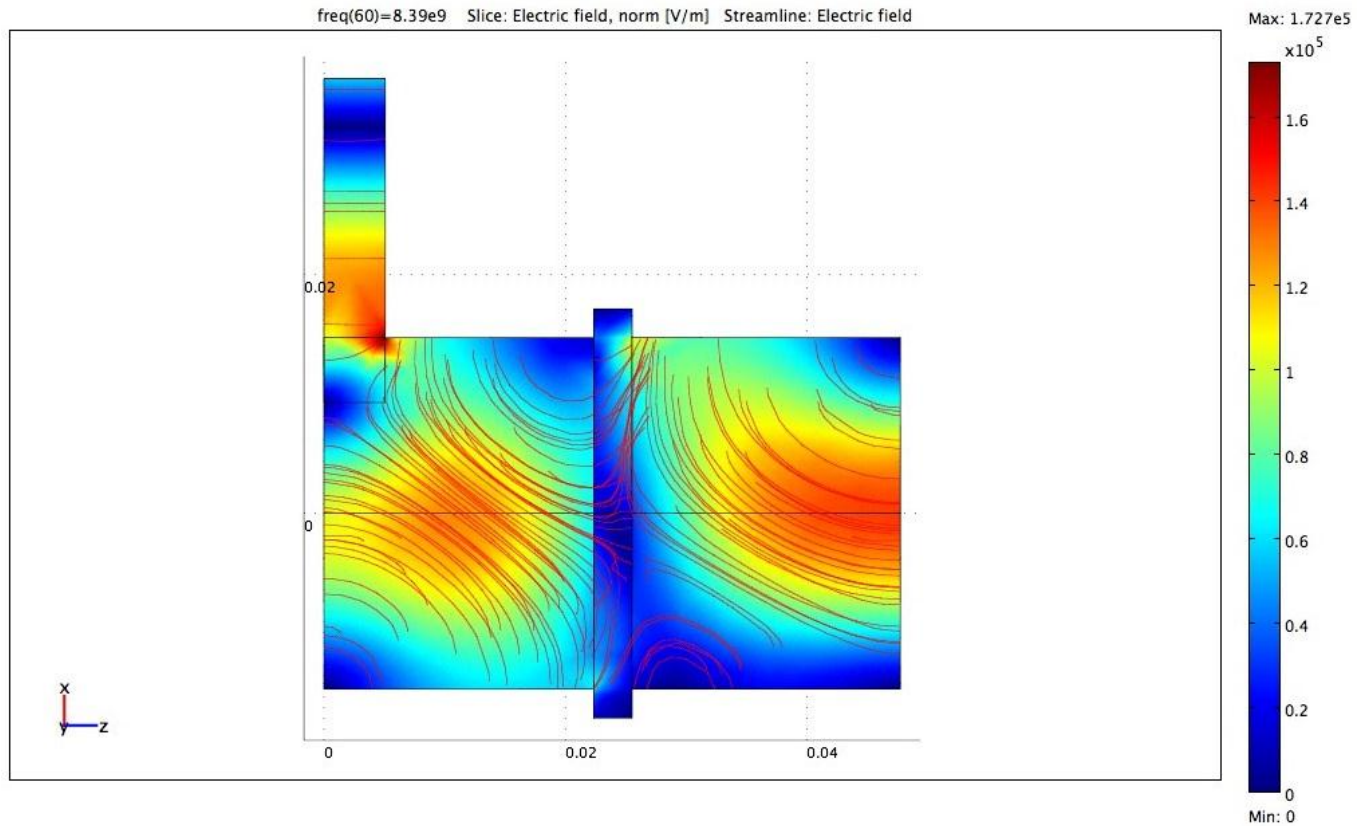


**Figure 4.10** Contour plot of the E-Field for the half-height WR90 single waveguide configuration.

Though there is more of an electric field concentration at the entrance of the nozzle, the mode shape is a hybrid between the  $TM_{011}^z$  and  $TM_{012}^z$  mode shapes and one can easily assume that this would be very unstable. A plot of the electric field vs. frequency can be observed in Figure 4.11 of all the single waveguide configurations.

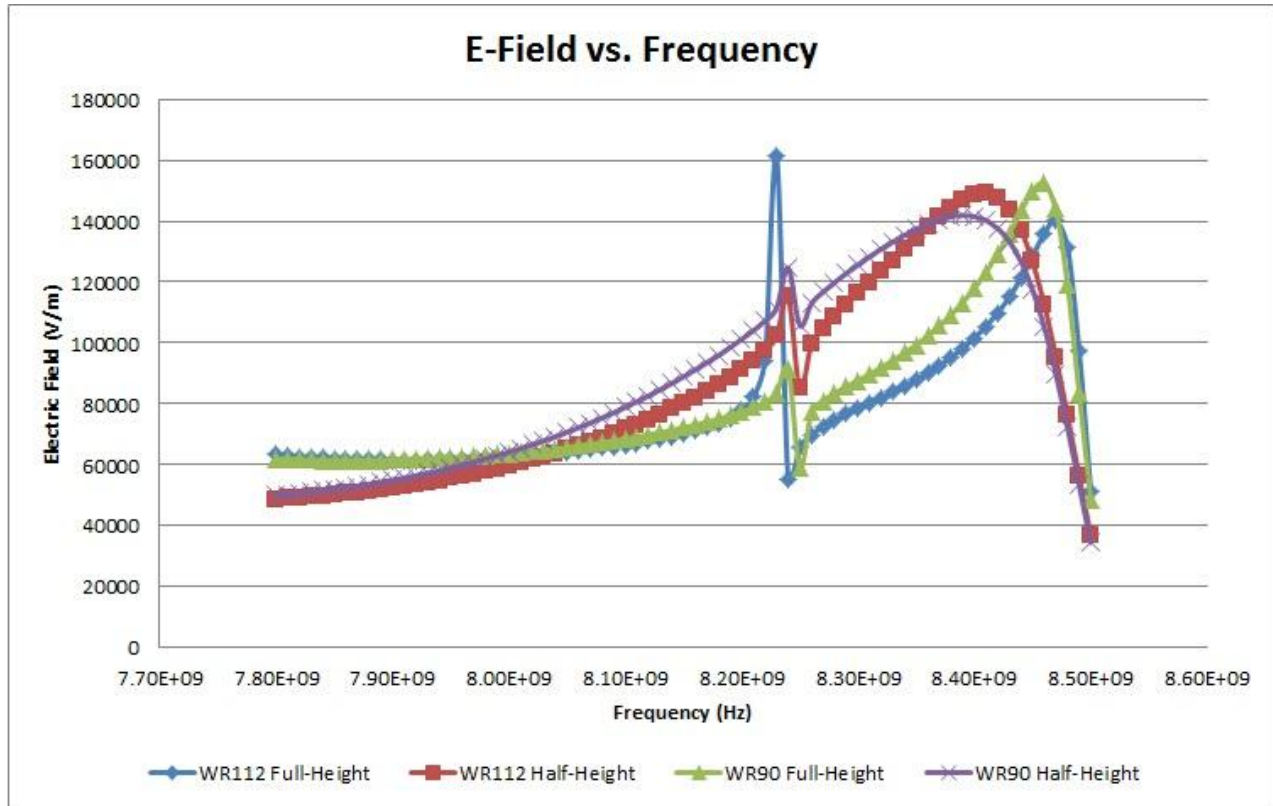


**Figure 4.11** Plot of E-Field vs. Frequency for the single waveguide configurations.

#### 4.1.2.2 Optimized Single Direct Waveguide Input Configuration

In the optimal configuration, the waveguide used in this particular model is a WR112 half-height waveguide. The width of the waveguide is 1.122 inches and the height is 0.2485 inches. The length used in this model is 1.434 inches. The dimensions of the chamber remain the same. The result of the single waveguide configuration can be seen in Figure 4.12. Finding a solid  $TM_{011}^z$  mode shape proved to be very difficult and thus this design was abandoned. Figure 4.13 shows the E-field vs. Frequency graph. The peak intensity was  $1.5 \times 10^5$  V/m at a frequency of 8.41 GHz.



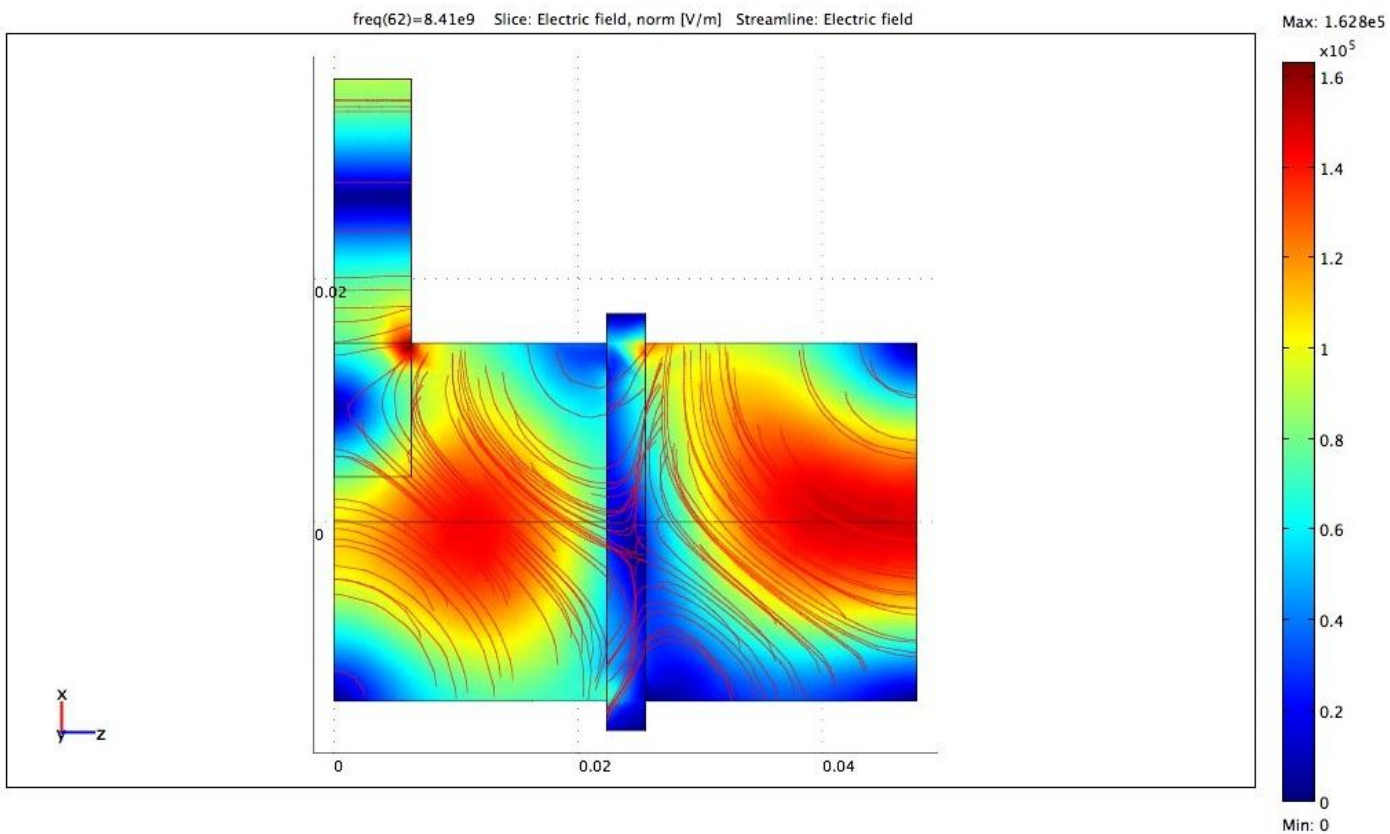


**Figure 4.12** Contour plot of the E-Field for a single waveguide configuration.

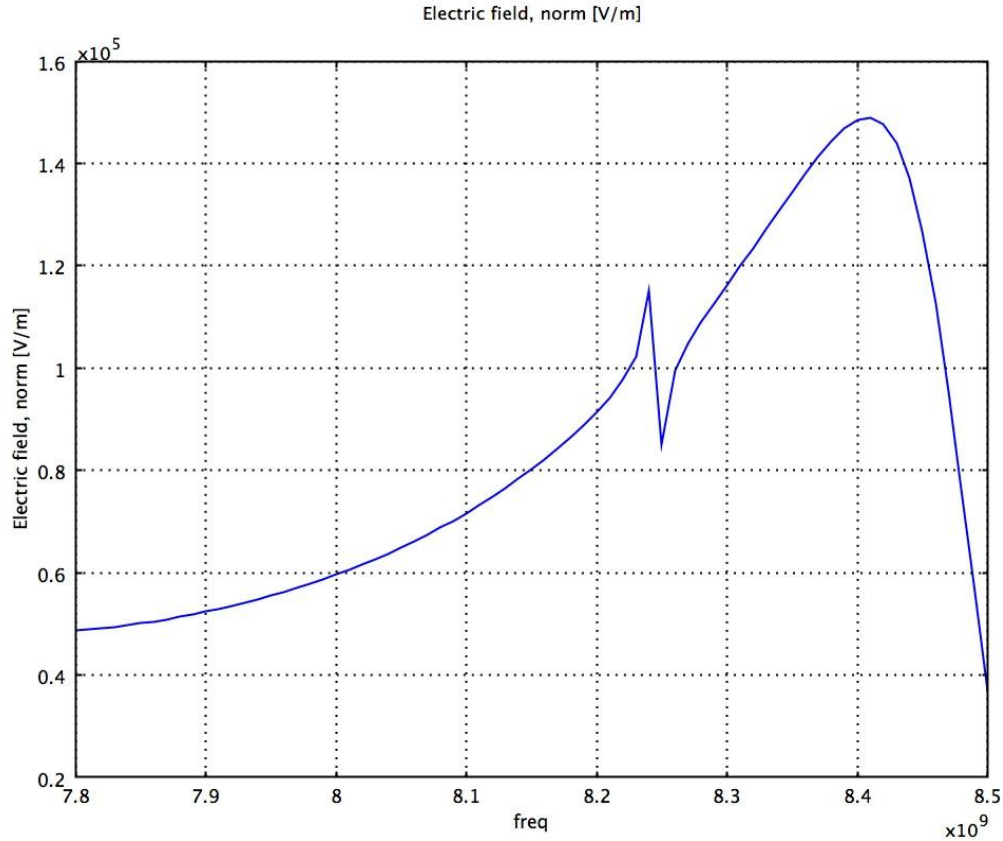


**Figure 4.13** Graph of E-Field vs. Frequency for the single waveguide model.

It can be seen from the modeling of the single waveguide configuration that the electric fields had two tendencies. The first proclivity is that the electric field generally resonated at the  $TM_{012}^z$  mode shape, which is not desired in this modeling. Through further modeling efforts, the  $TM_{011}^z$  mode was nearly obtained when modeling with the half height waveguide configurations, but a robust shape was never obtained. The second tendency for the electric field was arcing at the corner where the waveguide meets the cavity. This is obviously a characteristic to be avoided when designing a thruster in that one wants to avoid allowing potential sources of error to be present especially in design. Unfortunately, the issue of arcing was never resolved and this MET design configuration was abandoned.

#### 4.1.3 Double Direct Waveguide Input

The second waveguide model created was a double waveguide configuration where the energy is introduced from both waveguides equally. Both waveguides were placed on either side with the same length. The waveguide used was a WR90 half-height configuration. The width is 0.9 inches and the height is 0.2 inches. The length used was approximately 4.3 inches. The

length is long due to the fact that there was concern the microwaves were not completing a wavelength and thus 3 wavelengths were accommodated in the model. The chamber dimensions still remain the same. Looking at Figure 4.14, it can be seen that the intensity is concentrated in the center of each half of the chamber and this is not a desired result. Due to this result, another modification had to be implemented to correct this issue. Figure 4.15 is a graph of E-field vs. frequency for the double waveguide configuration. The peak E-field intensity is reached at 4800 V/m at a frequency of 8.5 GHz.

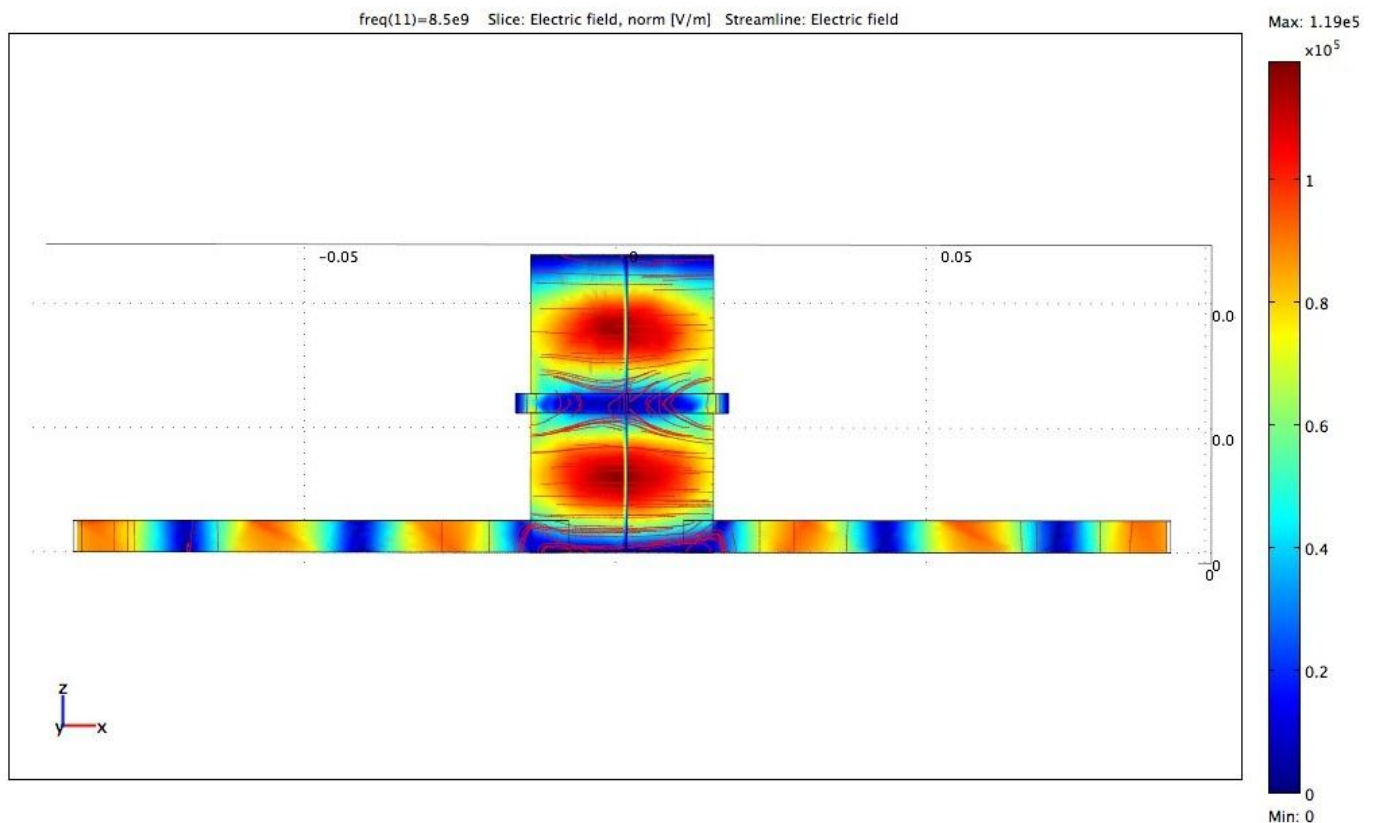


**Figure 4.14** Contour plot of the E-Field for a double waveguide configuration.

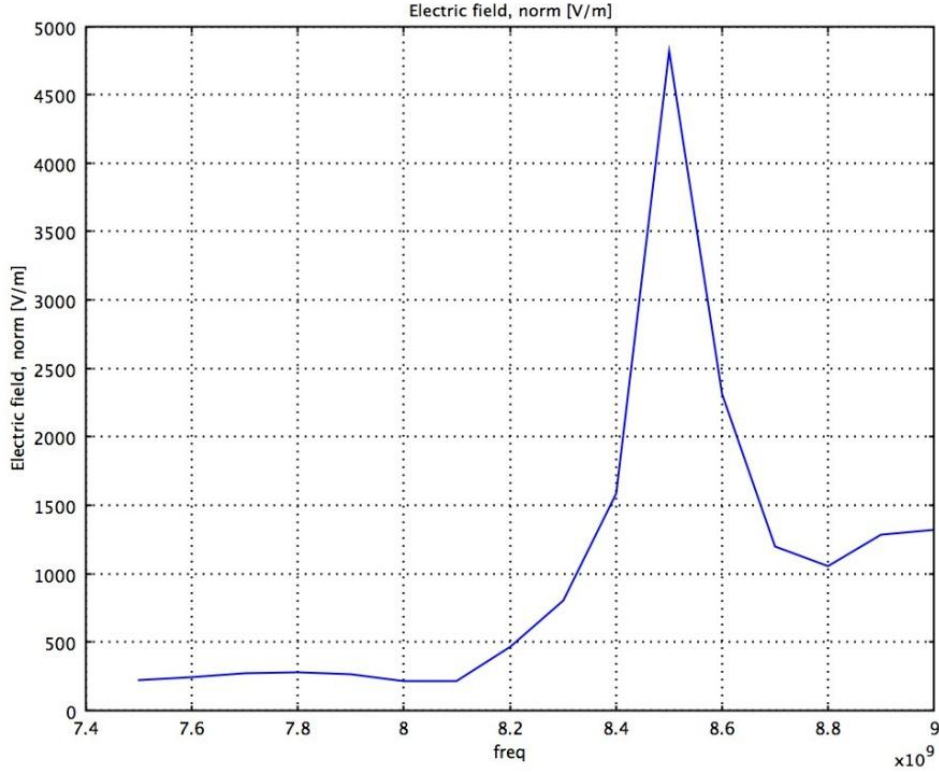


**Figure 4.15** Graph of E-Field vs. Frequency for the double waveguide model.

As was strongly present in the single direct waveguide input configuration, the double waveguide configuration resonates at the  $TM_{012}^z$  mode shape. This issue was more prevalent than for the single waveguide model in that it very strongly maintained its mode shape. Thus, this configuration was also abandoned.

#### 4.1.4 Single Direct Waveguide Input with Short

After modeling the single and double waveguide models, a slightly different approach was implemented in that a short was added to the single waveguide model with energy being introduced through one waveguide. A few different simulations were modeled in order to optimize the configuration. Some include: modeling the short at a variable length for a full and half-height WR90 configuration, modeling a quartz dielectric in the place of the short, and modeling with a sphere of conductivity to simulate the presence of a plasma.

##### 4.1.4.1 WR90 Full-Height with Variable Short Length

The initial modeling of the single waveguide mode with a short began with the full-height WR90 waveguide. An attempt was then made to optimize the configuration by adjusting the

length of the short until an optimized case was found. The waveguide was varied as a percentage of the full length waveguide where power was entering the system. This length was varied from 40–60% of the input waveguide's length and these results are shown in Figures 4.16–4.21.

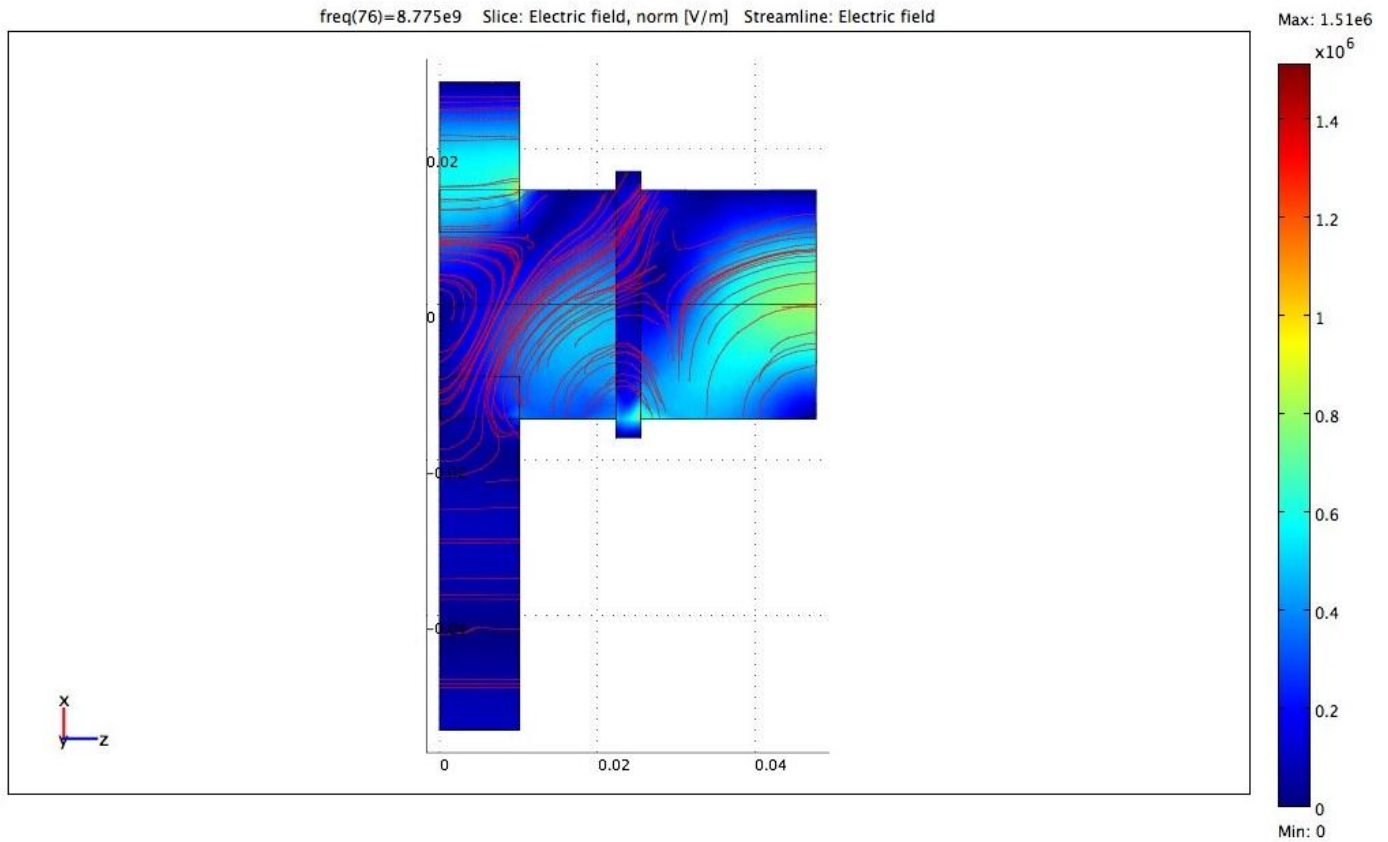


**Figure 4.16** WR90 full-height with 40% length short configuration.

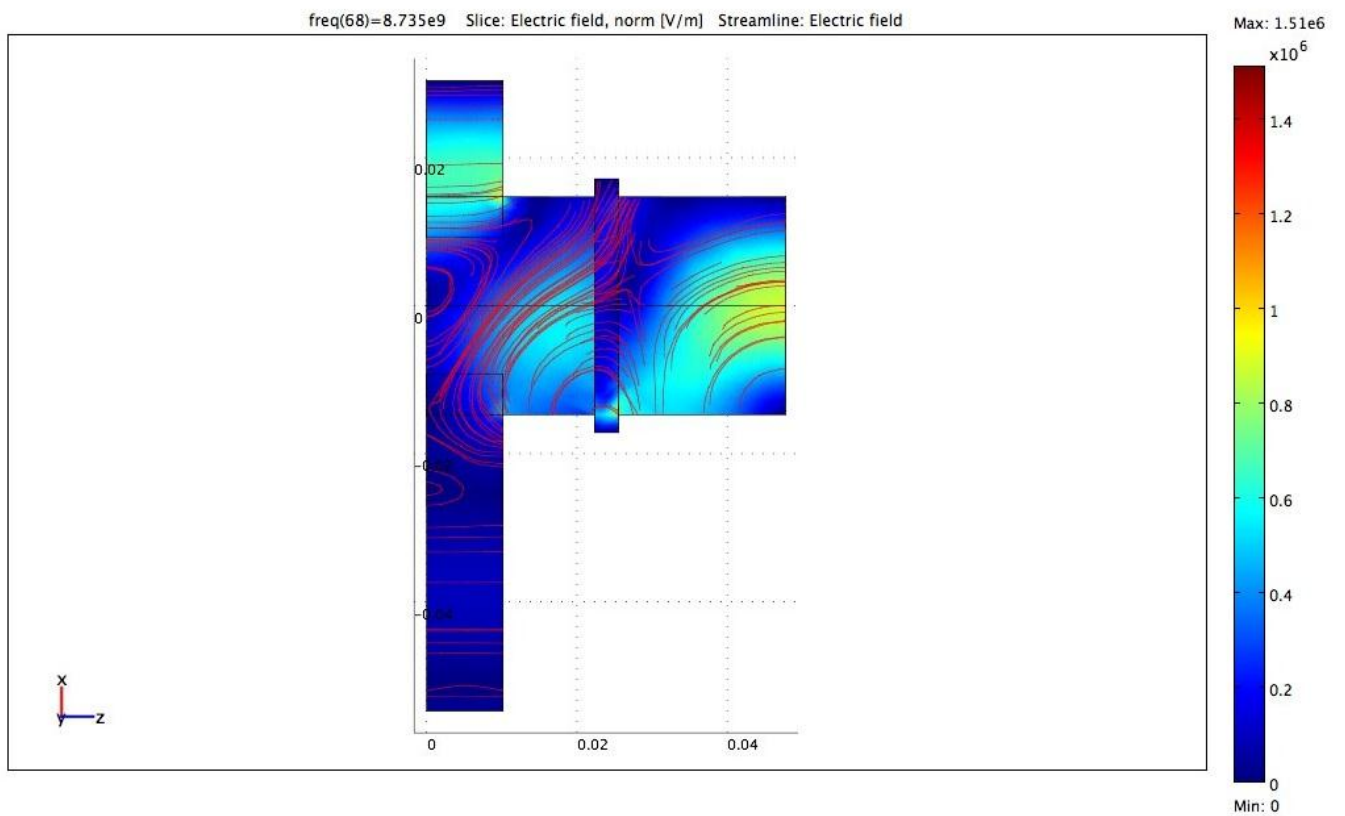


**Figure 4.17** WR90 full-height with 45% length short configuration.

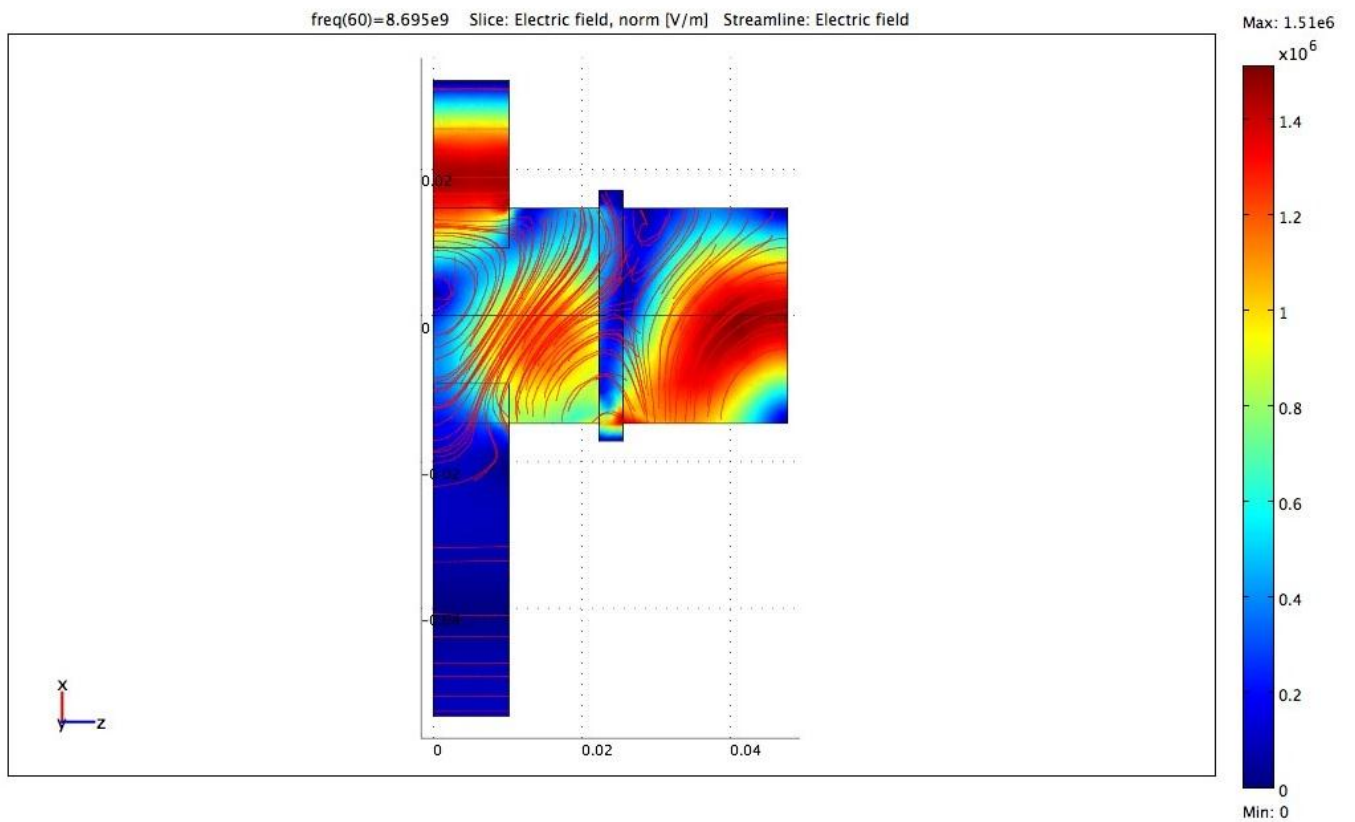


**Figure 4.18** WR90 full-height with 50% length short configuration.

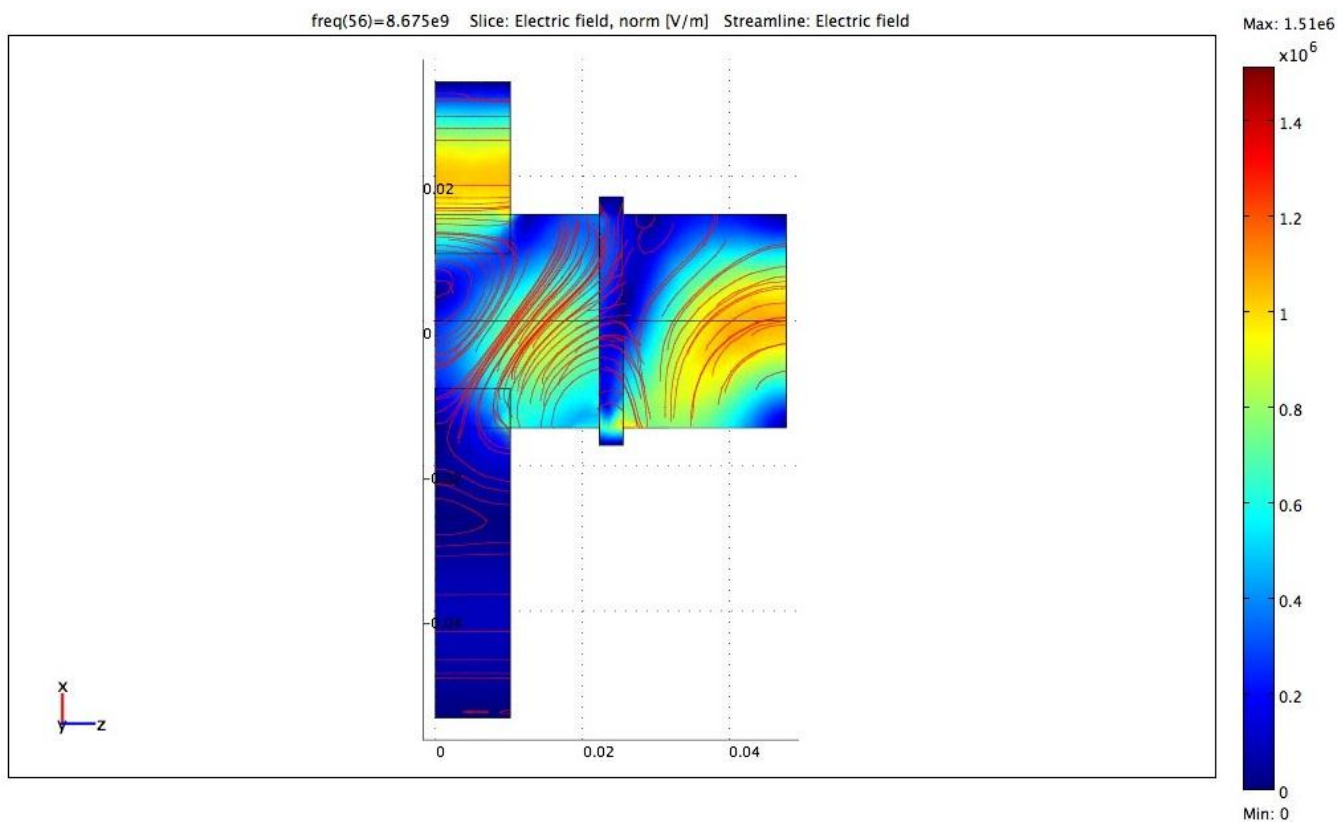


**Figure 4.19** WR90 full-height with 52.5% length short configuration.



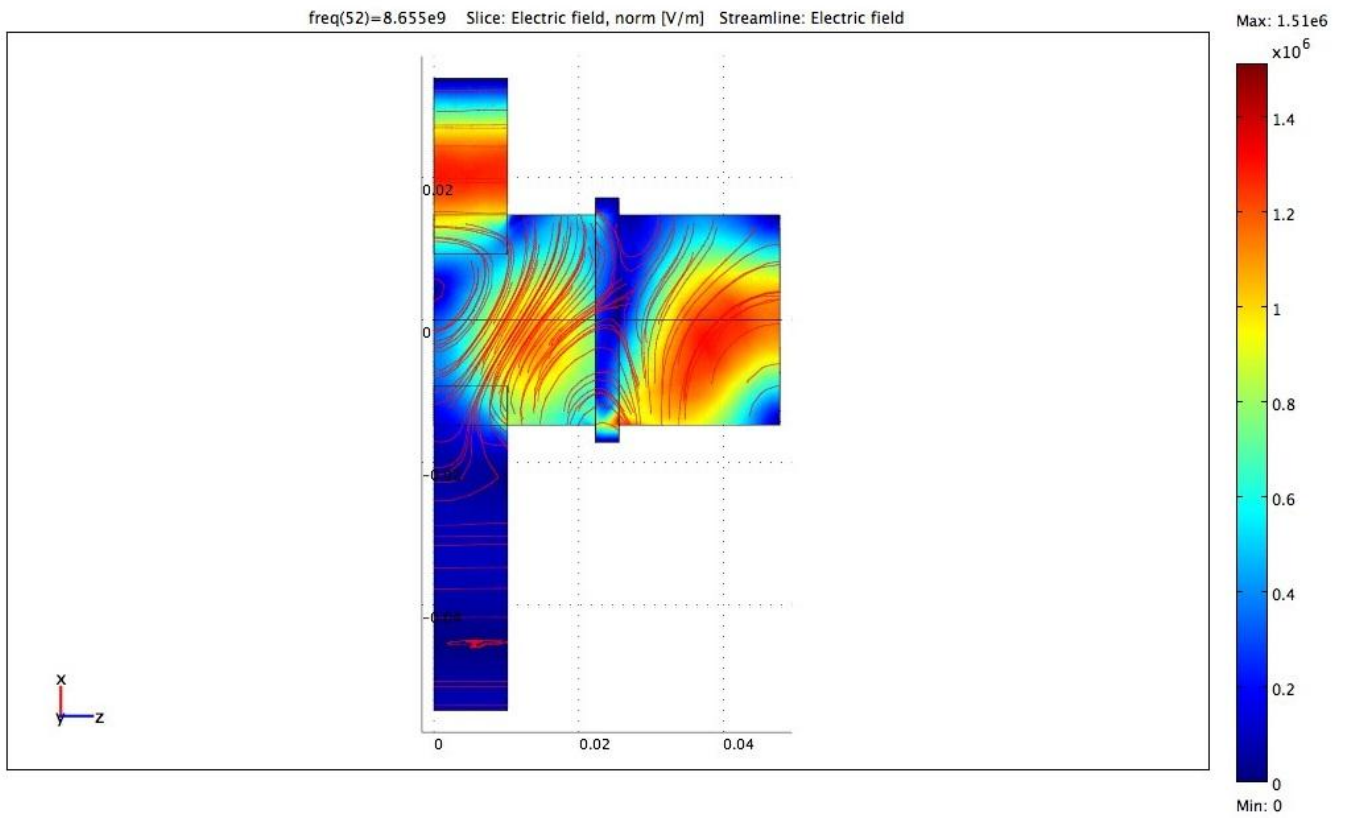


**Figure 4.20** WR90 full-height with 55% length short configuration.

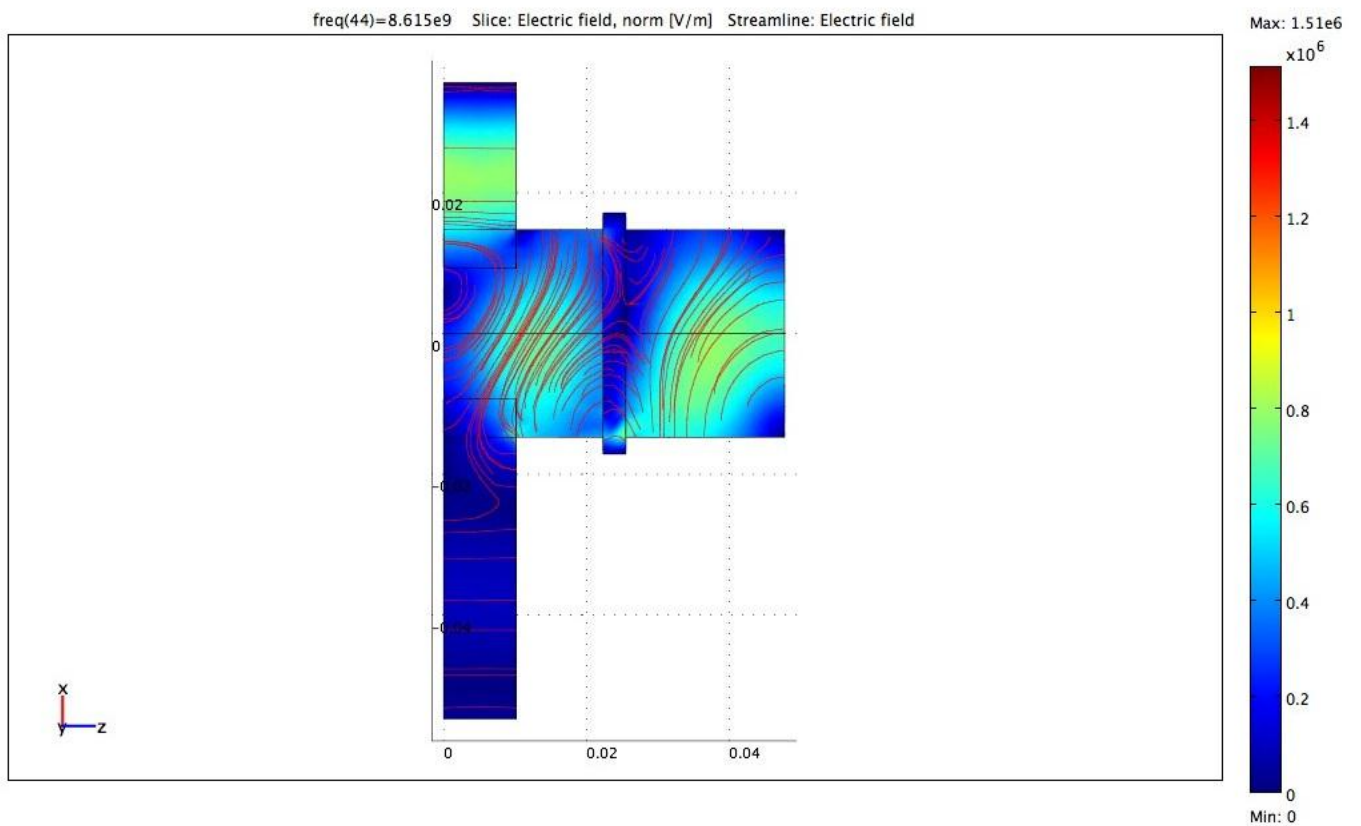


**Figure 4.21** WR90 full-height with 60% length short configuration.

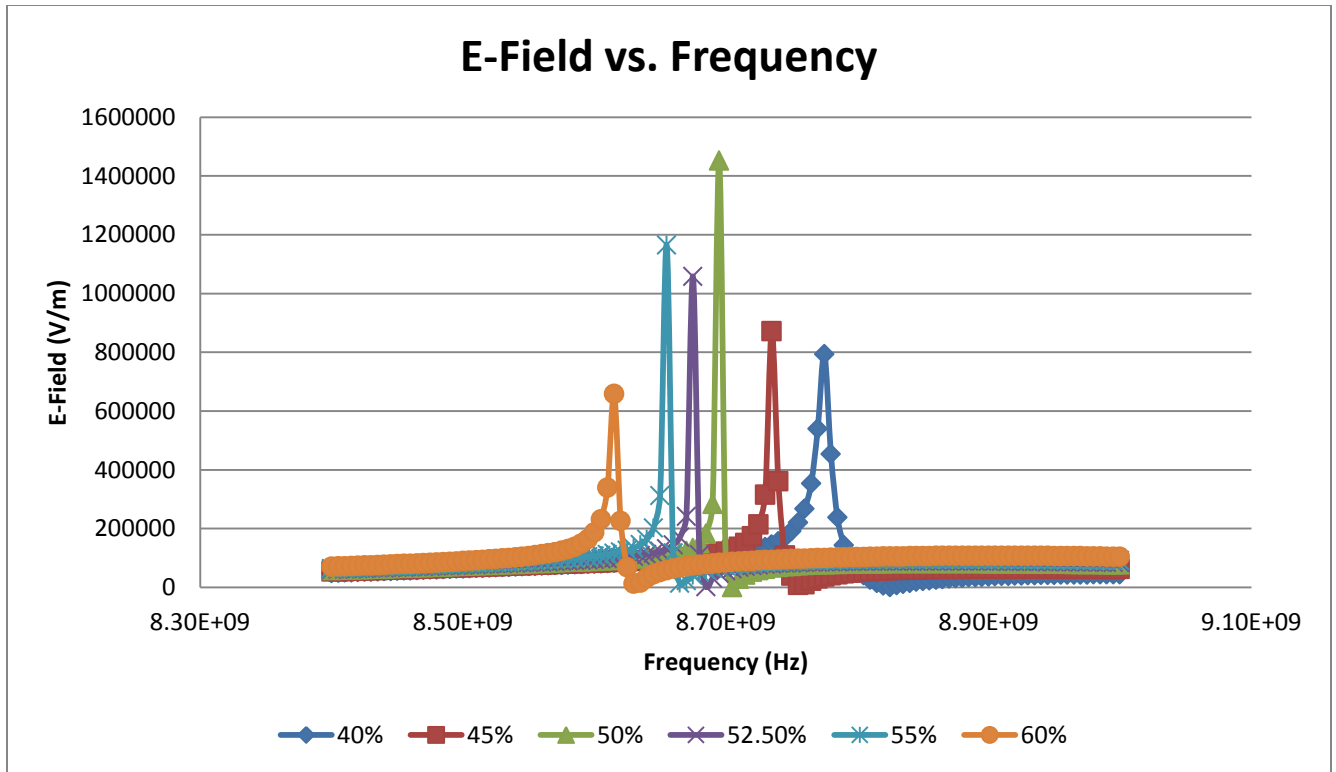


**Figure 4.22** E-Field vs. Frequency for WR90 full-height waveguide configuration with short.

Using a full-height WR90 waveguide, the model with the highest electric field intensity was the model where the short was 50% of the input waveguide. This can be seen in Figure 4.22. Despite having the highest electric field intensity, the mode shape was unstable in that it was a hybrid between the  $TM_{012}^z$  and  $TM_{011}^z$  mode shapes. Another issue was that there was a high electric field concentration in the waveguide short.

#### 4.1.4.2 WR90 Half-Height with Variable Short Length

After modeling the WR90 full-height configuration, a transition was made into using the WR90 half-height waveguides in an attempt to obtain a better  $TM_{011}^z$  mode shape. The half-height configuration was optimized in the same manner as with the full-height configuration. The short length was varied as a percentage of the length of the input waveguide. The length was varied from 40–60% and the contour result of the electric field for these models can be seen in Figures 4.23–4.28

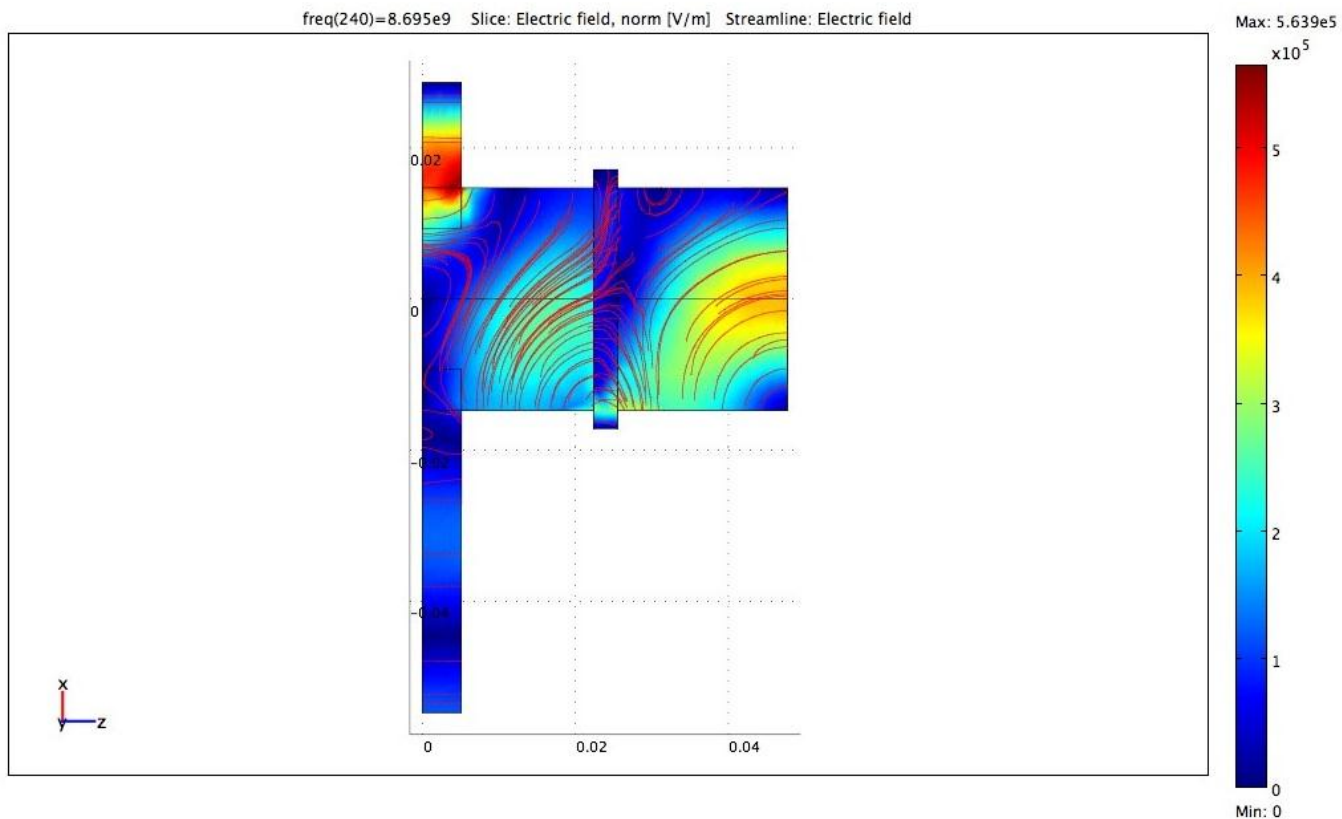


**Figure 4.23** WR90 half-height with 40% length short configuration.

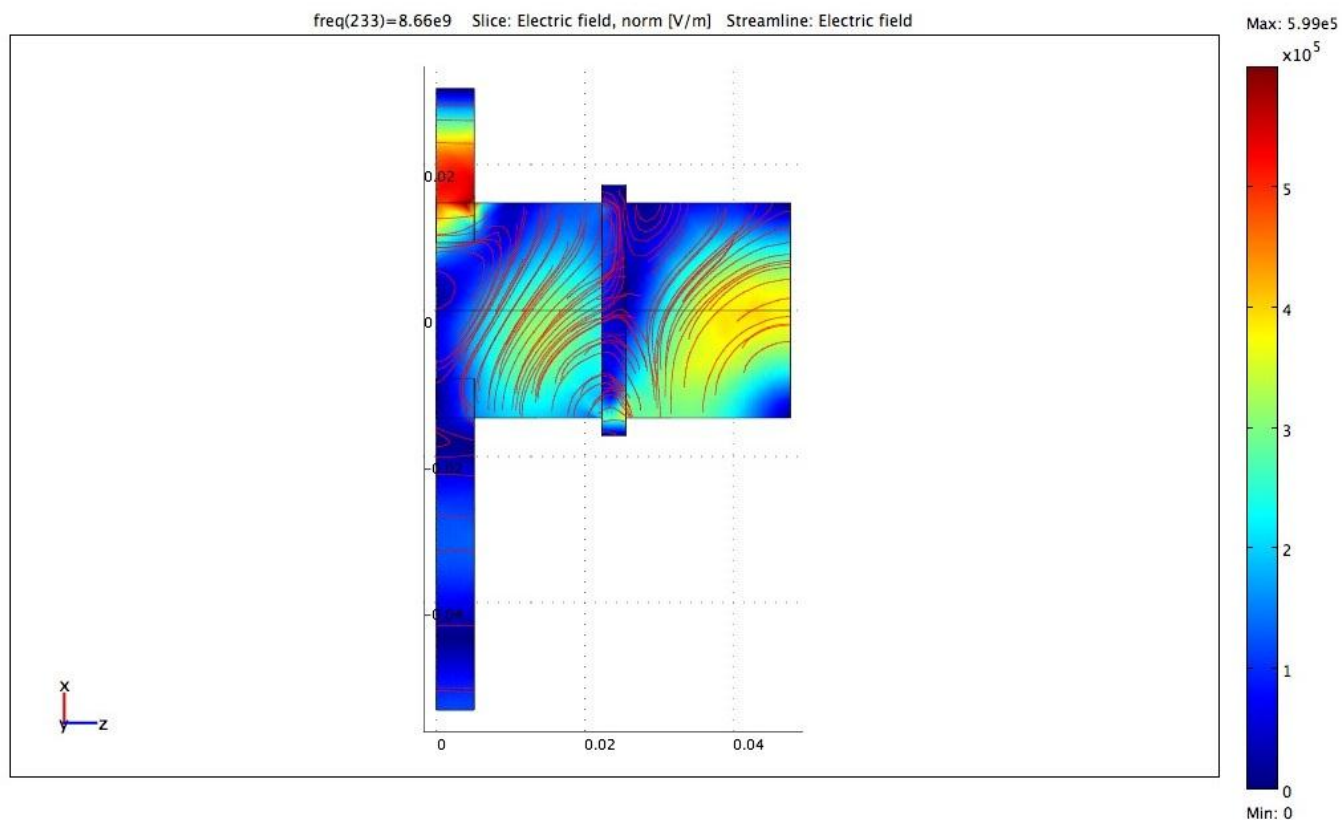


**Figure 4.24** WR90 half-height with 45% length short configuration.

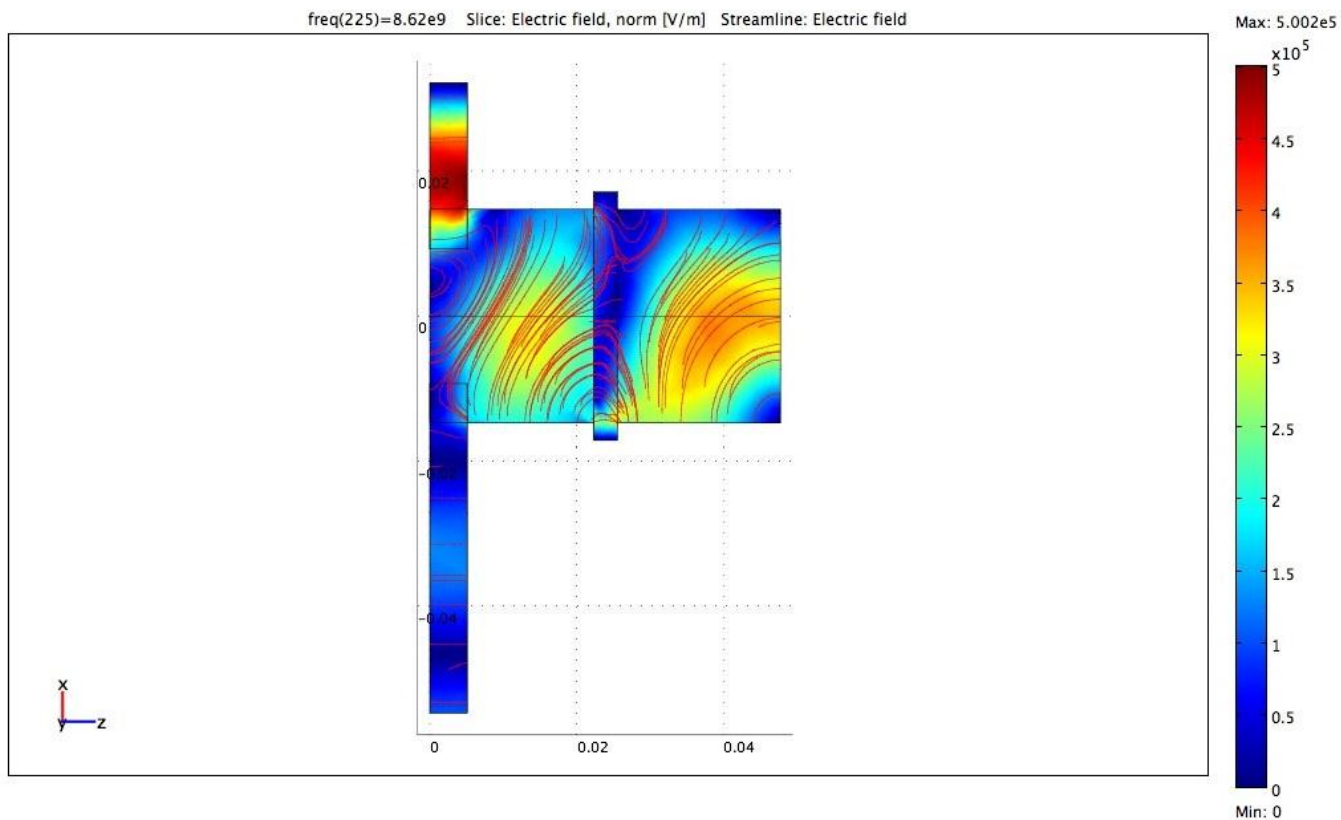


**Figure 4.25** WR90 half-height with 50% length short configuration.

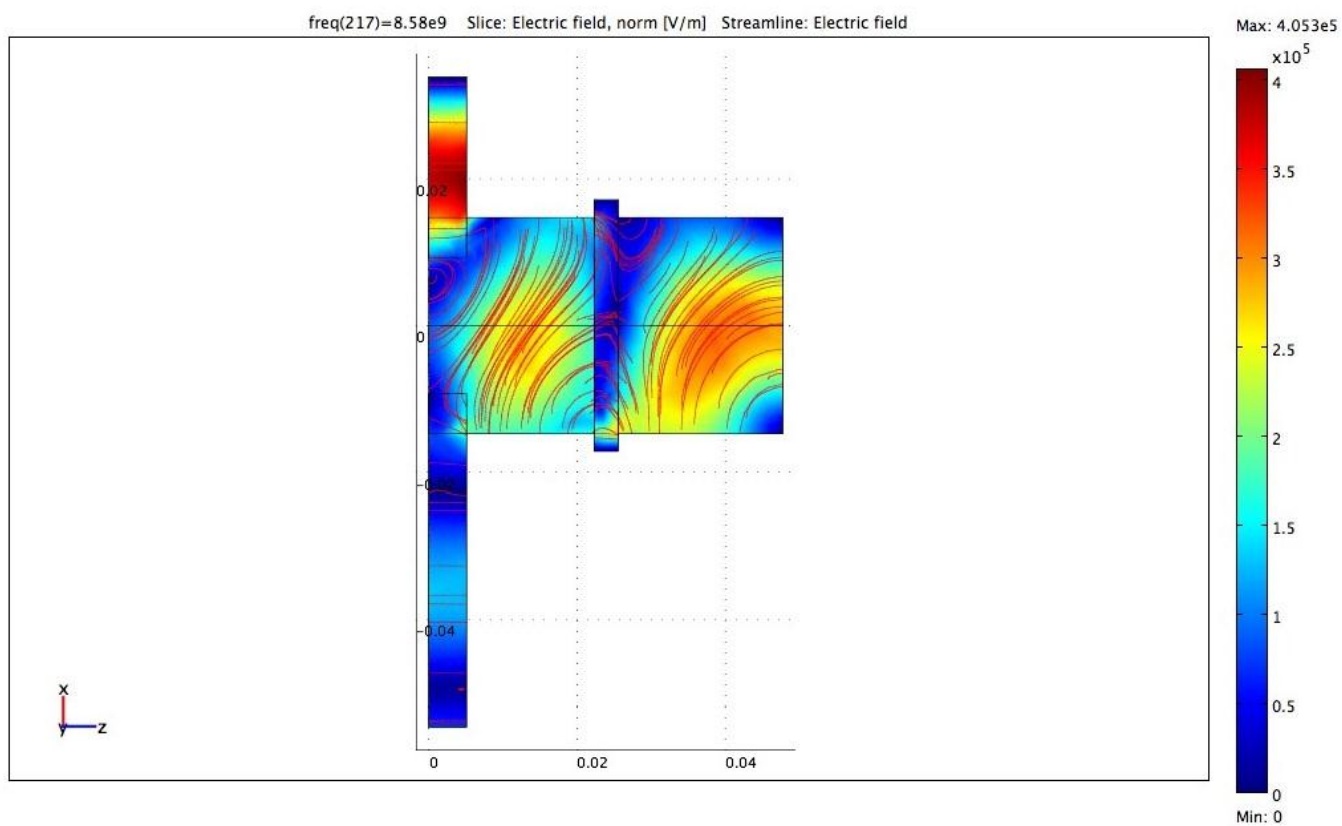


**Figure 4.27** WR90 half-height with 55% length short configuration.

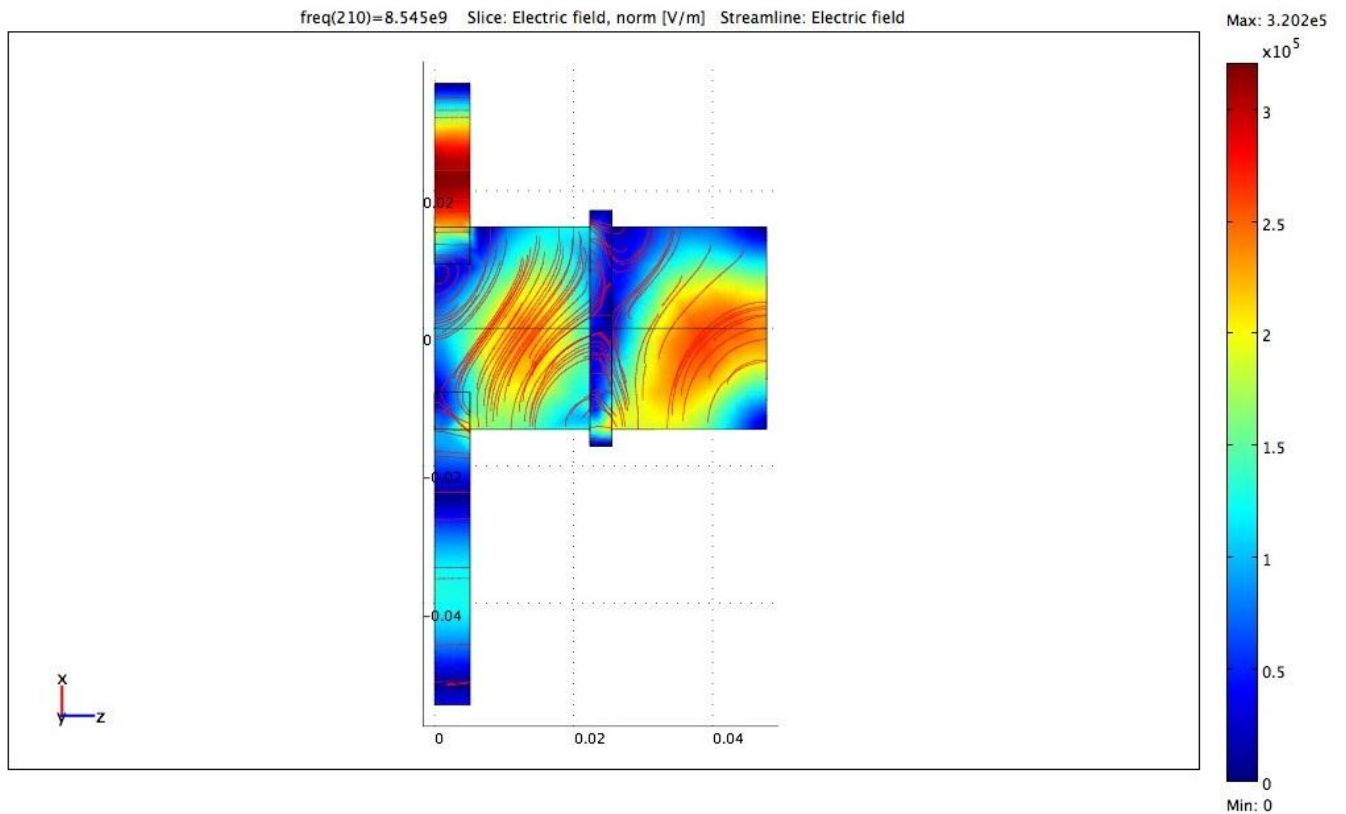


**Figure 4.28** WR90 half-height with 60% length short configuration.

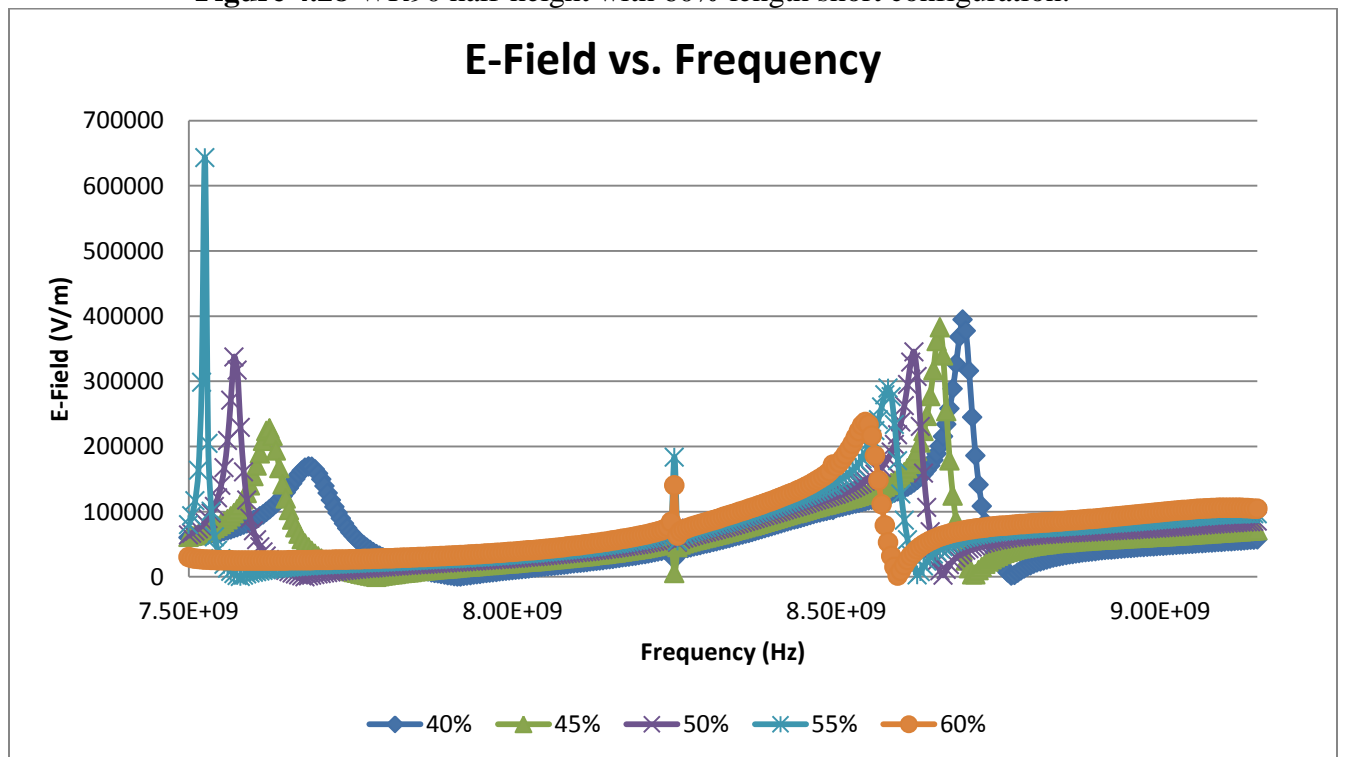


**Figure 4.29** E-Field vs. Frequency for WR90 half-height waveguide configuration with short.



The results of the half-height model have a mode shape that resembles the  $TM_{011}^z$  mode shape, but not in a symmetric and robust manner as is preferred. The electric field results in Figure 4.29 show a wider frequency range where the modes resonate, which yields the assumption that the mode shape would better maintain itself in operation as compared to the narrower peaks of the full-height simulation. However, the issue of a high electric field in the short was still a present issue.

#### 4.1.4.3 WR90 Full-Height with Variable Quartz Short Length

After modeling the WR90 half-height configuration, the concept of using a short composed of quartz was modeled. This was done with the hope of reducing the high electric field in the short. The WR90 full-height waveguide was used in this simulation. The length of the short was varied from 25–55% of the input waveguide length. Figures 4.30–4.33 contain the contour results of the electric field intensity.

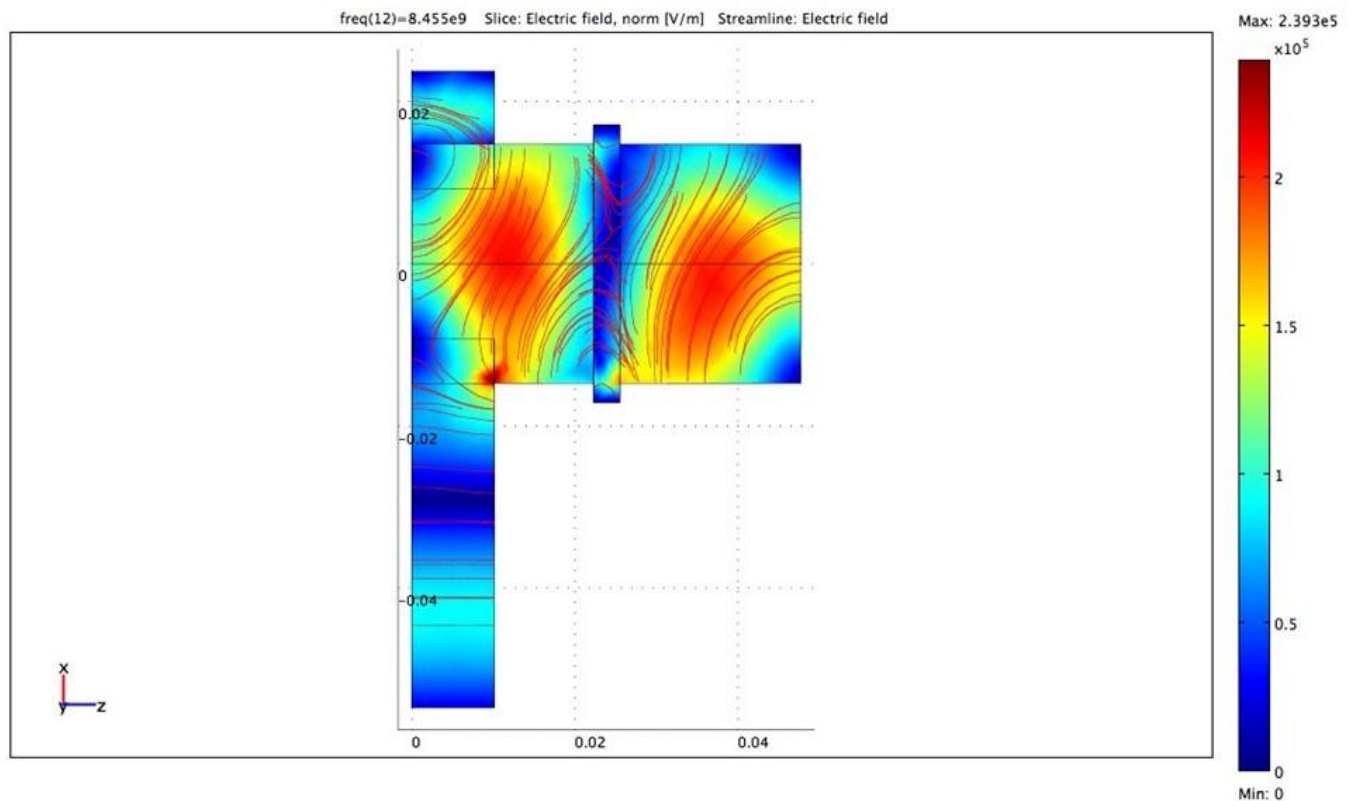


**Figure 4.30** WR90 full-height with 25% length quartz short configuration.

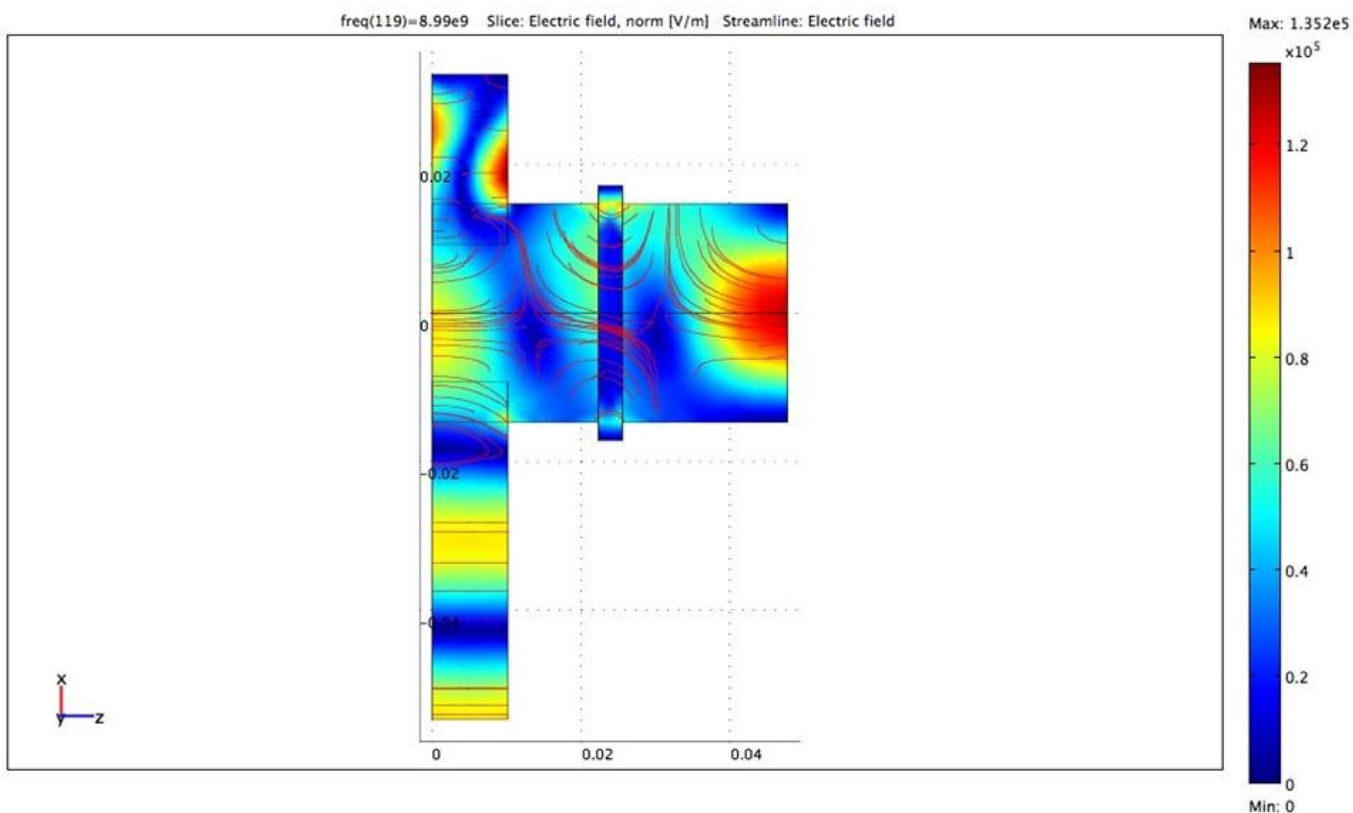


**Figure 4.31** WR90 full-height with 50% length quartz short configuration.

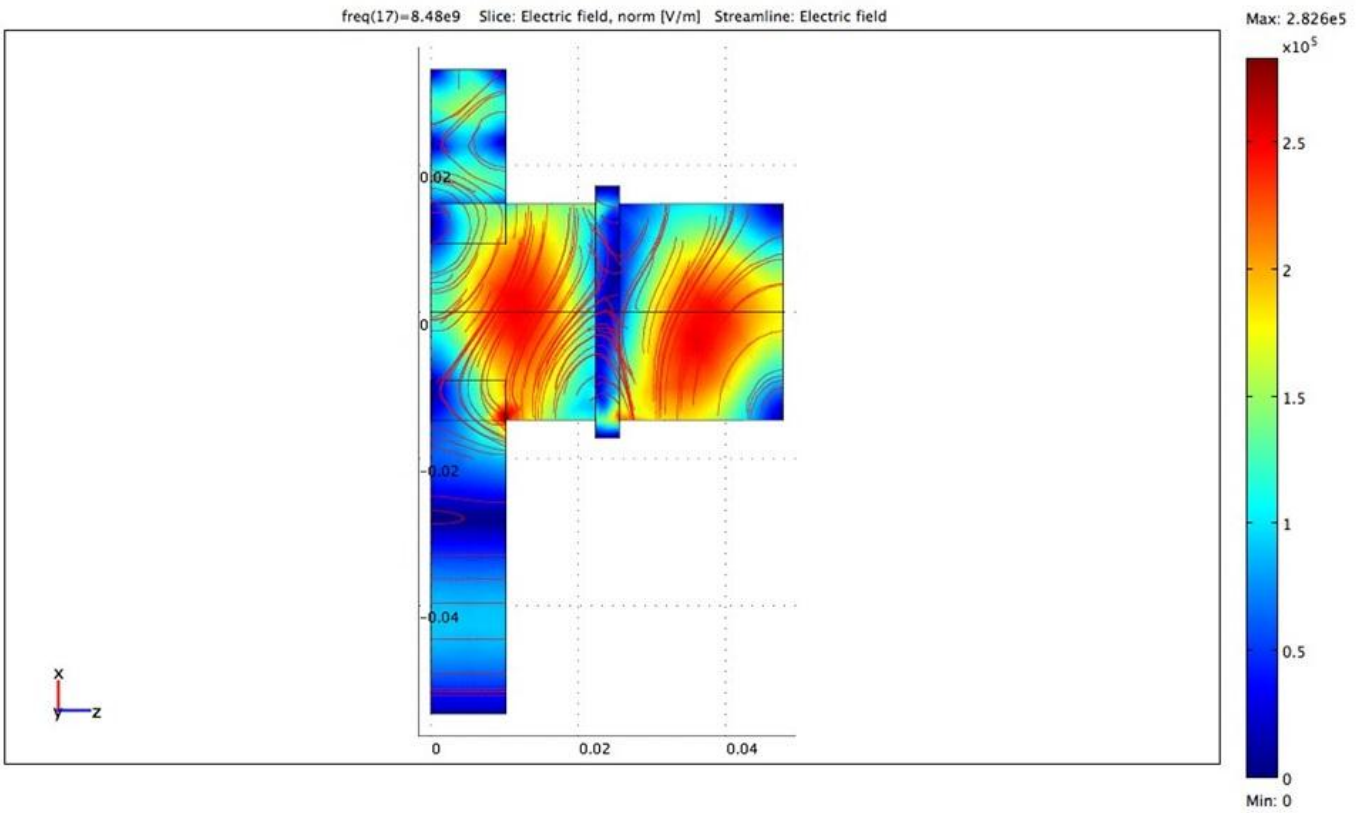


**Figure 4.32** WR90 full-height with 52.5% length quartz short configuration.

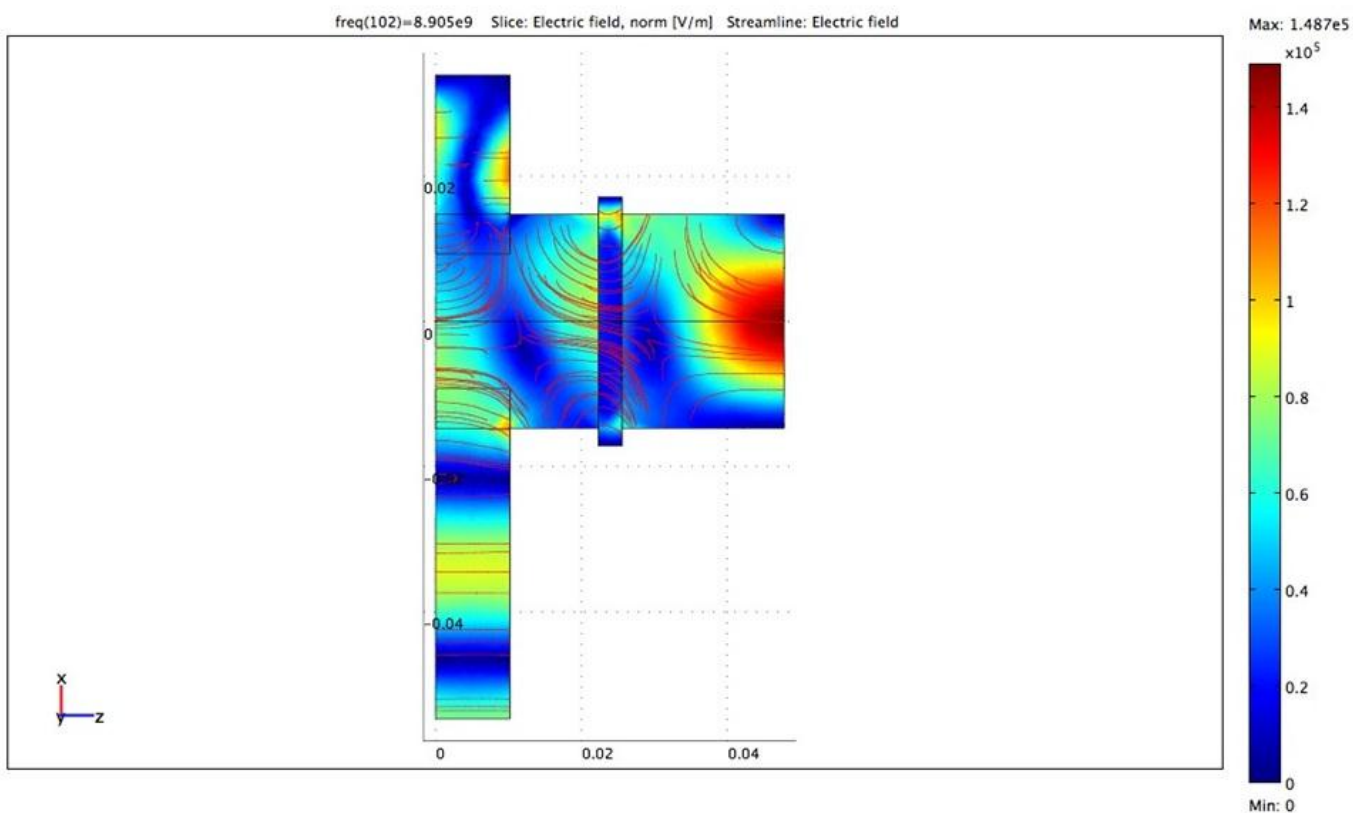


**Figure 4.33** WR90 full-height with 55% length quartz short configuration.

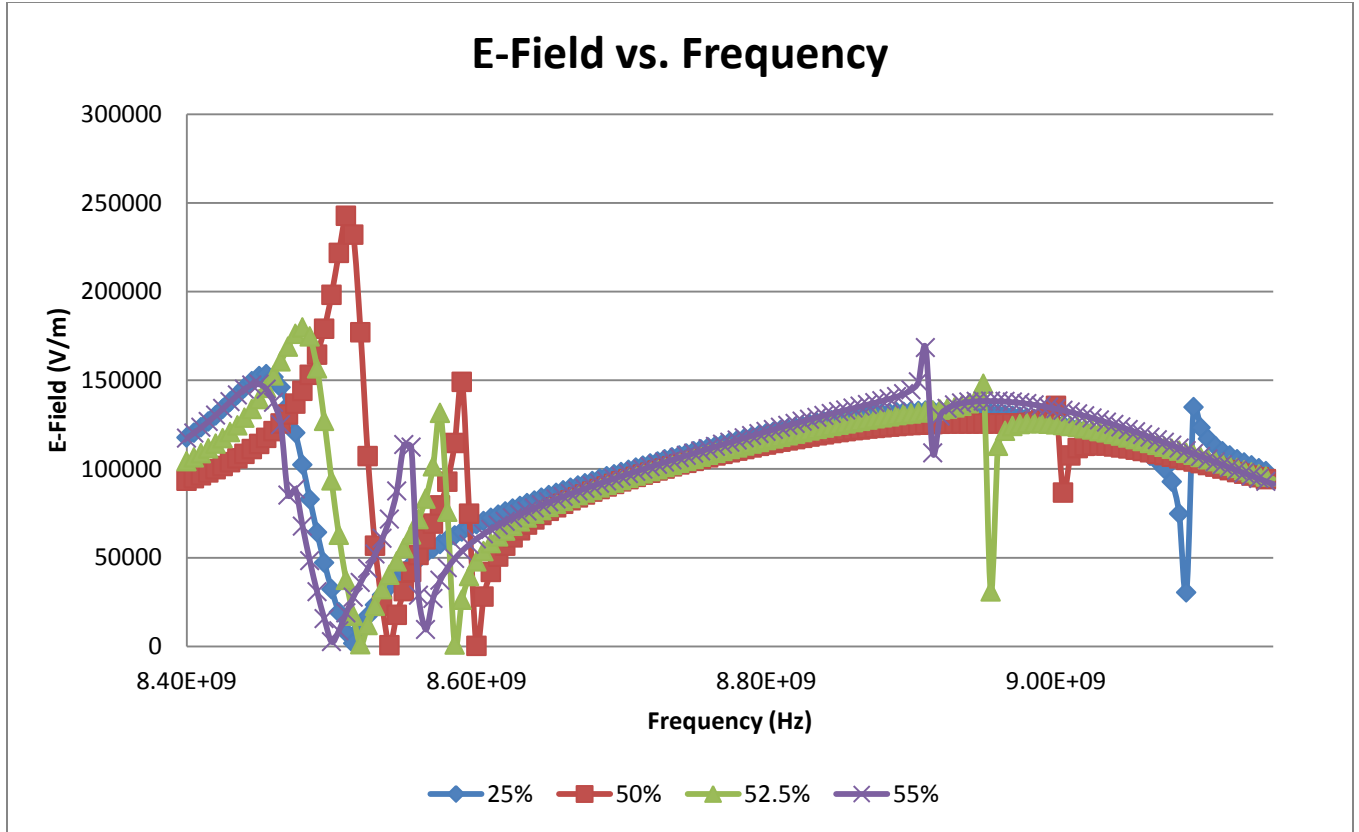


**Figure 4.34** E-Field vs. Frequency for WR90 full-height waveguide configuration with quartz short.

Using the quartz short, the electric field concentration was successfully reduced in most of the cases. In addition to this, the electric field concentration in the 50 and 55% short length scenarios had the highest electric field concentration at the entrance of the nozzle. When observing Figure 4.34, one can see that the simulation with the highest electric field concentration was the case with the quartz short length that was 50% of the input waveguide. Despite these results, the mode shape mode dominantly seen was the  $TM_{012}^z$  mode shape.

#### 4.1.4.4 Optimized Single Direct Waveguide Input with Short Configuration

In the optimum configuration, the short was modeled to be one-half a wavelength and the waveguide itself was one wavelength. The waveguide used is a WR90 half-height configuration. The width is 0.9 inches and the height is 0.2 inches. The length of the waveguide is 1.434 inches and the short length is 0.717 inches. The chamber dimensions remain the same in this model. Figure 4.35 is a contour plot of the electric field. Although the intensity is very good, an issue arises with the high concentration by the corner of the short. Several modifications were

implemented, but this core issue was not completely resolved. Figure 4.36 is a graph of E-field vs. frequency for the single waveguide with short configuration. The intensity of the electric field was approximately  $3.65 \times 10^5$  V/m at a frequency of 7.57 GHz.

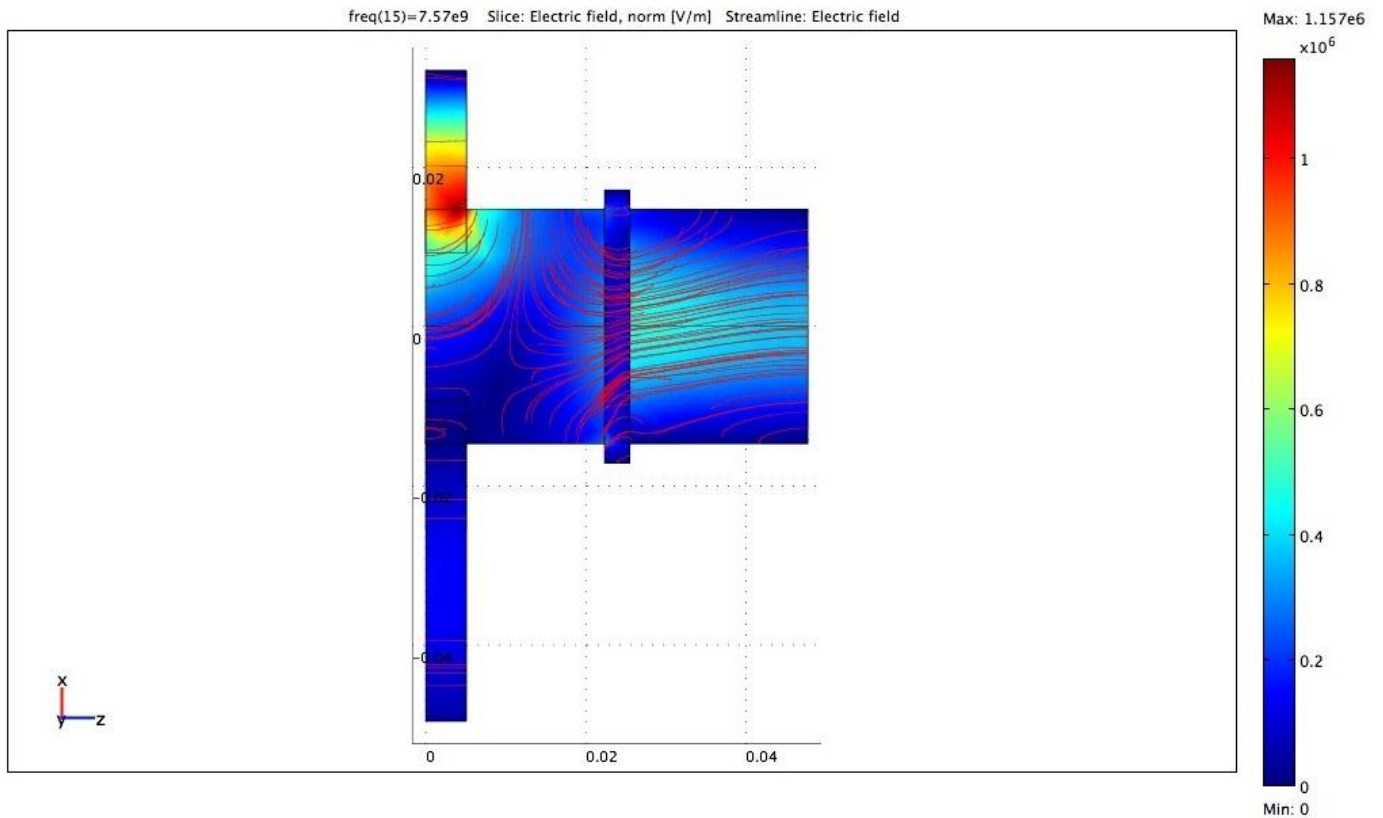


**Figure 4.35** Contour plot of the E-Field for a single waveguide with short configuration.

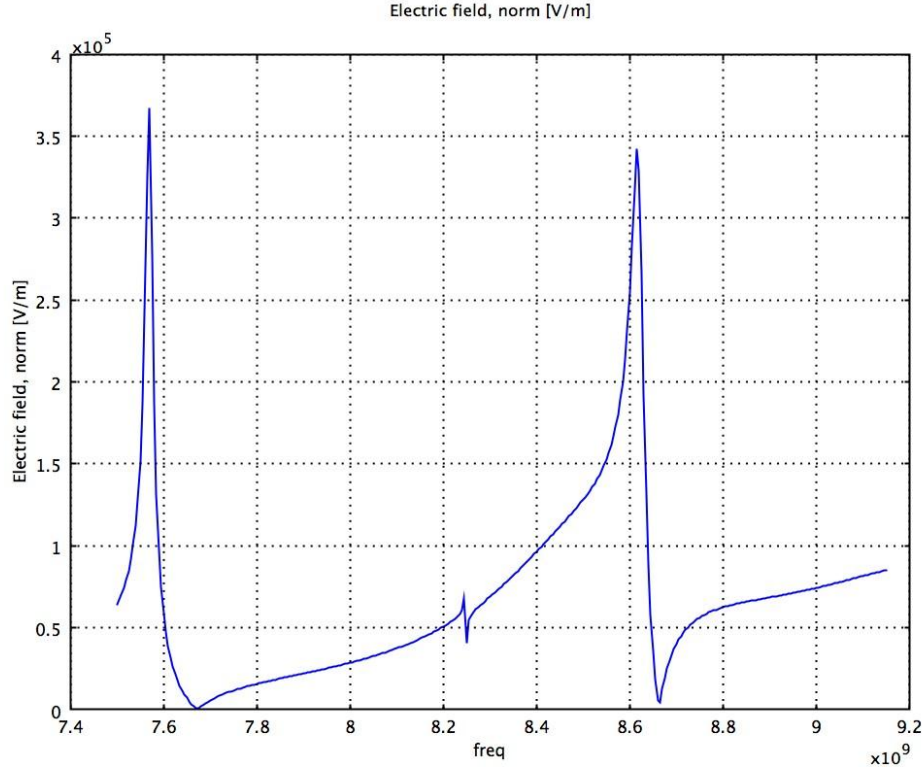


**Figure 4.36** Graph of E-Field vs. Frequency for the single waveguide with short model.

Although many of the issues of the single waveguide input configuration were resolved through the incorporation of a short, a new set of issues were present. Arcing was a large issue when modeling with a short as well as a high electric field concentration in the short that at times exceeded the concentration at the entrance to the nozzle. The  $\text{TM}_{012}^z$  mode shape was very domineering and despite multiple efforts to obtain a robust  $\text{TM}_{011}^z$  mode shape, this was never accomplished successfully. The  $\text{TM}_{011}^z$  modes obtained lacked symmetry, which would lead to instability and unreliable operation, thus, this configuration was not used.

#### 4.1.5 Waveguide to Coaxial Coupling

After modeling configurations of a coaxial port configuration and with a waveguide directly into the cavity, the two models were coalesced into one configuration in which the microwave energy entered into a waveguide and then, by coupling a coaxial antenna to the waveguide, the energy could be introduced into the cavity, thus utilizing the strengths of both configurations. The coaxial models gave very symmetric  $\text{TM}_{011}^z$  mode shapes and high electric fields were obtained using waveguides. A short was also used when coupling the waveguide and antenna as

to help optimize the configuration. In addition to this, a few studies were conducted to further optimize the configuration aside from using a short. Optimization models were produced for the waveguide, antenna, and aperture. Both WR112 and WR90 waveguides with varying lengths were modeled. Models with varying antenna depth within the chamber and end shape were generated. Apertures with different heights and widths were also examined.

#### 4.1.5.1 WR90 vs. WR112

The first aspect of the waveguide to coax coupling configuration investigated was the type of waveguide that would give the best result. The WR112 full and half-height waveguides were compared to the WR90 full and half-height waveguides to see which would yield the best results. Figure 4.37 contains the result of the waveguide comparison for the initial configuration.

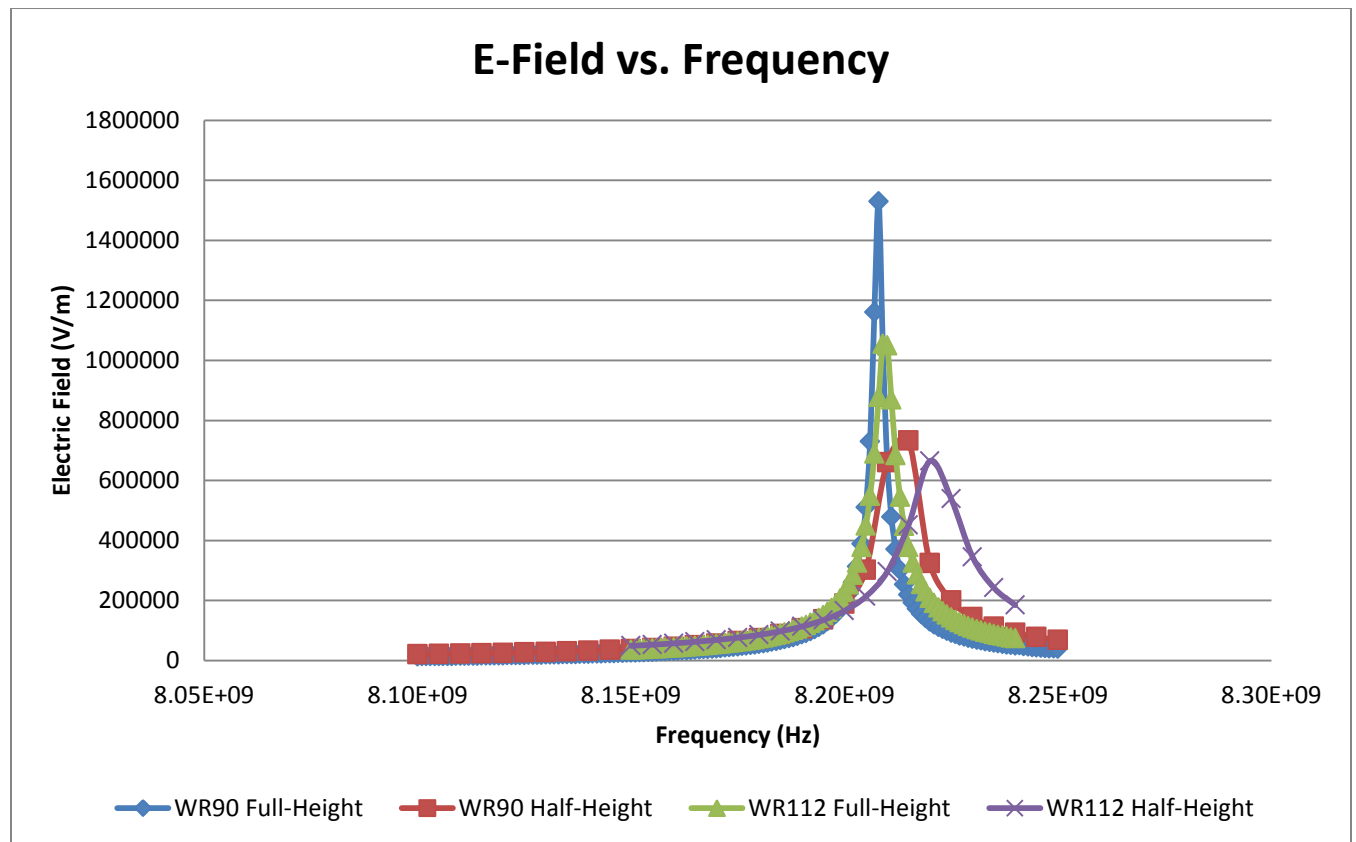


**Figure 4.37** Graph of E-Field vs. Frequency for the single waveguide with short model.

Initial modeling prior to optimizing the overall design gave results that strongly showed that higher electric fields were obtained with the full-height waveguides and, between the two full-height waveguides, the WR90 full-height configuration yielded the best results. In an attempt to



validate or disprove this result, models were made to optimize the geometry of the configuration, which eventually lead to disproving the idea that the WR90 waveguide gave the best result.

#### 4.1.5.2 Variable Antenna Depth

After completing the waveguide, optimization tests were done to further increase the electric field results. The first of these was to model variable antenna lengths using both the WR90 and WR112 waveguide configurations. The results for the WR90 and WR112 full-height configurations can be seen in Figures 4.38 and 4.39, respectively.

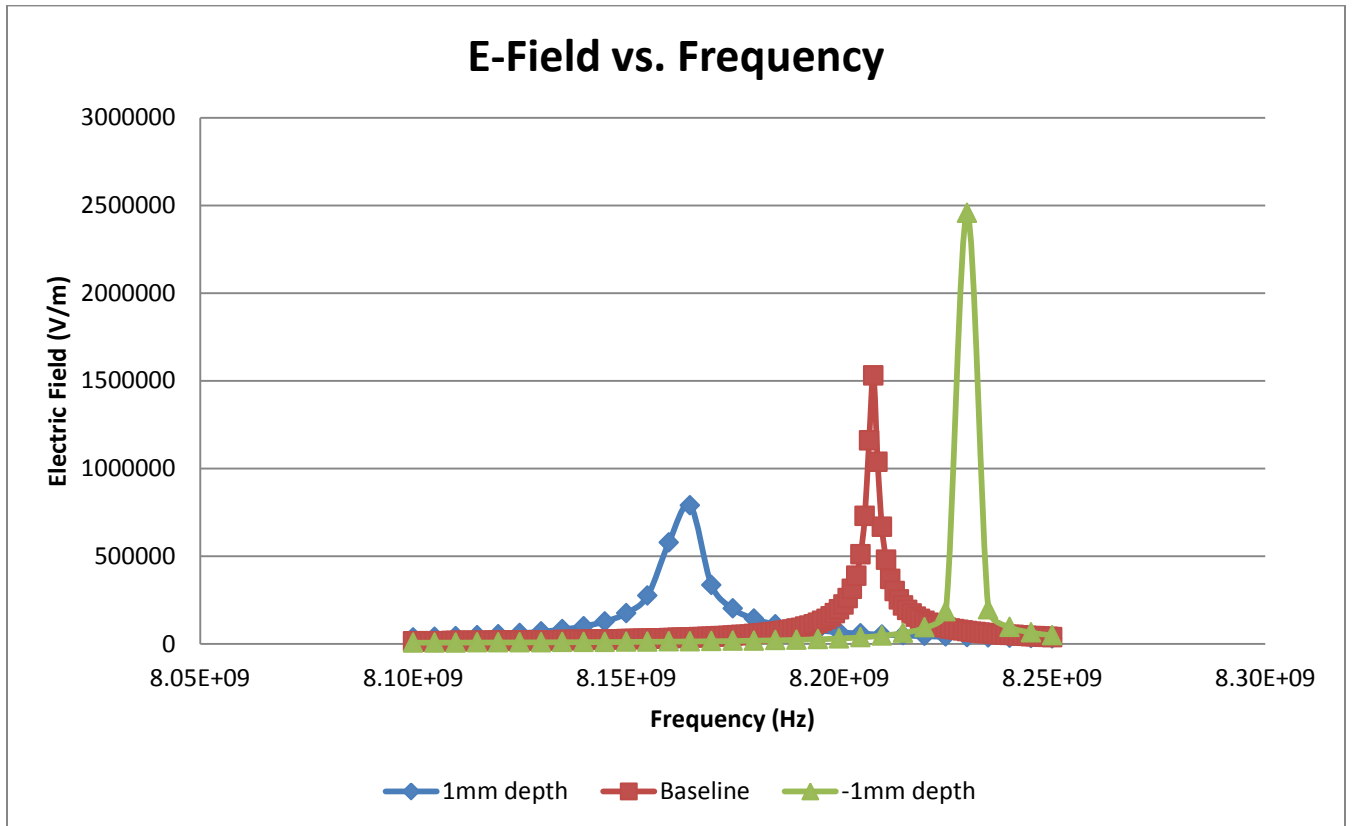


**Figure 4.38** Antenna depth study of E-Field vs. Frequency for WR90 full-height waveguide.

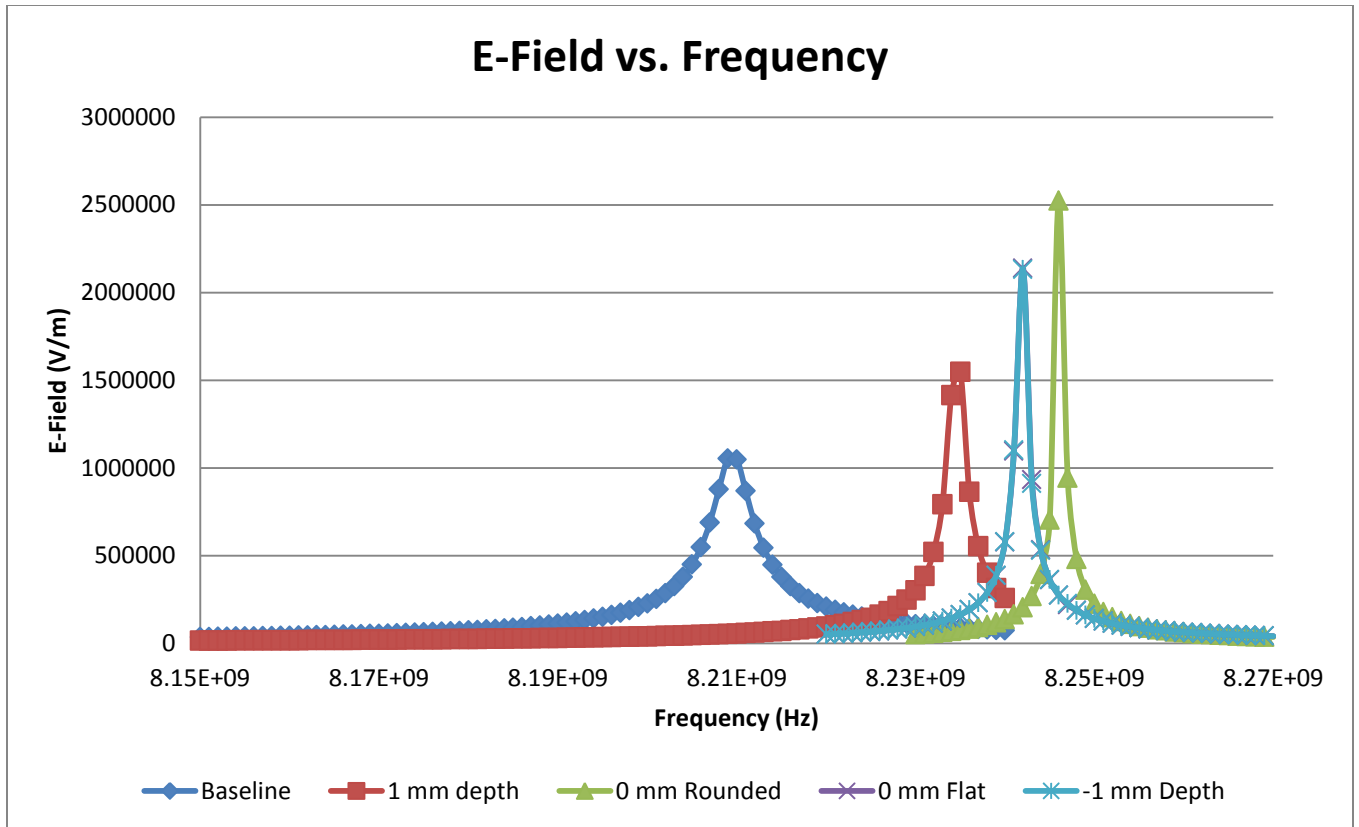


**Figure 4.39** Antenna depth study of E-Field vs. Frequency for WR112 full-height waveguide.

The results of the antenna depth study show that, upon optimizing the MET by varying the antenna length, higher electric fields were obtained with the WR112 waveguide. The baseline configuration also had a more robust resonance for the WR112 case.

#### 4.1.5.3 Electric Field Interaction with Plasma

One of the final studies conducted was a study to observe how the electric field would act in the presence of a plasma. This was accomplished by modeling a sphere in the chamber in the area where the plasma would be expected to form. The geometry for this can be seen in Figure 4.40. This sphere was given an arbitrary conductivity and the results can be seen in Figure 4.41.

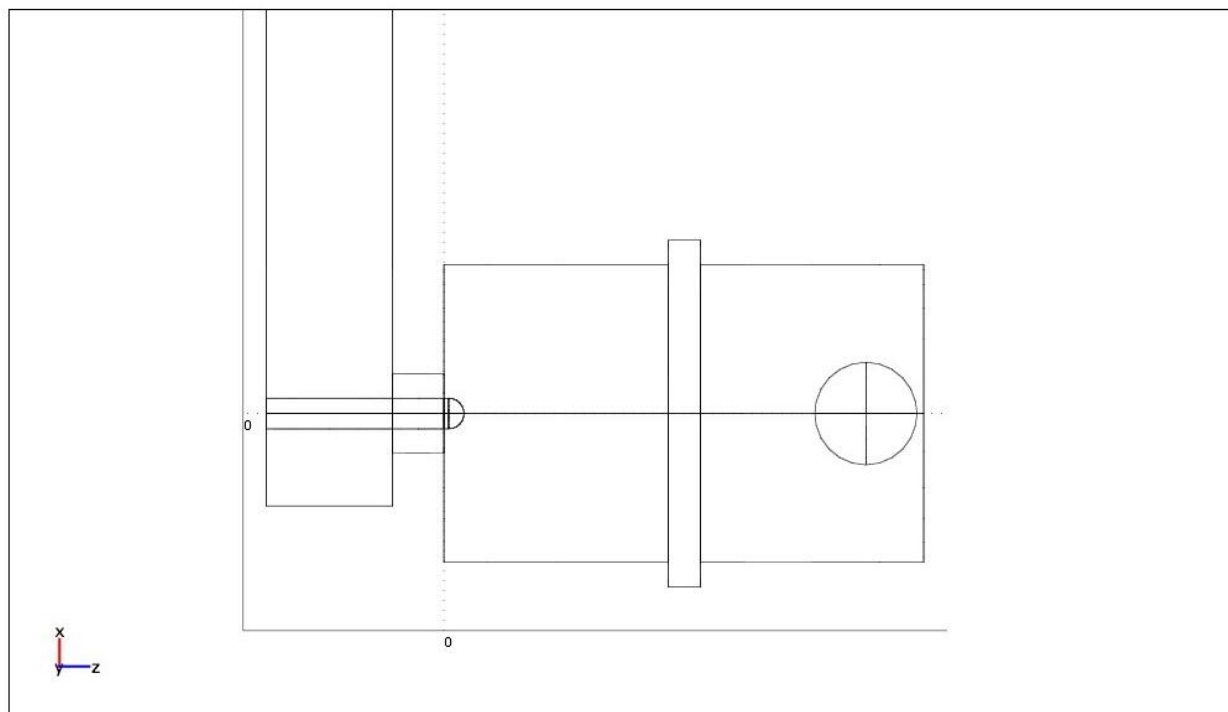


**Figure 4.40** Geometric setup of conducting sphere in MET cavity.

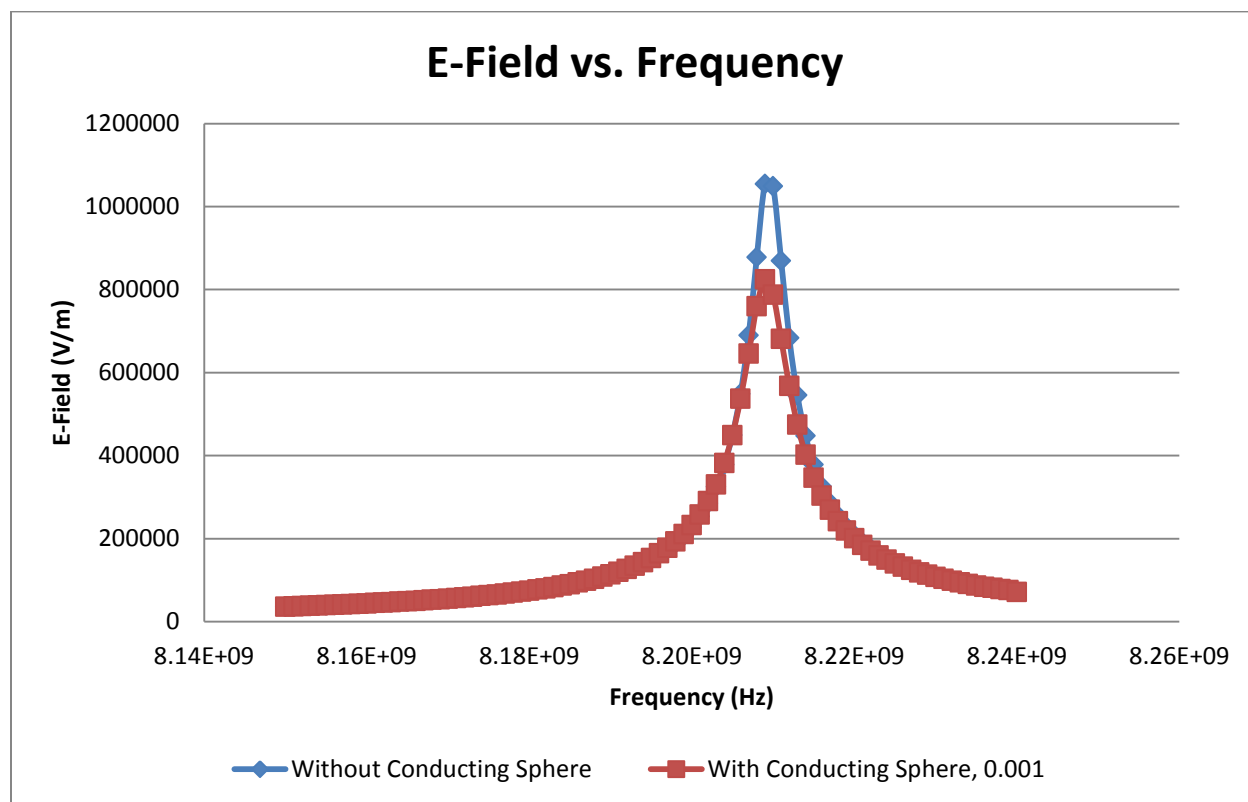


**Figure 4.41** E-field results in the presence of a conducting sphere for a WR112 configuration.

When inserting a conducting sphere in the cavity, one can see the drop in the electric field as much of the energy is absorbed into the sphere. Though this result is obviously not exact, it gives some indication of the behavioral change that the electric field will have in response to a plasma being present. It should also be noted that as the conductivity of the sphere increases, the electric field intensity decreases.

#### **4.1.5.4 Final MET Design**

The final design used was a waveguide with a short of one-quarter wavelength connected to an aperture and antenna. A WR112 waveguide was connected to a short with one quarter the length and this was connected to a coaxial configuration. The width of the waveguide is 1.122 inches and the height is 0.497 inches. The waveguide length is 0.357 inches to the center of the aperture and 0.1785 inches outward from the center on the other side. The height of the aperture is 0.2 inches with a radius of 0.155 inches. The antenna has a height of 0.7748 inches and a radius of 0.0598 inches. The tip of the antenna is rounded as well. The dimensions of the cavity remain the same. This final design had produced the best results and the most stable  $TM_{011}^z$  mode shape. Figure 4.42 shows a contour plot of electric field and the shows a pretty solid  $TM_{011}^z$  mode shape with a high e-field concentration. Figure 4.43 is a graph of the e-field vs. frequency for this configuration. The max electric field intensity is  $1.06 \times 10^6$  V/m at a frequency of 8.209 GHz.

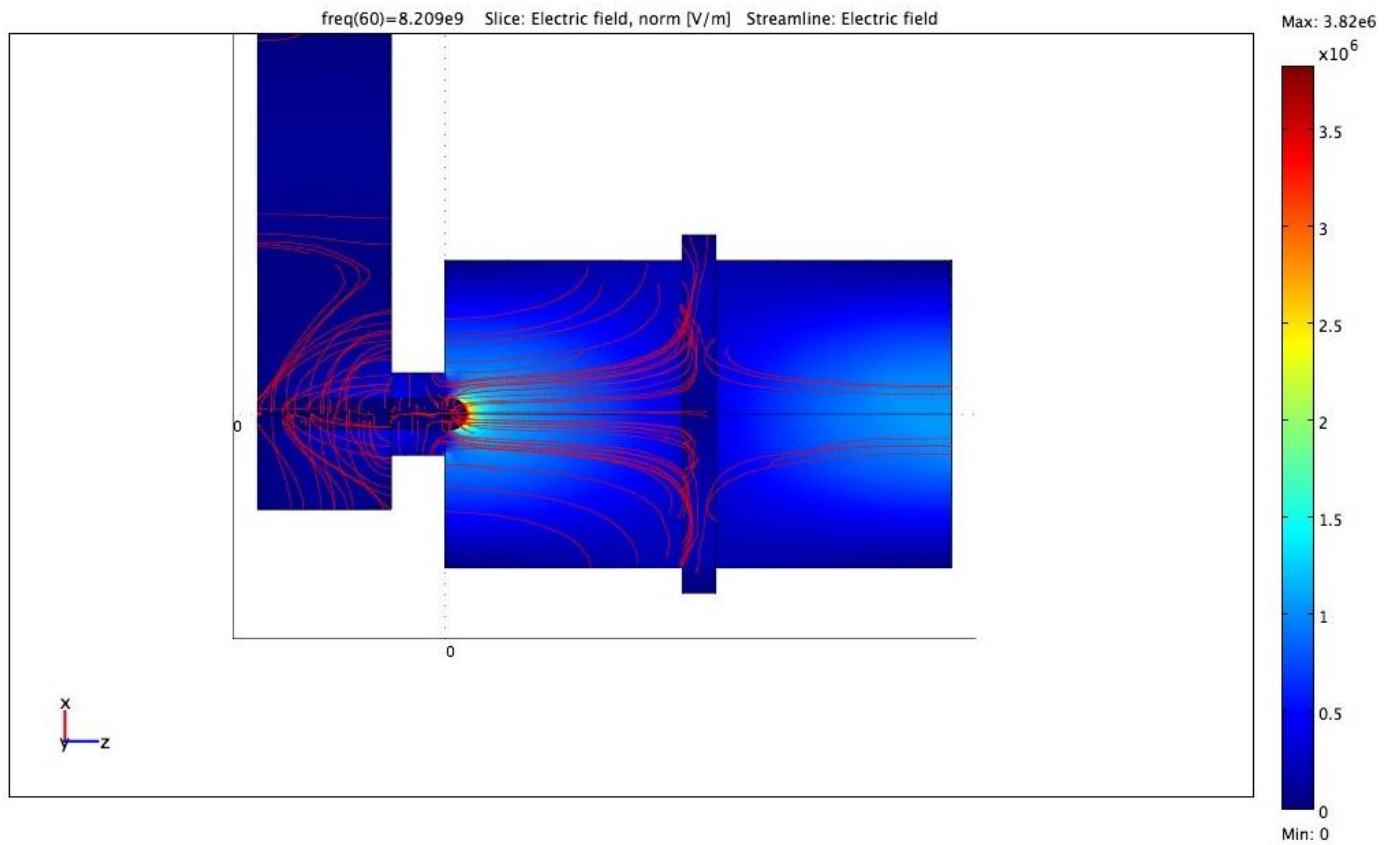


**Figure 4.42** Contour plot of the E-Field for a single waveguide with short with coaxial coupling.

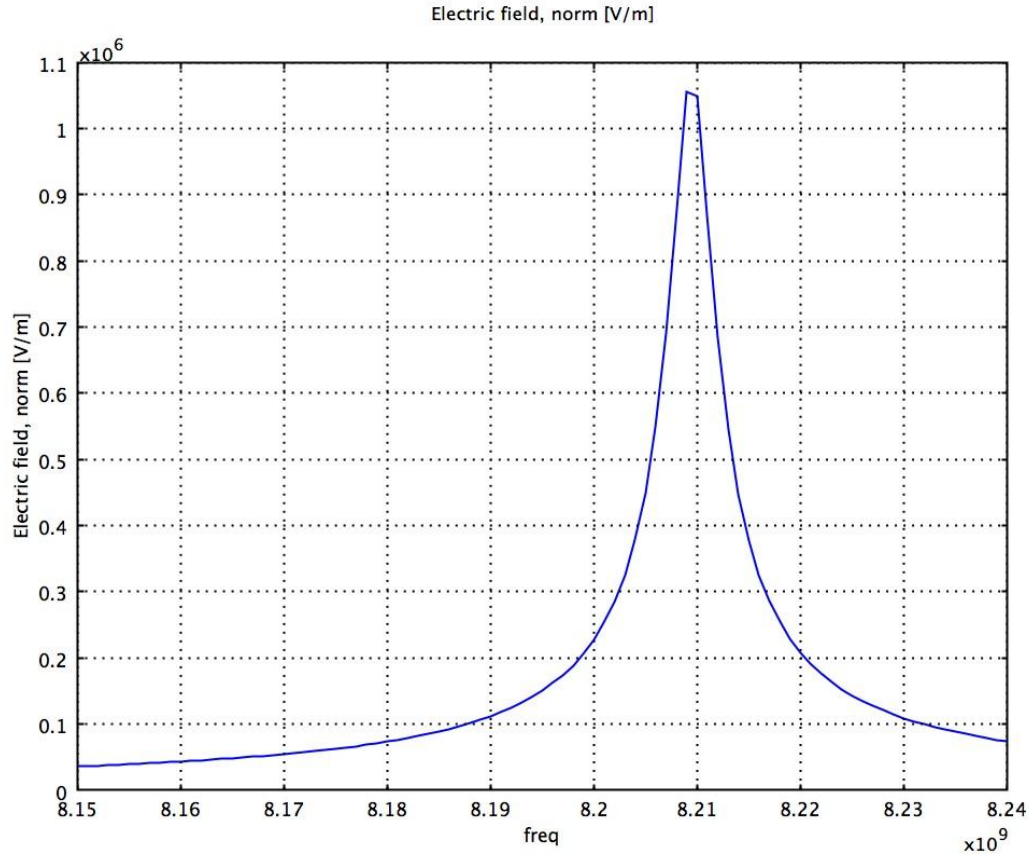


**Figure 4.43** Graph of E-Field vs. Frequency for the single waveguide with coaxing coupling.

## 4.2 Fluid Mechanics Modeling

The results of the fluid mechanics modeling are presented in this section. The main objective for modeling the fluid dynamics was to model the propellant injection system with the intention of better understanding the characteristics of the swirled flow within the MET. The overall goal was to model the propellant injection system using viscous compressible flow assumptions. The main issue with this was that COMSOL Multiphysics lacked a module that was capable of modeling compressible flow. The newest version of COMSOL Multiphysics (4.0a) has a Computational Fluid Dynamics (CFD) module that is capable of modeling compressible fluids below Mach 0.3, but in order to do anything higher than this, one must input their own expressions manually as will be seen in the discussion of the PDE module.

### 4.2.1 Viscous Incompressible Fluid Flow

Using the Incompressible Navier–Stokes Module, a three dimensional model was created of the swirled fuel injection within the chamber. Only the portion of the chamber above the

separation plate was modeled. In order to create the module for viscous compressible flow, the propellant injection system was first modeled using the incompressible Navier–Stokes module COMSOL Multiphysics. This helped to provide a basic idea of the flow characteristics. The velocity streamlines for the 3D viscous incompressible fluid flow of the propellant injection system can be seen in Figure 4.44. Figures 4.45 and 4.46 have the plots for pressure and velocity versus distance, respectively.

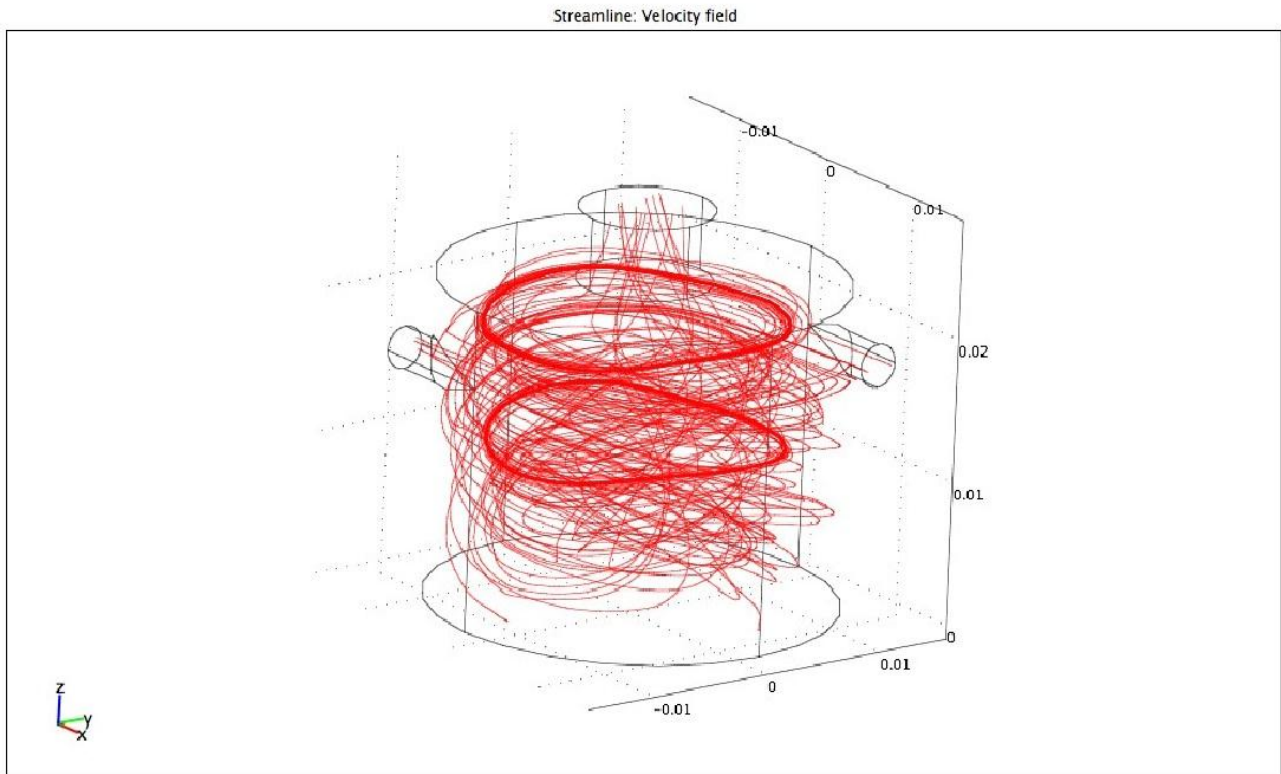


**Figure 4.44** 3-D viscous incompressible flow COMSOL Multiphysics result of the propellant injection.

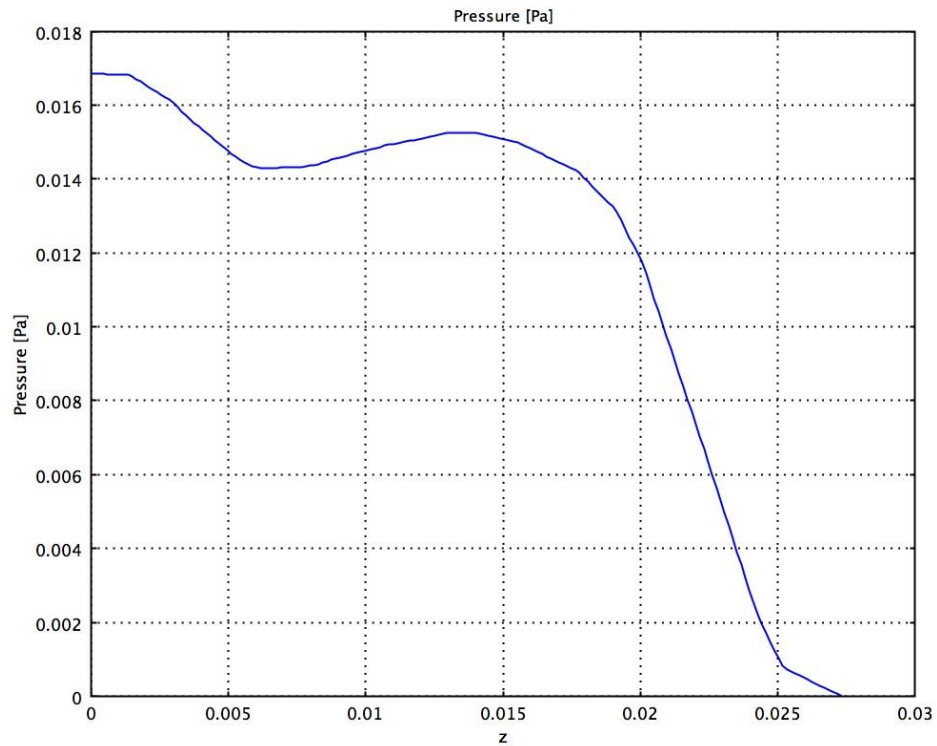


**Figure 4.45** Graph of pressure vs. distance for the viscous incompressible flow solution.

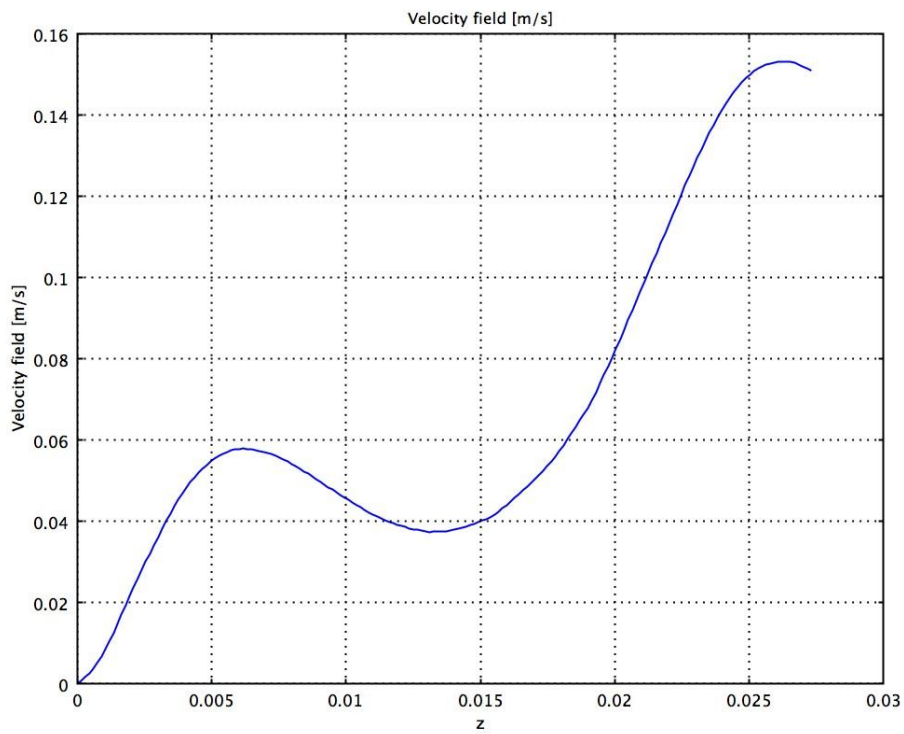


**Figure 4.46** Graph of velocity vs. distance for the viscous incompressible flow solution.



### 4.2.2 Viscous Weakly Compressible Flow

After completing the initial viscous incompressible flow modeling, the fluid flow was then modeled using the computation fluid dynamics (CFD) module, which supports weakly compressible flows. Weakly compressible flows are characterized as flows with a Mach number below 0.3. This flow is not truly compressible because when the Mach number is below 0.3, the density is relatively constant. The underlying reason for using the CFD module was to compare the results obtained from using the Reynolds averaged Navier–Stokes (RANS) smoothing method to the Galerkin least-squares (GLS) method used in the incompressible Navier–Stokes module. The 3D velocity streamline result of this model can be observed in Figure 4.47. A plot pressure vs. distance can be seen in Figure 4.48 and one of velocity vs. distance can be seen in Figure 4.49.

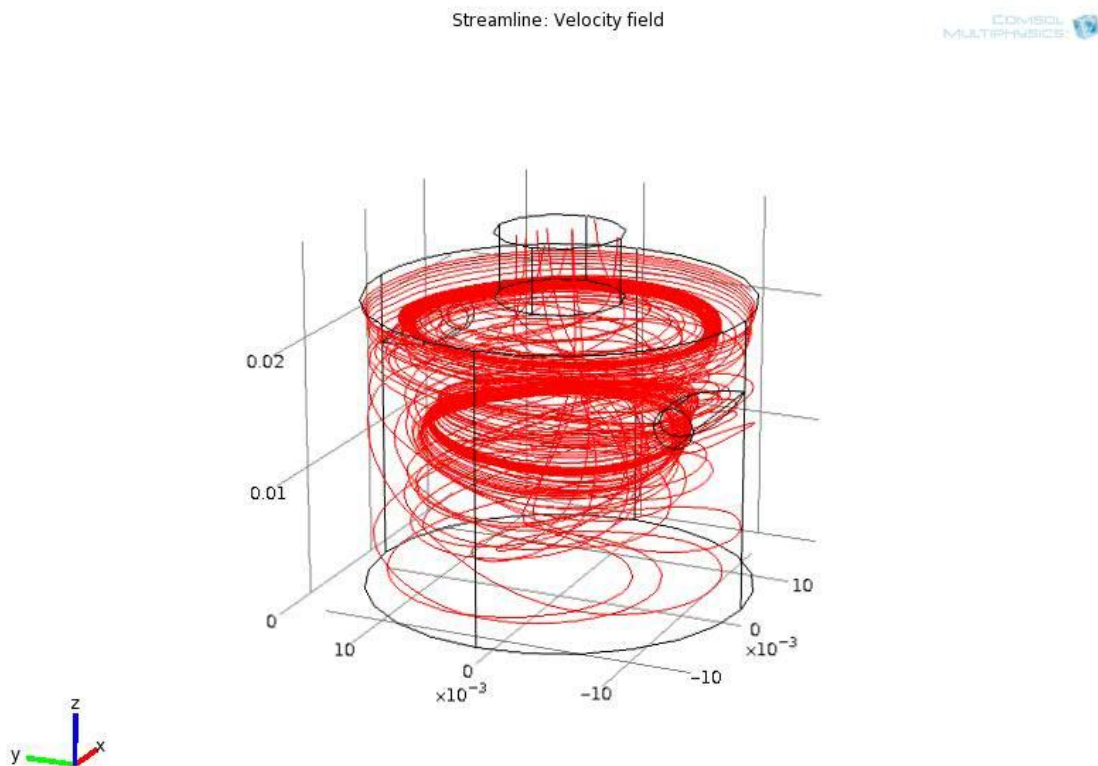


**Figure 4.47** 3-D CFD velocity streamline result.

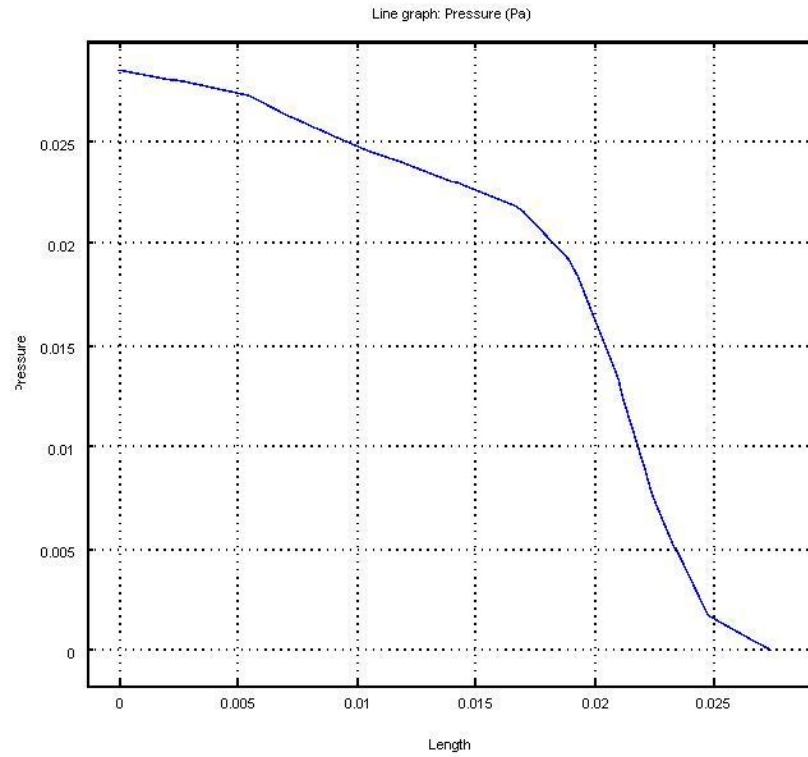


**Figure 4.48** Graph of pressure vs. distance for the COMSOL Multiphysics CFD solution.

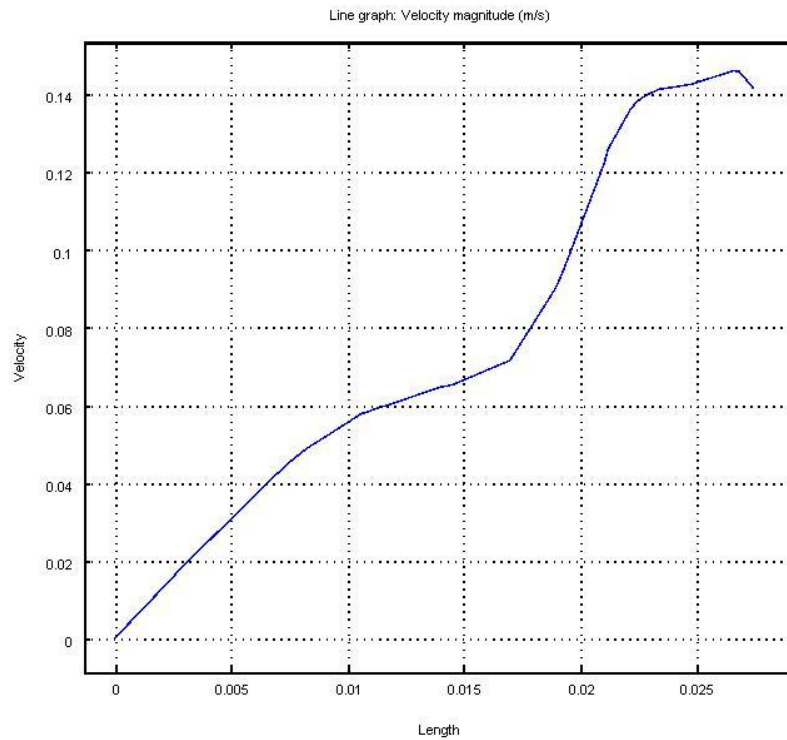


**Figure 4.49** Graph of velocity vs. distance for the COMSOL Multiphysics CFD solution.

#### 4.2.2.1 Incompressible vs. Weakly Compressible Flow

After completing the weakly compressible flow modeling, the results were compared to that of the incompressible flow. Figure 4.50 is a plot comparing the velocity results of the incompressible Navier–Stokes to that of the computational fluid dynamics module.

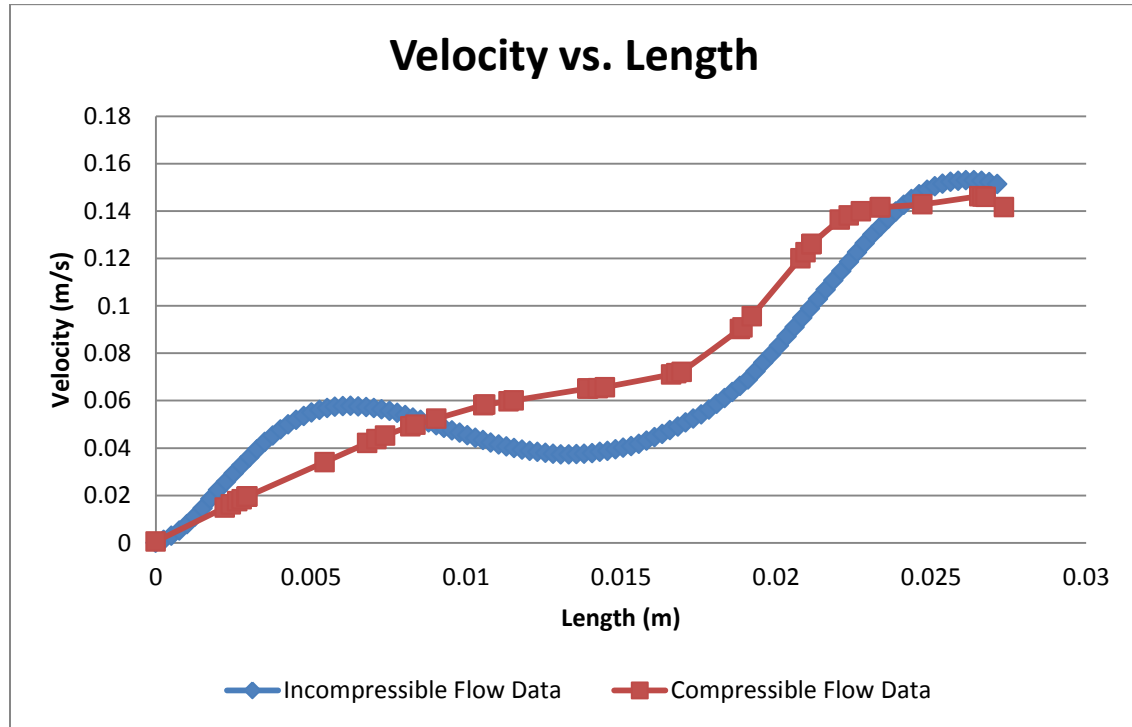


**Figure 4.50** Velocity comparison between incompressible and weakly compressible modules.

The results of the comparison between the two modules show that the smoothing methods used have a variable damping effect on the velocity. The Reynolds averaged Navier–Stokes (RANS) smoothing method of the weakly compressible flow constrains the velocity more than the Galerkin least-squares (GLS) method, but the overall results are of the same order. This information became critical later when smoothing was implemented into the PDE module.

#### 4.2.3 2D Viscous Compressible Flow

After completing the weakly compressible flow model, efforts were shifted toward creating a compressible flow model. The goal was to develop a compressible flow module that could handle Mach numbers above 0.3. Due to the complexity of building the module itself, the model was first developed in 2 dimensions. The fluid entered in a cylinder and was choked at the outlet by a converging nozzle. The governing equations for viscous compressible flow were derived

and integrated into the partial differential equation (PDE) module. Figure 4.51 contains the velocity streamline result for the 2D viscous compressible. A graph of pressure vs. distance can be observed in Figure 4.52 and a graph of velocity vs. distance can be observed in Figure 4.53.

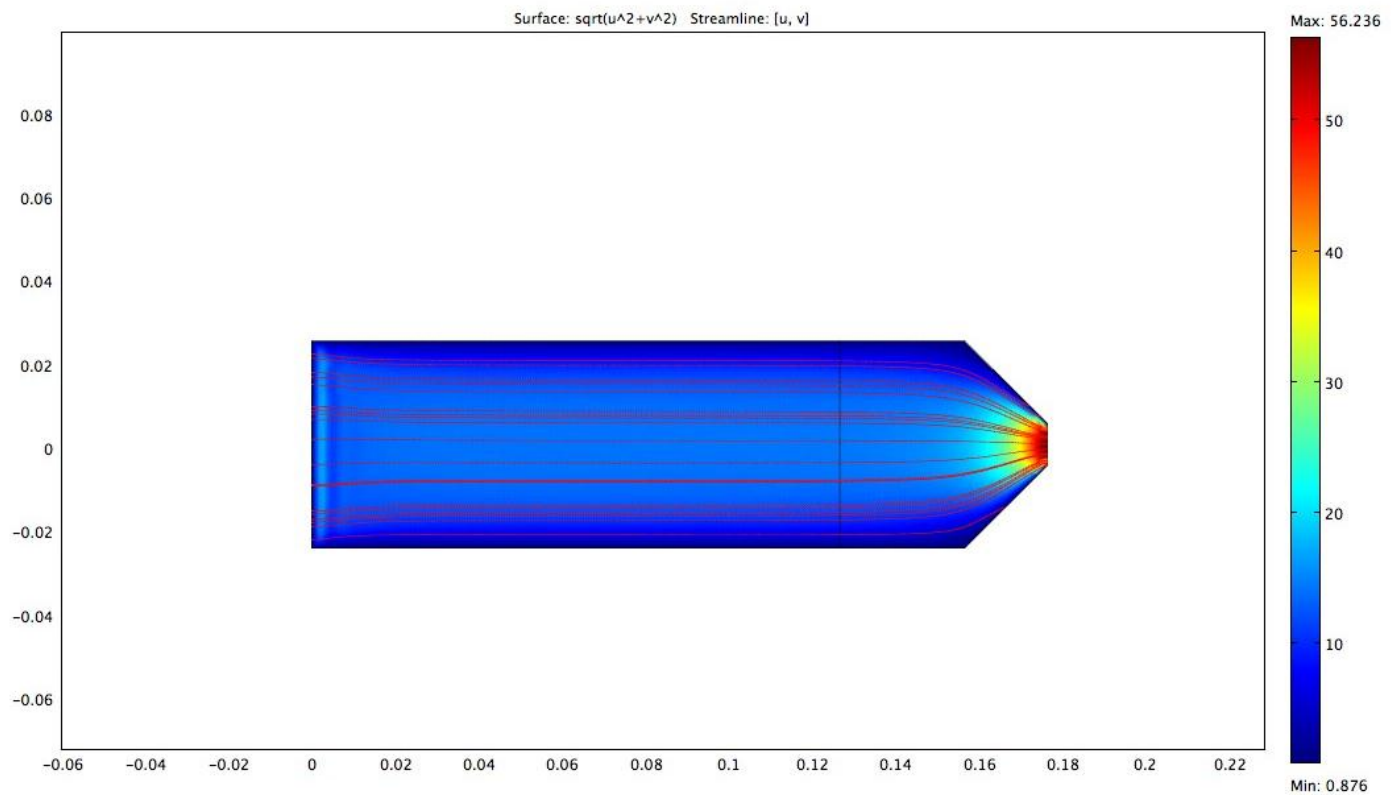


**Figure 4.51** 2-D viscous compressible flow model.

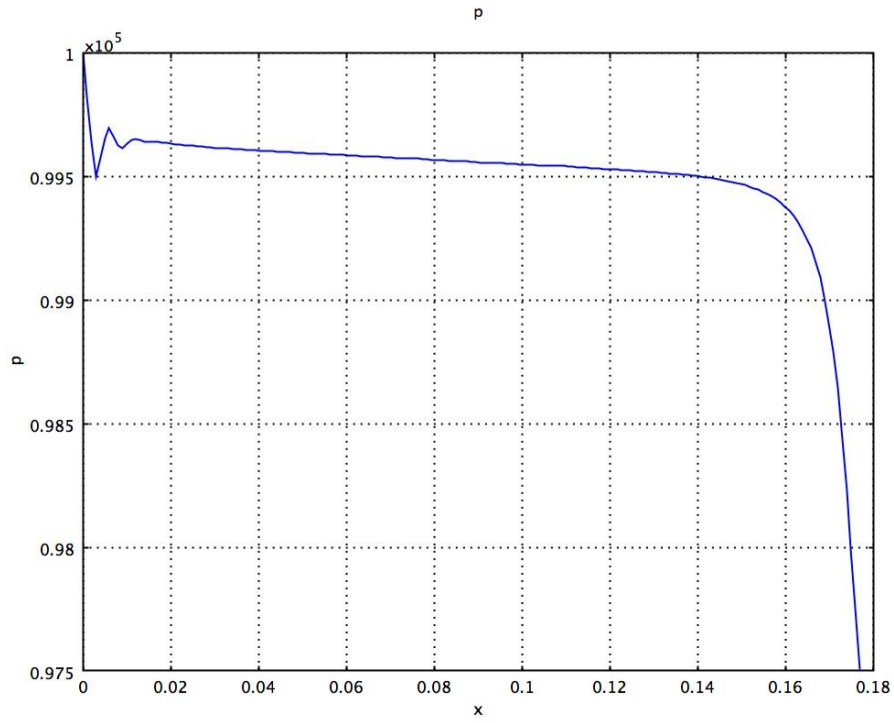


**Figure 4.52** Graph of pressure vs. distance for the 2-D viscous compressible flow solution.

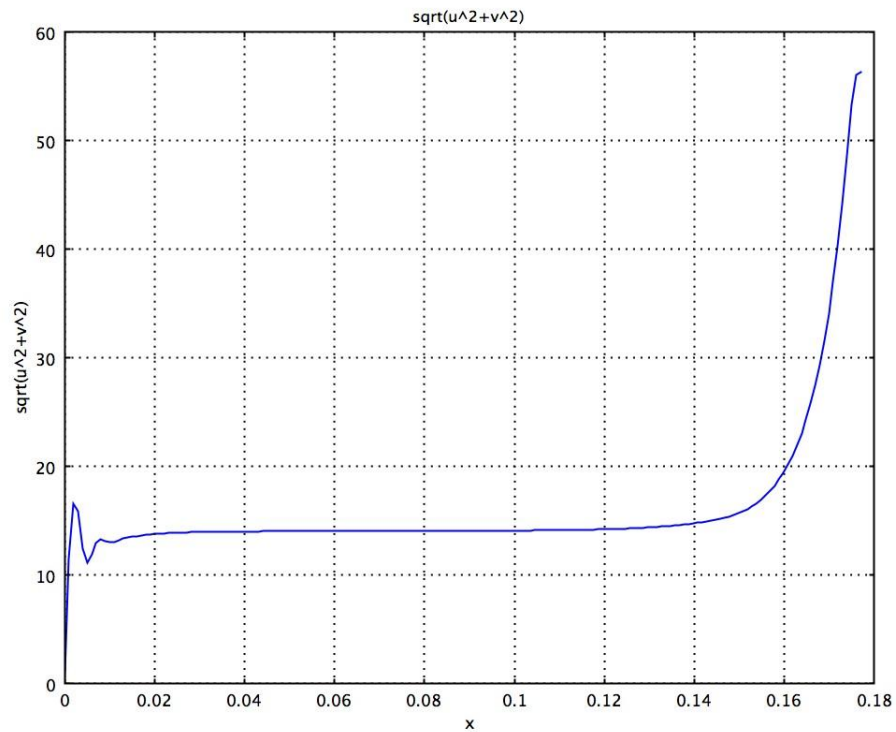


**Figure 4.53** Graph of velocity vs. distance for the 2-D viscous compressible flow solution.

#### 4.2.4 3D Viscous Compressible Flow

Once the 2D model was developed, the simulation was expanded to 3 dimensions. A 3D model can be observed in Figure 4.54. When developing the 3-dimensional models, instabilities began to arise and efforts were shifted toward resolving these issues. RANS smoothing was implemented into the 3D model in an attempt to resolve this and this COMSOL Multiphysics result can be observed in Figure 4.55. A comparison of the velocity and pressure before and after smoothing can be observed in Figures 4.56 and 4.57.

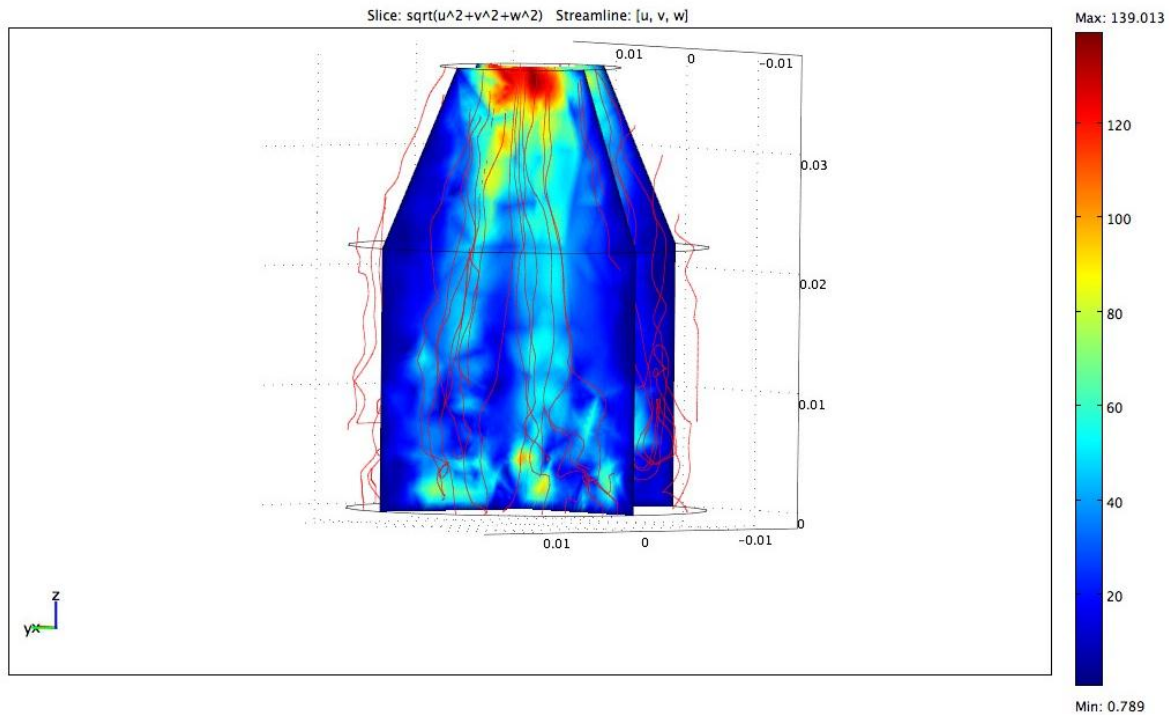


**Figure 4.54** 3-D viscous compressible flow model without RANS smoothing.

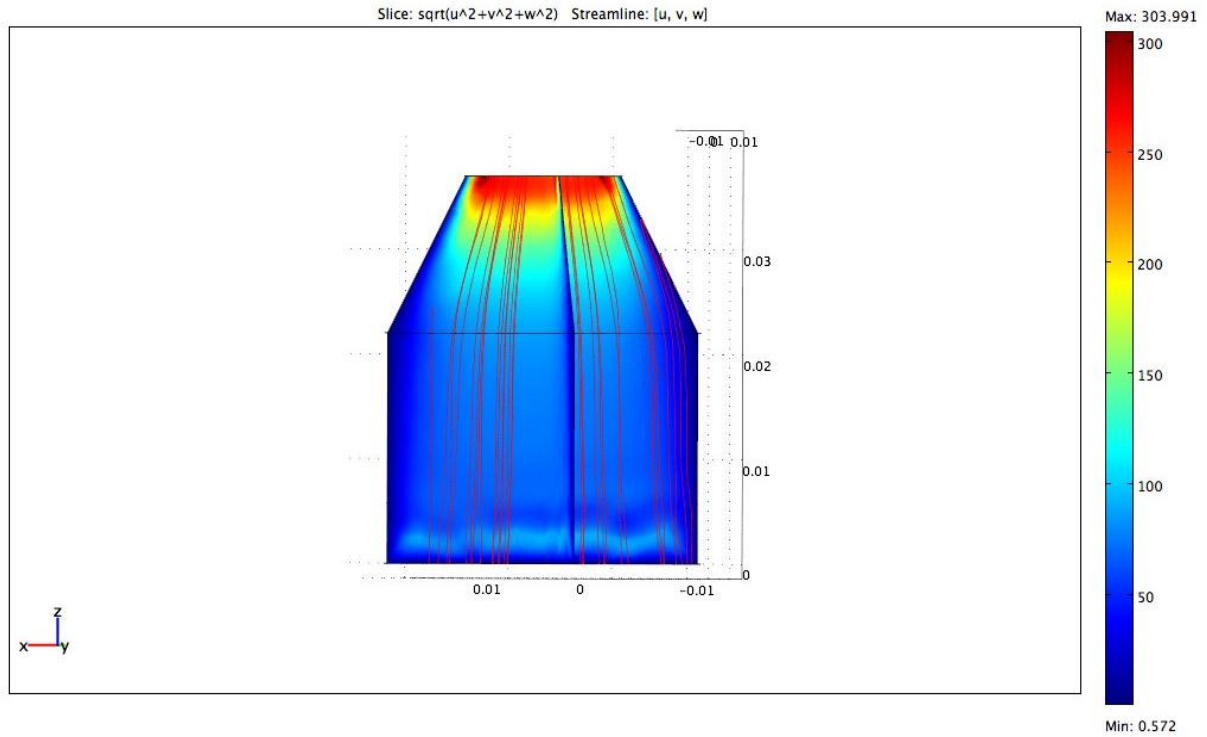


**Figure 4.55** 3-D viscous compressible flow model with RANS smoothing.

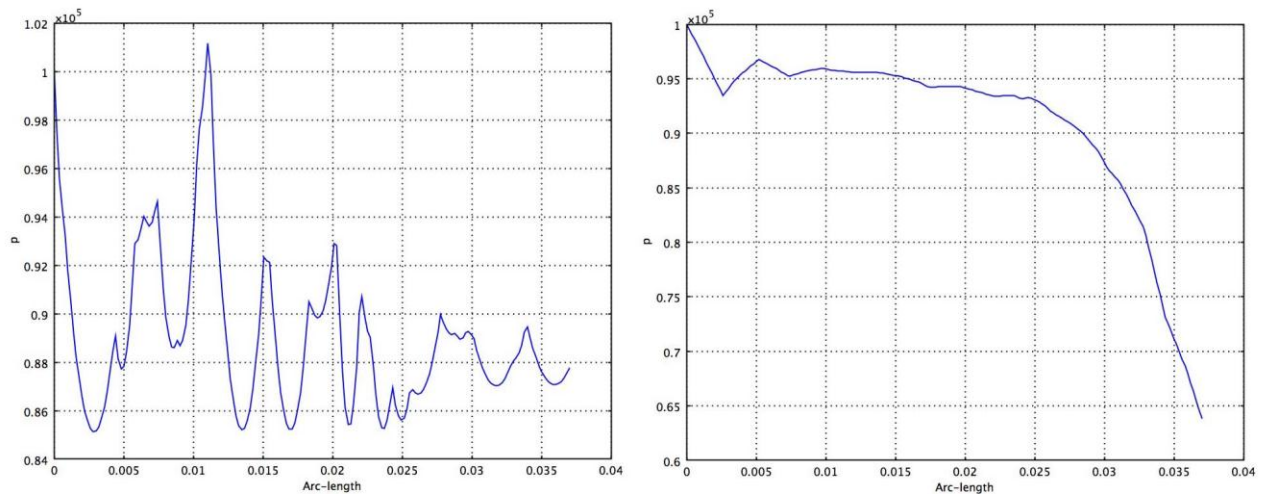


**Figure 4.56** Comparison of pressure vs. distance for 3-D viscous compressible flow solutions before and after RANS smoothing.



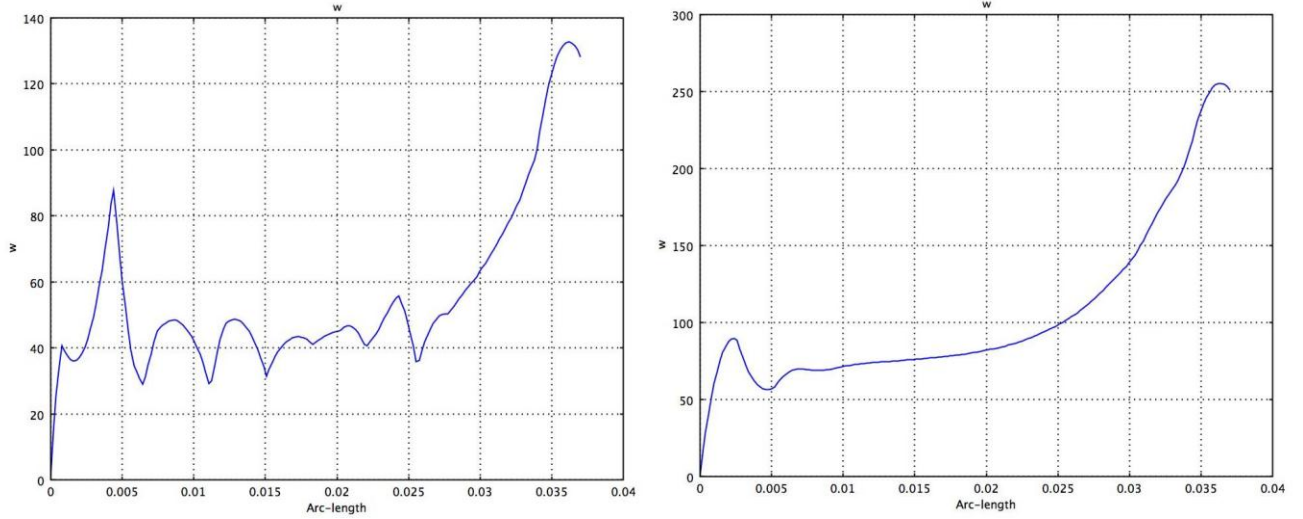


**Figure 4.57** Comparison of velocity vs. distance for 3-D viscous compressible flow solutions before and after RANS smoothing.

### 4.3 Summary of Results

In the initial investigation for an optimized MET design, a configuration using a coaxial port was studied. When modeling the unloaded cavity, the electric field intensity and resonant frequency were found to decrease as the antenna depth increased. The incorporation of a dielectric into the model helped increase the electric field intensity. It was also found that the resonant frequency increased when using a dielectric with a higher dielectric constant, but had little effect on the electric field intensity.

The efforts were shifted toward modeling waveguide cavities with the first model being a single waveguide input directly into the cavity. It was found that the  $TM_{012}^z$  mode was very dominant in the direct waveguide input models and obtaining a solid  $TM_{011}^z$  was unsuccessful. In the study of using various waveguides types, the WR112 half-height configuration provided the strongest electric field. Arcing at the corner where the waveguide met the cavity was found to be a constant issue.

The concept of using two waveguide ports connected directly to the cavity was studied. The mode shape was more symmetric, but again was very strongly resonating at the  $TM_{012}^z$  mode.

A single waveguide with a short was incorporated into the cavity in hopes of stabilizing the  $TM_{011}^z$  mode shape. The mode shape was still unstable and there was an issue with having high



electric fields within the short. An attempt was made to resolve this by replacing the waveguide short with a dielectric made of quartz. This helped to reduce the electric field intensity in the short and increase the electric field intensity at the entrance to the nozzle, but the  $TM_{011}^z$  mode shape was not robust.

The final configuration investigated involved coupling a waveguide with a short to a coaxial antenna. This configuration provided a very robust  $TM_{011}^z$  mode shape. This configuration was then optimized through varying the geometry. Some tests include varying the antenna length, performing a trade study on whether using a WR112 or WR90 half-height vs. full-height configuration was the optimal design. It was ultimately found that the WR112 full-height configuration provided the most stable  $TM_{011}^z$  mode shape with a high electric field strength concentrated at the entrance to the nozzle.

The viscous incompressible flow modeling helped to provide a baseline for the weakly compressible flow modeling. When comparing the results of the incompressible flow and the weakly compressible flow, the variations in the results were minimal. This was very important in that it helped validate the use of the RANS method rather than the GLS method. A 2D viscous compressible flow model was successfully created in COMSOL Multiphysics using the PDE module. However, when this model was expanded to 3D, instabilities in the results arose. Most of these instabilities were successfully resolved via incorporating the RANS smoothing method into the 3D viscous compressible flow model.

## **CHAPTER 5**

### **Conclusions and Future Recommendations**

The overall goal of the computer modeling efforts was to create a complete numerical model of the 8-GHz MET. This coupled multiphysics model would include modeling of the electromagnetics, fluid mechanics, thermodynamics, and plasma physics of the thruster. Though a complete model was not obtained, another step toward this goal was completed. The creation of the compressible flow model in COMSOL Multiphysics marked a great lateral transition from the previous modeling efforts in which the compressible flow was modeled in FLUENT, another commercially available software, which is typically used for fluid modeling.

The electromagnetics modeling in this thesis was very helpful in designing the optimal configuration. Multiple configurations and designs were attempted in finding the ideal configuration that generated the best resonant mode shape with an electric field concentration near the entrance to the nozzle. It was found that, depending on the manner the microwave energy was introduced, the behavior of the mode shapes and resonant frequencies varied greatly. The depth of the antenna in the chamber as well as the shape at the tip also caused great fluctuations in the mode shape and resonant frequency. Using the waveguide-to-coax transition configuration, the desired electromagnetic results were found. The use of computer modeling helped to save time and money by bypassing the need to perform reiterative physical prototyping.

The fluid mechanics modeling in COMSOL Multiphysics marked a great transition from the previous modeling attempts in that using the same software as with the electromagnetics modeling was a step closer to the ultimate goal. The progress with developing a compressible flow model showed that one could successfully move beyond the constraints of solely using the modules at hand and successfully move toward creating the unified model at a pace independent of the development timeframe for new modules in COMSOL Multiphysics. Future work with the compressible flow model should reside primarily in optimizing the RANS smoothing equations used in the simulation to help better smooth and constrain the flow. This would greatly aid in generating a model of the propellant injection system that would give similar characteristic results to that found in the incompressible and weakly compressible flow simulations.

Future work with respect to plasma modeling should begin with attempting to generate a model with COMSOL Multiphysics 4.0's new plasma module. The current constraints of this

module, however, are that it can only simulate plasmas at low pressures ( $< \sim 10$  Torr). The next step, if this low pressure constraint is not removed, would be to develop a model of a plasma within the chamber using the PDE module. Finally, these models, along with a modeling of the thermodynamics, can be condensed into an integrated model that would couple the various physics of the MET to give a total numerical simulation.

Though the progress of the computer modeling presented in this thesis was short of the overall goal, a step was taken in the positive direction, thus laying another brick in the foundation of the ultimate goal of creating an MET model that numerically represents the coalesced plasma characteristics that a physical prototype demonstrates.

## REFERENCES

- 1) Hill, P. and Peterson, C., *Mechanics and Thermodynamics of Propulsion*, 2<sup>nd</sup> Edition, Addison-Wesley Publishing Company, Inc., New York, 1992.
- 2) Wertz, J. and Larson, W., *Space Mission Analysis and Design*, 3<sup>rd</sup> Edition, Microcosm Press and Kluwer Academic Publishers, Boston, 1999.
- 3) Chianese, S. and Micci, M., “Microwave Electrothermal Thruster Chamber Temperature Measurements and Performance Calculations,” AIAA-15337-756, *Journal of Propulsion and Power*, Vol. 22, No. 1, 2006.
- 4) Mueller, J., *Performance Evaluation and Operating Characteristics of a Waveguide Microwave Applicator for Space Propulsion Applications*, Ph.D. Dissertation, Department of Aerospace Engineering, The Pennsylvania State University, 1993.
- 5) Mueller, J. and Micci, M., “Microwave Waveguide Helium Plasmas for Electrothermal Propulsion,” AIAA-23587-274, *Journal of Propulsion and Power*, Vol. 8, No. 5, Sept.–Oct. 1992.
- 6) Balaam, P. and Micci, M., “Investigation of Stabilized Resonant Cavity Microwave Plasmas for Propulsion,” AIAA-23932-388, *Journal of Propulsion and Power*, Vol. 11, No. 5, Sept.–Oct. 1992.
- 7) Sullivan, D. and Micci, M., “Performance Testing and Exhaust Plume Characterization of a Microwave Arcjet Thruster,” AIAA-94-3127, 30th AIAA/ASME/SAE/ASEE JPC, June 27–29, 1994.
- 8) Chianese, S. G., *Microwave Electrothermal Thruster Chamber Temperature Measurements and Energy Exchange Calculations*, Ph.D. Dissertation, Department of Aerospace Engineering, The Pennsylvania State University, 2005.
- 9) Nordling, D., Souliez, F., and Micci, M., “Low-Power Microwave Arcjet Testing,” AIAA-3499-138, 1998.
- 10) Souliez, F., Chianese, S., Dizac, G., and Micci, M., “Low-Power Microwave Arcjet Testing: Plasma and Plume Diagnostics and Performance Evaluation,” AIAA-99-2717, 35th AIAA/ASME/SAE/ASEE JPC, June 20–24, 1999.
- 11) Souliez, F. J., *Low-Power Microwave Arcjet Spectroscopic Diagnostics and Performance Evaluation*, M.S. Thesis, The Pennsylvania State University, 1999.
- 12) Clemens, D., *Performance Evaluation of The Microwave Electrothermal Thruster Using*

*Nitrogen, Simulated Hydrazine, and Ammonia*, Ph.D. Dissertation, Department of Aerospace Engineering, The Pennsylvania State University, 2008.

- 13) Clemens, D., Micci, M., and Bilén, S., “Microwave Electrothermal Thruster Using Simulated Hydrazine,” AIAA-2006-5156, 42th AIAA/ASME/SAE/ASEE JPC, July 9–12, 2006.
- 14) Blum, J., *Performance Evaluation and Optimization of an 8 GHz Microwave Electrothermal Thruster*, M.S. Thesis, The Pennsylvania State University, 2009.
- 15) Venkateswaren, S. and Merkle, C., “Numerical Investigation of Bluff Body Stabilized Microwave Plasmas,” AIAA-91-1503, AIAA 22nd Fluid Dynamics, Plasma Dynamics & Lasers Conference, June 24–26, 1991.
- 16) Bilén, S. G., Valentino, C. J., Micci, M. M., and Clemens, D. E., “Numerical Electromagnetic Modeling of a Low-Power Microwave Electrothermal Thruster,” AIAA-2006-5156, 41th AIAA/ASME/SAE/ASEE JPC & Exhibit, July 10–13, 2005.
- 17) Valentino, C., *A Numerical Study of a Microwave Electrothermal Thruster*, M.S. Thesis, The Pennsylvania State University, 2007.
- 18) Pozar, D., *Microwave Engineering*, 3<sup>rd</sup> Edition, John Wiley & Sons, Inc., Hoboken, 2005.
- 19) Balanis, C., *Advanced Engineering Electromagnetics*, John Wiley & Sons, Inc., Hoboken, 1989.
- 20) Anderson, J., *Modern Compressible Flow*, International Edition, The McGraw–Hill Companies, Inc., New York, 2004.
- 21) White, F., *Viscous Fluid Flow*, 3<sup>rd</sup> Edition, The McGraw–Hill Companies, Inc., 2005.
- 22) Tu, J., *Computational Fluid Dynamics: A Practical Approach*, 1<sup>st</sup> Edition, Elsevier Science & Technology Books, 2007.
- 23) Ashcraft, C., Pierce, D., WAH, K., and Wu, J., *The Reference Manual for SPOOLES, Release 2.2: An Object Oriented Software Library for Solving Sparse Linear Systems of Equations*, URL <http://www.netlib.org/linalg/spooles>, 1999.
- 24) Clemens, D., Micci, M., Bilén, S., Hopkins, J., Blum, J., and DeForce, C., “Evaluation and Optimization of an 8-GHz Microwave Electrothermal Thruster,” AIAA-2010-6520, 46th AIAA/ASME/SAE/ASEE Joint Propulsion Conference and Exhibit, Nashville, TN, July 25-28, 2010.